

ÉCOLE DE TECHNOLOGIE SUPÉRIEURE
UNIVERSITÉ DU QUÉBEC

MASTER'S THESIS PRESENTED TO
ÉCOLE DE TECHNOLOGIE SUPÉRIEURE

IN PARTIAL FULFILLMENT OF THE REQUIREMENTS
FOR A MASTER'S DEGREE IN MECHANICAL ENGINEERING
M.Eng.

BY
Mélissa ANDERSON

TUBE HYDROFORMING OF AEROSPACE ALLOYS:
MATERIAL CHARACTERIZATION METHODS

MONTREAL, AUGUST 19 2010

© Copyright 2010 reserved by Mélissa Anderson

BOARD OF EXAMINERS

THIS THESIS HAS BEEN EVALUATED

BY THE FOLLOWING BOARD OF EXAMINERS

M. Philippe Bocher, Thesis supervisor

Département de génie mécanique à École de technologie supérieure

M. Zhaoheng Liu, President of the Board of Examiners

Département de génie mécanique à École de technologie supérieure

M. Henri Champliaud, Examiner

Département de génie mécanique à École de technologie supérieure

M. Javad Gholipour Baradari, External Examiner

National Research Council, Institute for Aerospace Research, Aerospace Manufacturing Technologies Center

THIS THESIS HAS BEEN PRESENTED AND DEFENDED

BEFORE A BOARD OF EXAMINERS AND PUBLIC

JULY 28 2010

AT ÉCOLE DE TECHNOLOGIE SUPÉRIEURE

"Behind every success is endeavor...

Behind endeavor, ability...

Behind ability, knowledge...

Behind knowledge, a seeker."

Mark Twain

ACKNOWLEDGMENTS

First, I would like to thank my supervisor, Professor Philippe Bocher for his support and invaluable trust throughout this master program. I want to thank him for the opportunity he gave me to present my work at several international and national meetings and conferences. Those two and a half years have been great and full of knowledge.

I would like to extend my special thanks to Dr Javad Gholipour Baradari from NRC-IAR-AMTC for his helpful and insightful advice as well as his constant availability. Our many discussions helped me improve my critical thinking abilities, build my profile as a researcher and a whole lot more.

I gratefully acknowledge Dr Florent Bridier, researcher at ETS, for being there and providing me valuable help and support along with expertise and friendship.

I would like to thank Dr Zhaoheng Liu and Dr Henri Champliaud, professors at ETS, for accepting to be part of my board of examiners.

I also sincerely thank Mr Daniel Chiriac from AMTC for providing technical support. This work was made possible by the financial support provided by Pratt & Whitney Canada, the NRC-IAR-AMTC and the NSERC through the CRIAQ. Special thanks to Dr Jean Savoie from Pratt & Whitney Canada for his enthusiastic support and pertinent suggestions all along the project.

I am particularly grateful to my friends and colleagues who put up with me during the hard times and the joyful ones: Ben, Greg, Christophe, Yoann, Vincent, Yann, Felix, JM, Anko, Helene, Laetitia and all the students who have been in passing at ICIA-016 and AMTC metallic products group.

My special thanks go to my parents and sisters: You supported me throughout my studies and helped me achieve what I have accomplished so far. It would not have been possible without your help. Christelle, Alexandra and Camille, you sometimes believe in me more than I do. I especially thank you for your everlasting love and encouragement.

Last but not least, I would like to send special thanks to Will for always being there for me. I will always be grateful for your patience, love and support.

HYDROFORMAGE DE TUBES EN ALLIAGES AÉRONAUTIQUES: MÉTHODES DE CARACTÉRISATION

Mélissa ANDERSON

SOMMAIRE

L'objectif du projet est de développer des outils de modélisation de procédé pour la fabrication virtuelle de composants aéronautiques par hydroformage de tubes. L'industrie aérospatiale s'intéresse aux possibilités qu'offre la technologie d'hydroformage pour la fabrication de pièces aéronautiques. Dans ce contexte, les travaux menés portent sur la mise en place de méthodes appropriées pour caractériser certains alliages aéronautiques: les aciers inoxydables 321, 17-4 PH ainsi que le superalliage base-nickel Inconel 718. Le présent travail cherche à comprendre le comportement mécanique de ces trois alliages lorsqu'ils sont soumis à des déformations de type hydroformage tels que les essais de traction ou d'expansion libre. Les lois constitutives adéquates pour chaque alliage sont extraites selon différentes géométries d'échantillons et divers états métallurgiques. Cette étude s'inscrit comme base de données expérimentales indispensable pour la construction de modèles valides et robustes pour la simulation numérique du procédé d'hydroformage. De plus, une méthodologie fiable de caractérisation des alliages aéronautiques sous déformation est développée étape par étape. Enfin, cette étude propose les coefficients d'écrouissage appropriés de plusieurs lois constitutives tenant compte de l'état de déformation. Ces données pourront être intégrées directement dans les modèles d'analyse par éléments finis.

Mots-Clés : Hydroformage de tubes, alliages aéronautiques, traction, expansion libre, écrouissage

TUBE HYDROFORMING OF AEROSPACE ALLOYS: MATERIAL CHARACTERIZATION METHODS

Mélissa ANDERSON

ABSTRACT

The objective of the project concerns the setting up of appropriate methods to characterize some aerospace alloys for appropriate process modeling of aerospace components by tube hydroforming. In fact, the aerospace industry is interested in the possibilities of tube hydroforming technology to manufacture generic component prototypes because of its many advantages such as weight and cost reduction. In order to do so, understanding the mechanical behavior during hydroforming-type deformation is considered critical. The materials under investigation are Stainless Steel 321, Stainless Steel 17-4 PH and Superalloy Inconel 718. At the end, the appropriate constitutive laws of these alloys are extracted according to several specimens' geometries and various metallurgical states. This study comes as an essential experimental base needed to build valid and robust material models simulating hydroforming. In addition, it develops a step by step reliable characterization method. The appropriate hardening coefficients of several constitutive laws which could be integrated into the Finite Element Analysis will be discussed.

Keywords: tube hydroforming, aerospace alloys, tensile tests, free expansion tests, hardening laws

HYDROFORMAGE DE TUBES EN ALLIAGES AÉRONAUTIQUES: MÉTHODES DE CARACTÉRISATION

Mélissa ANDERSON

RÉSUMÉ

Ce projet de maîtrise concerne la mise en place de méthodes de caractérisations d'alliages aéronautiques pour des applications en hydroformage. L'hydroformage de tubes est un procédé de mise en forme du métal qui utilise la pression d'un fluide, généralement de l'eau, dans une matrice fermée pour déformer plastiquement des pièces d'épaisseur faible et fabriquer ainsi des composants tubulaires de géométries complexes. Ce procédé possède de nombreux avantages par rapport aux procédés traditionnels d'emboutissage tels que la réduction du poids des pièces car aucun assemblage n'est requis, la diminution des coûts liés au fait qu'aucun consommable n'est utilisé et que toute perte de matière est évitée mais également l'excellent état de surface des pièces hydroformées dû à l'utilisation du fluide. Cependant, malgré tous ces atouts, l'hydroformage reste un procédé marginal surtout dans le domaine aérospatial. À cause du caractère relativement récent de la technique mais aussi le très haut niveau de fiabilité que nécessitent les composants aéronautiques, l'hydroformage de tube en alliages aéronautiques est novateur et nécessite plus de connaissances sur le comportement du matériau pendant le procédé. Très peu d'études ont été menées jusqu'alors, surtout dans le domaine aéronautique, sur le comportement du matériau au cours du procédé. De plus, récemment, la modélisation par éléments finis (MEF) a été largement utilisée pour réduire les coûts de fabrication en simulant le procédé pour éliminer les éventuels problèmes avant de produire la pièce réelle. Pour des simulations fiables, un modèle matériau juste, valide et reflétant le comportement réel du matériau est nécessaire.

Le but du travail présenté dans ce mémoire est de mettre en place des méthodes adaptées, peu coûteuses et qui reflètent le procédé d'hydroformage pour caractériser de façon efficace le comportement de quelques alliages aéronautiques désignés. Ensuite, la construction d'une base de données expérimentale fiable des propriétés mécaniques et coefficients d'écrouissage des alliages étudiés est proposée pour constituer les données d'entrée des futurs modèles de

simulation de l'hydroformage d'alliages aéronautiques. Enfin, un autre aspect est d'introduire des étapes de traitements thermiques au début du processus de déformation pour étudier l'impact de l'état métallurgique du matériau sur sa réponse mécanique et à nouveau proposer les paramètres matériau appropriés dans chaque état.

Le chapitre 1, destiné à une revue de littérature complète, et se subdivise en 3 sous parties. Dans un premier temps, le phénomène de déformation qui prend place lors de tout processus de mise en forme est détaillé. En effet, la déformation peut être définie comme la réponse du matériau à une sollicitation extérieure. Cette réponse se présente sous forme de changement de dimensions ou de forme après application de forces externes. Les essais mécaniques et lois constitutives sont utilisés pour étudier, d'un point de vue macroscopique, le comportement mécanique d'un matériau donné. Cependant, tout changement macroscopique observé est induit par plusieurs petites modifications se produisant à l'échelle microscopique. La capacité des métaux à se déformer plastiquement sans rupture est liée à leur structure composée d'atomes ordonnés mais aussi grâce à la présence de défauts, notamment les dislocations qui se déplacent. Plus elles peuvent le faire facilement, plus la capacité à déformer du matériau diminue. Ainsi, tout élément capable de ralentir, voire de stopper le déplacement des dislocations va contribuer au durcissement du matériau, et donc à son écrouissage. Le phénomène d'écrouissage influence directement les propriétés mécaniques des matériaux. Elles peuvent être quantifiées à partir de tests mécaniques standardisés tel que l'essai de traction. La courbe contrainte-déformation obtenue à l'issu de l'essai de traction renferme plusieurs propriétés indicatrices du comportement mécanique du matériau telles que le module d'Young, la limite élastique ou la contrainte à la rupture. Les lois constitutives sont des formules mathématiques permettant de caractériser le comportement mécanique d'un matériau dans son domaine de déformation plastique uniforme au travers de paramètres tel que le coefficient d'écrouissage.

Plusieurs équations empiriques existent pour décrire la courbe d'écoulement du matériau et seulement cinq des plus connues ont été décrites et traitées dans ce travail :

- *Hollomon equation* : $\sigma = K_H \times \epsilon_p^n$
- *Ludwik equation* : $\sigma = \sigma_0 + K_{L,K} \times \epsilon_p^n$
- *Swift equation* : $\sigma = K_S \times (\epsilon_0 + \epsilon_p)^n$
- *Ludwigson equation* : $\sigma = K_L \times \epsilon_p^n + \exp(K_1 + n_1 \epsilon_p)$
- *Voce equation* : $\sigma = \sigma_V - K_V \times \exp(n_V \epsilon_p)$

Dans la deuxième sous-section du chapitre 1, il est question de la différence en matière de caractérisation entre un tube et une feuille de métal rapportée par plusieurs études précédentes. En effet, à cause des importants niveaux de déformation atteints lors du procédé d'hydroformage, la courbe contrainte-déformation obtenue après l'essai de traction sous-estimerait le niveau réel de déformation possiblement atteint pendant l'hydroformage. D'où la nécessité de mener expérimentalement différents tests de caractérisation allant de l'essai de traction sur feuille plate à l'essai biaxial sur tube. Enfin, la 3^e sous-section présente les alliages aéronautiques étudiés. Ceux-ci ont été choisis car ils sont représentatifs de la production de PWC. Il s'agit de l'acier inoxydable austénitique SS 321, l'acier inoxydable martensitique SS 17-4 PH et le superalliage base Nickel Inconel 718.

La procédure expérimentale est détaillée dans le chapitre 2. Afin de caractériser au mieux le comportement mécanique des matériaux, il est indispensable de mesurer de façon très précise la déformation du matériau au cours des essais. Pour ce faire, deux méthodes de mesure de déformation ont été testées : l'extensomètre-vidéo et le système de mesures de déformation 3D sans contact Aramis. L'extensomètre-vidéo suit la déformation de neuf points tracés au centre de l'échantillon au cours d'un essai de traction. Cette méthode est très utilisée car facile à mettre en œuvre. Cependant, les résultats obtenus ont montré une perte importante de précision due à la position des points au centre de l'éprouvette. Le système Aramis mesure les champs de déformation de points noirs aléatoirement vaporisés sur l'ensemble de l'éprouvette. Cette méthode est définitivement plus exacte et précise que l'extensomètre vidéo car elle donne accès à une variété de méthodes de visualisation des données en plus de suivre précisément les champs de déformations locaux ainsi que d'identifier précisément le début de la striction. Enfin, le système Aramis s'adapte aisément à tout type d'essais. Deux

types d'essais mécaniques ont été menés au cours du projet. L'essai de traction uniaxial qui consiste à appliquer une force sur une éprouvette jusqu'à la rupture double du système Aramis qui enregistre la déformation de l'échantillon durant l'essai. Des essais d'expansion libre ont été conduits pour déterminer les propriétés mécaniques dans un état de déformation biaxial. L'essai d'expansion libre se déroule dans une presse d'hydroformage mais avec une matrice ouverte. Ainsi, le tube peut gonfler librement jusqu'à la rupture. L'historique de déformation du tube est enregistré par le logiciel Aramis. À l'issue des tests, les courbes contrainte-déformation des matériaux sont obtenues et les lois constitutives, nécessaire pour l'implémentation des modèles, doivent être identifiées. Pour ce faire, une méthodologie pour les extraire suivant différents cas de figures a été élaborée. Ainsi, les lois constitutives proposées ont été intégrées dans un programme Matlab qui ajuste les coefficients d'écrouissage des lois par rapport aux données expérimentales par la méthode des moindres carrés.

Le chapitre 3 se concentre sur les résultats obtenus pour l'acier inoxydable 321 et s'intéresse à l'influence de la géométrie de l'échantillon sur les propriétés mécaniques et les lois d'écrouissage. Deux types d'éprouvette de traction ont été étudiés. L'éprouvette plate provenant du métal en feuille et l'éprouvette courbe coupée directement dans le tube. Les essais de traction réalisés sur les échantillons plats ont permis d'évaluer l'influence de la direction de laminage et les résultats ont montré un très faible impact sur les propriétés mécaniques autant que sur les coefficients d'écrouissage. Les essais conduits sur des échantillons courbes de deux épaisseurs ont démontré un effet très net de l'épaisseur. Le tube à épaisseur plus fine voit ses propriétés mécaniques augmenter par écrouissage. Cette étude a été l'occasion de tester un programme permettant d'estimer les courbes contrainte-déformation vraies du matériau à partir des essais d'expansion libre de tubes. La comparaison de ces trois types de géométries a donné des résultats surprenants. Les courbes issues des essais de traction présentent des formes similaires tandis que les courbes calculées à partir des tests d'expansion libre, qui supposément reflètent la biaxialité de ce test ont menées à des déformations de striction et rupture similaires aux précédentes sans atteindre de plus grandes

contraintes. Par contre, les coefficients d'écrouissage obtenus diffèrent ce qui sous tend un comportement d'écrouissage différent selon le type de tests mécaniques.

La deuxième partie des résultats est présentée dans le chapitre 4. L'influence d'un état métallurgique différent sur le comportement mécanique du matériau a été étudié pour les 3 alliages aéronautiques et au moyen d'essais de traction. Pour le 321, un traitement thermique de relaxation des contraintes a été appliqué à quelques éprouvettes avant l'essai et sont comparées à l'état reçu. Les résultats ont montré une amélioration de la ductilité de l'alliage ainsi que l'augmentation du coefficient d'écrouissage n avec le traitement thermique. Pour l'acier 17-4 PH qui se prête bien aux traitements thermiques, deux traitements thermiques ont été testés et comparés à l'état reçu. Le traitement de recuit de survieillissement a adouci le matériau par rapport à l'état reçu avec une augmentation importante de la ductilité couplée à une baisse certaine de la limite élastique tandis que le traitement de durcissement par précipitation a permis d'atteindre des propriétés intermédiaires entre l'état reçu très dur et le survieillissement très doux. De même, les coefficients d'écrouissage sont grandement modifiés avec les traitements thermiques et mènent à des comportements d'écrouissage distincts pour chaque état métallurgique. Enfin, l'inconel 718 a subi un traitement thermique alternatif de mise en solution. Les résultats ont montré un léger durcissement du matériau traité thermiquement sans modification du niveau de ductilité. De même, les coefficients d'écrouissage dans les deux cas, sont restés très proches. Dans le cas du superalliage, le traitement thermique testé ne permet aucun changement significatif du comportement mécanique.

Le but de l'étude menée et présentée dans ce mémoire était de mettre en place une méthode robuste et valide de caractérisation des propriétés mécaniques d'alliages aéronautiques destinés à une mise en forme par hydroformage de tubes. De plus, afin de construire des modèles de simulation valides et qui reflète le procédé étudié, il est primordial d'y implémenter des données exactes. Ainsi, une base de données expérimentales fiable concernant ce type d'alliage a été construite afin d'alimenter les futurs modèles de simulation.

CONTENTS

| | Page |
|--|------|
| INTRODUCTION | 25 |
| Hydroforming generalities | 25 |
| Project objectives: feed simulation models..... | 26 |
| Aeronautical constraints and aerospace alloys limitations | 26 |
| CHAPTER 1 LITTERATURE REVIEW..... | 28 |
| 1.1 The phenomenon of deformation..... | 28 |
| 1.1.1 Levels of deformation..... | 28 |
| 1.1.2 Metallurgical response to deformation | 29 |
| 1.1.2.1 Plastic deformation by slip and dislocation theory | 30 |
| 1.1.2.2 Importance of defects | 31 |
| 1.1.2.3 Strengthening mechanisms..... | 31 |
| 1.1.3 Mechanical point of view..... | 32 |
| 1.1.3.1 Mechanical properties definitions | 32 |
| 1.1.3.2 The necking phenomenon | 36 |
| 1.1.3.3 Material work hardening description | 36 |
| 1.2 Characterization differences between tubes and sheets..... | 39 |
| 1.3 Aerospace alloys | 41 |
| 1.3.1 Stainless Steel 321 | 41 |
| 1.3.1.1 Chemical composition..... | 42 |
| 1.3.1.2 Mechanical properties | 42 |
| 1.3.2 Stainless Steel 17-4 PH | 43 |
| 1.3.2.1 Chemical composition..... | 44 |
| 1.3.2.2 Mechanical properties and microstructure | 45 |
| 1.3.3 Superalloy Inconel 718 | 47 |
| 1.3.3.1 Chemical composition..... | 47 |
| 1.3.3.2 Mechanical properties and microstructure | 48 |
| CHAPTER 2 EXPERIMENTAL PROCESS..... | 51 |
| 2.1 Deformation measurements methods..... | 51 |
| 2.1.1 Video-extensometer method | 52 |
| 2.1.1.1 Procedure | 53 |
| 2.1.1.2 Preliminary results on 17-4 PH | 54 |
| 2.1.1.3 Advantages / Drawbacks of video-extensometry | 56 |
| 2.1.2 Strain field measurement method by image correlation of random pattern.. | 57 |
| 2.1.2.1 Description of the method | 57 |
| 2.1.2.2 Procedure | 59 |
| 2.1.2.3 Preliminary results on 17-4 PH | 61 |
| 2.1.3 Characterization method choice..... | 64 |

| | | |
|--|--|-----|
| 2.2 | Mechanical tests..... | 64 |
| 2.2.1 | Tensile test | 64 |
| 2.2.2 | Free expansion test..... | 66 |
| 2.2.2.1 | Procedure..... | 67 |
| 2.2.2.2 | Stress-strain curves from free expansion tests | 69 |
| 2.3 | Hardening laws extraction | 74 |
| 2.3.1 | Hardening equations presentation..... | 74 |
| 2.3.2 | Fitting method..... | 75 |
| 2.3.3 | Matlab program..... | 76 |
| 2.3.3.1 | Procedure..... | 76 |
| 2.3.3.2 | Main program | 76 |
| 2.3.3.3 | Block diagram | 77 |
| CHAPTER 3 ON THE EFFECT OF SPECIMEN GEOMETRY (SS 321)..... | | 78 |
| 3.1 | From sheets (flattened samples) | 78 |
| 3.1.1 | Stress-Strain curves and mechanical properties..... | 78 |
| 3.1.2 | Hardening equations | 82 |
| 3.1.3 | Effect of the orientation on the hardening equations | 86 |
| 3.2 | From curved specimens | 87 |
| 3.2.1 | Stress-strain curves and mechanical properties | 88 |
| 3.2.2 | Hardening equations | 90 |
| 3.2.3 | Effect of the thickness on the hardening equations | 93 |
| 3.3 | Stress-strain curves from tubes | 97 |
| 3.3.1 | Stress – strain curves..... | 98 |
| 3.3.2 | Hardening equations | 101 |
| 3.3.3 | Effect of the thickness..... | 102 |
| 3.4 | Synthesis | 104 |
| CHAPTER 4 HEAT TREATMENT IMPACT ON THE MATERIAL CONSTITUTIVE LAWS (SS 321 / SS 17-4PH / INC 718)..... | | 107 |
| 4.1 | Stainless Steel 321 | 107 |
| 4.1.1 | Applied Heat treatment | 107 |
| 4.1.2 | Stress-strain curves | 108 |
| 4.1.3 | Hardening equations | 110 |
| 4.2 | Stainless Steel 17-4 PH | 115 |
| 4.2.1 | Heat treatments tested | 115 |
| 4.2.2 | Stress-strain curves comparison..... | 117 |
| 4.2.3 | Hardening equations | 119 |
| 4.2.3.1 | As received state (A-R) | 119 |
| 4.2.3.2 | Annealing Overage heat treatment (AO)..... | 121 |
| 4.2.3.3 | Precipitation hardening heat treatment (PH) | 123 |
| 4.2.4 | Synthesis | 125 |
| 4.3 | Superalloy Inconel 718 | 128 |
| 4.3.1 | Stress Relieve Heat treatment | 128 |
| 4.3.2 | Stress-strain curves | 129 |

| | | |
|--------------------|--|-----|
| 4.3.3 | Hardening equations | 131 |
| 4.3.3.1 | As Received state | 132 |
| 4.3.3.2 | Heat Treatment 2 state..... | 133 |
| 4.3.4 | Synthesis | 135 |
| CONCLUSIONS..... | | 139 |
| ANNEX I | STANDARD TEST METHODS FOR TENSION OF METALLIC MATERIALS..... | 142 |
| ANNEX II | MATLAB PROGRAM FOR HARDENING EQUATIONS EXTRACTION | 143 |
| ANNEX III | 45D AND TD SPECIMENS FROM SHEETS DATA..... | 146 |
| ANNEX IV | 1.2 mm THICKNESS CURVED SPECIMENS DATA..... | 148 |
| ANNEX V | 1.2 mm THICKNESS TUBE SPECIMENS DATA..... | 151 |
| BIBLIOGRAPHY | | 154 |

LIST OF TABLES

| | Page |
|--|------|
| Table 1.1 Chemical composition of SS 321 | 42 |
| Table 1.2 Typical tensile properties of stainless steel 321 | 43 |
| Table 1.3 Chemical composition of SS 17-4 PH | 44 |
| Table 1.4 Typical mechanical properties of 17-4 PH | 46 |
| Table 1.5 Chemical composition of INC 718 | 48 |
| Table 1.6 Typical mechanical properties of INC 718 | 49 |
| Table 2.1 Considered constitutive equations..... | 74 |
| Table 3.1 Mechanical properties of SS 321 flatted samples in 3 directions | 79 |
| Table 3.2 Best fit coefficients of the tested hardening equations – SS321 RD..... | 84 |
| Table 3.3 Best fit coefficients of the tested hardening equations – SS321 45D | 87 |
| Table 3.4 Best fit coefficients of the tested hardening equations – SS321 TD | 87 |
| Table 3.5 Mechanical properties of SS 321 curved specimens– 0.9 mm thick..... | 89 |
| Table 3.6 Best fit coefficients of the tested hardening equations SS321 curved specimens – 0.9 mm thick..... | 92 |
| Table 3.7 Mechanical properties of SS 321 curved samples– 1.2 mm thick | 94 |
| Table 3.8 Best fit coefficients of the tested hardening equations SS321 curved specimens – 1.2 mm thick..... | 94 |
| Table 3.9 Best fit coefficients of the tested hardening equations SS321 tubes 0.9 mm thick..... | 102 |
| Table 3.10 Best fit coefficients of the tested hardening equations – SS321 tubes 1.2 mm thick..... | 103 |
| Table 3.11 Summarization table of hardening coefficients for different equations of SS 321 in various geometries..... | 106 |
| Table 4.1 Mechanical properties of SS 321 flatted samples in A-R and SR states..... | 109 |

| | | |
|------------|--|-----|
| Table 4.2 | Best fit coefficients of the tested hardening equations SS 321 heat treated specimens (SR)..... | 112 |
| Table 4.3 | Mechanical properties of SS 17-4 PH flattened samples in A-R, PH and AO states | 118 |
| Table 4.4 | Best fit coefficients of the tested hardening equations – SS 17-4 PH as received specimens (A-R)..... | 120 |
| Table 4.5 | Calculated YS based on the best fit parameters of tested hardening equations – SS 17-4 PH in A-R state..... | 121 |
| Table 4.6 | Best fit coefficients of the tested hardening equations – SS 17-4 PH overage annealed specimens (AO)..... | 122 |
| Table 4.7 | Calculated YS based on the best fit parameters of tested hardening equations – SS 17-4 PH in AO state..... | 123 |
| Table 4.8 | Best fit coefficients of the tested hardening equations SS 17-4 PH - precipitation hardened specimens (PH) | 124 |
| Table 4.9 | Calculated YS based on the best fit parameters of tested hardening equations – SS 17-4 PH in PH state | 125 |
| Table 4.10 | Mechanical properties of INC 718 flattened samples in A-R and HT2 states | 130 |
| Table 4.11 | Best fit coefficients of the tested hardening equations INC 718 in A-R state | 133 |
| Table 4.12 | Calculated YS based on the best fit parameters of tested hardening equations - INC 718 in A-R state..... | 133 |
| Table 4.13 | Best fit coefficients of the tested hardening equations INC 718 in HT2 state | 134 |
| Table 4.14 | Calculated YS based on the best fit parameters of tested hardening equations INC 718 in HT2 state | 135 |

LIST OF FIGURES

| | Page |
|--|------|
| Figure 0.1 Steps in typical hydroforming process..... | 26 |
| Figure 1.1 Typical engineering stress-strain curve..... | 33 |
| Figure 1.2 Schematic representation of the usual hardening equations..... | 38 |
| Figure 1.3 Stress- strain curves of SS 321..... | 43 |
| Figure 1.4 Stress-strain curves of 17-4 PH bar at various temperatures..... | 46 |
| Figure 1.5 Stress-strain curves of 17-4 PH at different conditions..... | 47 |
| Figure 1.6 Stress-strain curve of Inconel 718 bar at various temperatures..... | 49 |
| Figure 1.7 Tensile properties of aged Inconel 718 bar..... | 50 |
| Figure 2.1 Location of sampling for tension testing of sheet products..... | 52 |
| Figure 2.2 Position and numbering of measurement dots..... | 53 |
| Figure 2.3 Tensile test with video-extensometer assembly..... | 54 |
| Figure 2.4 Tensile engineering stress-strain curves for 17-4 PH RD direction..... | 55 |
| Figure 2.5 17-4 PH RD broken samples..... | 56 |
| Figure 2.6 Aramis system components..... | 58 |
| Figure 2.7 Example of a good pattern..... | 60 |
| Figure 2.8 Images extracted from Aramis at different levels of deformation of a 17-4 PH specimen during tensile test..... | 62 |
| Figure 2.9 Tensile engineering stress-strain curve for 17-4 PH RD direction (Aramis) compared to curves 1 and 6 obtained by Video-Extensometer..... | 63 |
| Figure 2.10 Orientation of tensile samples cut around a tube (curved specimens)..... | 65 |
| Figure 2.11 Schematic view of the free expansion process..... | 67 |
| Figure 2.12 Free expansion test with Aramis set up..... | 68 |
| Figure 2.13 Schematic diagram of the bulge test with the geometrical parameters..... | 70 |

| | |
|--|----|
| Figure 2.14 The state of stress at the tip of bulge region..... | 71 |
| Figure 2.15 Matlab program interface..... | 73 |
| Figure 2.16 Diagram presenting the Matlab main program. | 76 |
| Figure 2.17 Matlab block diagram to find hardening laws best coefficients..... | 77 |
| Figure 3.1 Engineering stress-strain curves of SS 321 flat samples (1 mm thickness) in the three directions. | 79 |
| Figure 3.2 Pole figures of SS 321 on respectively {2 0 0} {2 2 0} {1 1 1} diffracting planes..... | 81 |
| Figure 3.3 True stress-strain curves of SS 321 specimens on the 3 directions in the logarithmic scale. | 82 |
| Figure 3.4 True stress-strain curves of SS 321 RD specimen fitted by calculated hardening equations in the logarithmic scale. | 83 |
| Figure 3.5 True stress-strain curves of SS 321 RD specimen fitted by calculated hardening equations extended to higher strain levels. | 85 |
| Figure 3.6 True stress-strain curves of SS 321 RD specimen fitted by calculated hardening equations extended up to 100%..... | 86 |
| Figure 3.7 Engineering stress-strain curves of SS 321 curved samples cut around the tube – 0.9 mm thick..... | 88 |
| Figure 3.8 Comparison of true stress-strain curves of SS 321 curved samples (0.9mm thick) vs. flat samples (1mm thick). | 90 |
| Figure 3.9 True stress-strain curve of SS 321 curved specimen – 0.9 mm thick fitted by calculated hardening equations in the logarithmic scale. | 91 |
| Figure 3.10 True stress-strain curves of SS 321 curved specimens – 0.9 mm thickness fitted by calculated hardening equations extended up to 100%.... | 92 |
| Figure 3.11 Comparison of engineering stress-strain curves of SS 321 curved samples 0.9 mm vs. 1.2mm thick. | 93 |
| Figure 3.12 Best fit hardening coefficient K of each equation for two different curved specimens (0.9 mm & 1.2 mm thick). | 95 |
| Figure 3.13 Best fit hardening coefficient n of each equation for two different curved specimens (0.9 mm & 1.2 mm thick). | 96 |

| | | |
|-------------|---|-----|
| Figure 3.14 | True stress-strain curves of two thicknesses SS 321 curved specimens (0.9 mm & 1.2 mm) fitted by calculated hardening equations extended up to 100% | 97 |
| Figure 3.15 | Water pressure vs. Expansion curve of SS 321 tubes from free expansion tests – 0.9 mm thick..... | 98 |
| Figure 3.16 | Calculated true stress-strain curves of SS 321 tubes from free expansion tests – 0.9 mm..... | 99 |
| Figure 3.17 | Comparison of true stress-strain curves of SS 321 – sheet (1 mm thick), curved (0.9 mm thick), and the calculated one for tube (0.9 mm thick)..... | 100 |
| Figure 3.18 | True stress-strain curve of SS 321 tubes 0.9 mm thick fitted by calculated hardening equations in the logarithmic scale..... | 101 |
| Figure 3.19 | Calculated true stress-strain curves of two thicknesses SS 321 tubes (0.9 mm & 1.2 mm) fitted by calculated hardening equations extended up to 100% | 103 |
| Figure 3.20 | Stress-strain curves of SS 321 sheets (1mm thick), curved and tubes (0.9 mm) fitted by calculated hardening equations extended up to 100%..... | 105 |
| Figure 3.21 | Stress-strain curves of SS 321 sheets (1 mm), curved and tubes (1.2 mm) fitted by calculated hardening equations extended up to 100%..... | 105 |
| Figure 4.1 | SR performed on the SS 321 specimens..... | 108 |
| Figure 4.2 | Engineering stress-strain curves of SS 321 flat samples (1 mm thickness) in As-Received state vs. Stress Relieve state..... | 109 |
| Figure 4.3 | Comparison of true stress-strain curves of both A-R and SR specimens in logarithmic scale..... | 111 |
| Figure 4.4 | True stress-strain curves of SS 321 SR heat treated specimen fitted by calculated hardening equations in the logarithmic scale..... | 111 |
| Figure 4.5 | Best fit strength coefficient K of each equation for as-received and heat treated specimens..... | 113 |
| Figure 4.6 | Best fit hardening coefficient n of each equation for as-received and heat treated specimens..... | 113 |
| Figure 4.7 | True stress-strain curves of two SS 321 sheets (A-R & SR) fitted by calculated hardening equations extended up to 100%..... | 114 |
| Figure 4.8 | Annealing Overage schedule performed on SS 17-4 PH specimens..... | 116 |
| Figure 4.9 | Precipitation Hardening schedule performed on SS 17-4 PH specimens..... | 116 |

| | | |
|-------------|--|-----|
| Figure 4.10 | Engineering stress-strain curves of SS 17-4 PH flatted samples in A-R, PH and AO states..... | 117 |
| Figure 4.11 | True stress-strain curves of SS 17-4 PH A-R specimen fitted by calculated hardening equations in the logarithmic scale..... | 120 |
| Figure 4.12 | True stress-strain curves of SS 17-4 PH specimen heat treated by AO fitted by calculated hardening equations in the logarithmic scale..... | 122 |
| Figure 4.13 | True stress-strain curves of SS 17-4 PH specimen heat treated by PH fitted by calculated hardening equations in the logarithmic scale..... | 124 |
| Figure 4.14 | Best fit hardening coefficient K of each equation for A-R, AO and PH specimens of SS 17-4 PH..... | 126 |
| Figure 4.15 | Best fit hardening coefficient n of each equation for A-R, AO and PH specimens of SS 17-4 PH..... | 126 |
| Figure 4.16 | True stress-strain curves of SS 17-4 PH specimens (A-R, AO & PH) fitted by calculated hardening equations extended up to 100%..... | 127 |
| Figure 4.17 | Heat treatment conducted on the A-R INC 718 specimens..... | 129 |
| Figure 4.18 | HT2 performed on INC 718 specimens..... | 129 |
| Figure 4.19 | Engineering stress-strain curves of INC 718 flatted samples in A-R and HT2 states..... | 130 |
| Figure 4.20 | Comparison of true stress-strain curves of both A-R and HT2 specimens in logarithmic scale - INC 718..... | 131 |
| Figure 4.21 | True stress-strain curves of INC 718 A-R specimens fitted by calculated hardening equations in the logarithmic scale..... | 132 |
| Figure 4.22 | True stress-strain curves of INC 718 HT2 specimens fitted by calculated hardening equations in the logarithmic scale..... | 134 |
| Figure 4.23 | Best fit hardening coefficient K of each equation for A-R and HT2 specimens of INC 718..... | 136 |
| Figure 4.24 | Best fit hardening coefficient n of each equation for A-R and HT2 specimens of INC 718..... | 136 |
| Figure 4.25 | True stress-strain curves of INC 718 specimens (A-R & HT2) fitted by calculated hardening equations extended up to 100%..... | 137 |

LIST OF ABBREVIATIONS AND ACRONYMS

45D45° Direction

AMTCAerospace Manufacturing Technology Centre

AOAnnealing Overage

A-RAs- Received

ASMAmerican Society of Materials

ASTMAmerican Society of Testing Materials

CRIAQConsortium of Research and Innovation in Aerospace in Quebec

DCCDigital Camera Club

FEMFinite Element Modeling

FCCFace Centered Cubic

FXFree Expansion

HFHydroforming

HT2Heat Treatment 2

INC 718Inconel 718

NSERCNatural Sciences and Engineering Research Council

NRCNational Research Council of Canada

ODForientation Distribution Function

PHPrecipitation Hardening

PWCPratt & Whitney Canada

RDRolling Direction

SRStress Relief

SS 17-4 PHStainless Steel 17-4 PH

SS 321Stainless Steel 321

TDTransverse Direction

THFTube Hydroforming

XRDX-Ray Diffraction

LIST OF SYMBOLS

| | |
|-----------------|-------------------------------------|
| A% | Breaking strain (%) |
| E | Young Modulus (GPa) |
| UTS | Ultimate Tensile Strength (Mpa) |
| N% | Necking strain (%) |
| n | Strain hardening coefficient |
| K | Strength coefficient (Mpa) |
| σ_p | Uniform plastic stress (Mpa) |
| ε_p | Uniform plastic strain |
| HRB | Hardness Rockwell B (HRB) |
| HRC | Hardness Rockwell C (HRC) |
| H900 | Peak-aged heat treatment |
| H1150 | Over-aged heat treatment |
| HT | Heat treatment |
| R-value | Planar anisotropy |
| f | Frequency (Hz) |
| T_f° | Melting temperature ($^{\circ}$ K) |
| YS | Yield strength (MPa) |

INTRODUCTION

Hydroforming generalities

Sheet metal forming is a relevant process for inexpensive manufacturing and allows important cost reduction compare to other methods such as machining. For the manufacture of thin walled parts, several metal forming methods starting from sheet or tubes are available. The most common method is deep drawing (Vollertsen, 2001). Deep drawing is a compression-tension metal forming process in which a sheet metal blank is drawn into a forming die by mechanical action of a punch (Douthett, 2006). This process is well-established but has some limitations such as a non-uniform thickness distribution because of the punch-sheet-die contact or undesirable long process chains with stamping and welding. In order to overcome some of these disadvantages, forming methods with fluids media have been established (Vollertsen, 2001).

Tube hydroforming (THF) is a forming process that uses a pressurized fluid (liquid or gas) to plastically deform a given blank tube material into a desired shape. Figure 0.1 shows a typical tube hydroforming operation for a simple part. The first stage is to place an original tube between the upper and lower dies and close the dies. Then, the ends of the tube are sealed with two plungers and the fluid is pressurized inside the tube to expand it to take the shape of the die cavity. Finally, the dies open and a hydroformed part is obtained. This process presents many advantages: a lower weight/rigidity ratio as well as reducing the number of welds in an assembly which allows a considerable weight reduction. Moreover, hydroforming provides higher strength and quality in a part with complex shape. This process is also known for its reduced tooling and assembly costs. Finally, hydroforming is recognized as an attractive manufacturing process in many fields, notably in the aerospace industry.

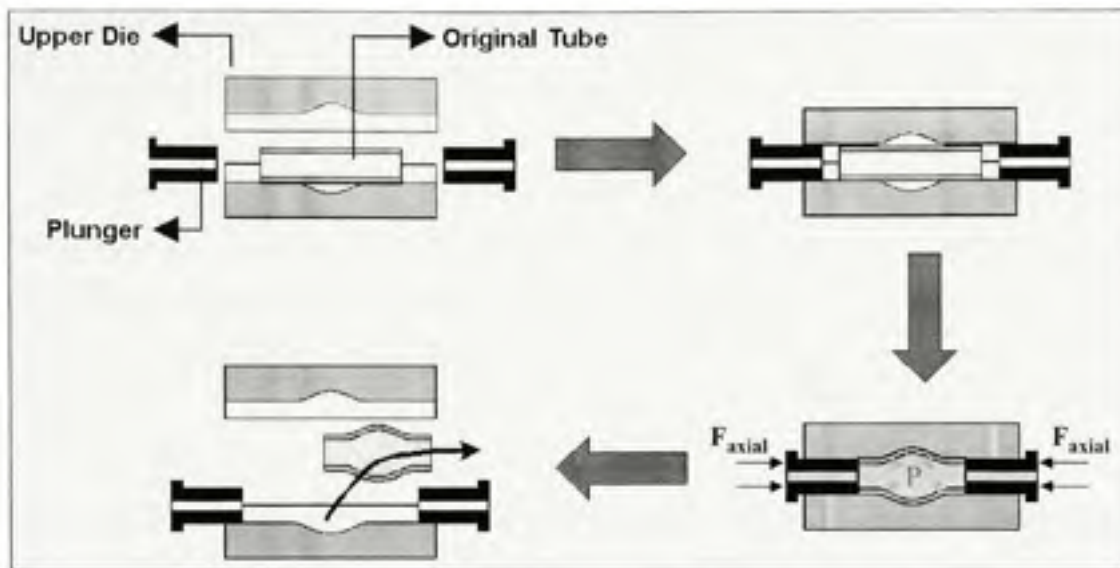


Figure 0.1 Steps in typical hydroforming process.
From Koç (2008, p. 2)

Project objectives: feed simulation models

The global purpose of the CRIAQ 4.6 project is to develop a process modeling tools for virtual manufacturing of aerospace components by tube hydroforming. In other words, the project aims at assessing if tube hydroforming technology can be used to manufacture generic components for the aerospace industries. Even if hydroforming is recognized as an attractive manufacturing process in many fields such as automotive and marine industries, it is not yet the case in the aerospace sector. Because of the recentness of the technology and also the high accuracy/reliability required for aerospace components, hydroforming of aerospace alloys is challenging and requires more knowledge about the material behavior during the process.

Aeronautical constraints and aerospace alloys limitations

Despite of all the advantages in the hydroforming process, it took a long time before the aerospace industry got interested in this process because aerospace components have tight

tolerances and use high-performance materials with high strength that require high pressures. In fact, most aerospace materials are known to be high strength and have limited formability.

Currently, very little work has been done experimentally to characterize the effects of the metallurgical and mechanical behavior of materials under the specific conditions of hydroforming (Ahmetoglu and Altan, 2000; Lianfa and Cheng, 2008), though this step is essential to develop future Finite Element Modeling simulations for Tube Hydroforming optimization.

The focus of the present work is to develop appropriate methods to characterize designated aerospace alloys for this project and understand the material behavior during hydroforming-type deformation. In other words, the purpose was to bring experimental responses to aerospace material deformation by hydroforming. In this study, the first step was to develop an accurate methodology to characterize properly some relevant aerospace materials. The next stage consists of studying the formability of those materials and extracting the suitable constitutive laws for each material to be used in FEM of hydroforming processes. This thesis presents step by step the characterization method used for extracting the constitutive laws for the designated aeronautical alloys to apply inside the FEM models taking into account the deformation state.

The first chapter presents an overview of the literature concerning the hydroforming process challenges. The deformation phenomenon in the case of forming metallurgy is detailed as well as the characterization methods and the studied aeronautical alloys. The experimental procedure is developed in chapter 2. The mechanical point of view, which is the effect of the specimen's geometry on the hardening coefficients, is presented in chapter 3 where as chapter 4 deals with the impact of changing the metallurgical state of the material on the constitutive parameters. The results are discussed directly in each chapter and a conclusion groups together a synthesis and some recommendations for future work on the material characterization of aerospace alloys for hydroforming applications.

CHAPTER I

LITTERATURE REVIEW

This literature review chapter deals with the challenges encountered by the hydroforming process when applied to aerospace alloys. The deformation phenomenon which takes place in any forming process is deeply analyzed on the metallurgical and mechanical points of view. Then, the characterization methods of sheets and tubes are examined and the possible differences between both types are outlined. Finally, the designated aerospace alloys structures and properties are presented.

1.1 The phenomenon of deformation

In order to form a component, a sheet or tube, known as the raw material, can be deformed to obtain the shape of the final part. Dowling (2007, p. 2) gives an interesting definition of the deformation: «A deformation failure is a change in the physical dimensions or shape of the component that is sufficient for its function to be lost or impaired [...]; it is also the cumulative effect of strains in a component, such as bend, twist, or stretch ». The deformation is a change in dimensions or shape as a response of the material under external loads. There are two kind of deformation in metals: the elastic deformation which is recovered after unloading and the plastic deformation which remains permanently. Before going deeper in the characteristics of the deformation related to hydroforming, it is important to talk about the general metallurgical aspects of deformation, i.e. forming processes.

1.1.1 Levels of deformation

In forming metallurgy, there are several scales of observation that define the study method of a deformed material. Many authors distinguish 4 different scales of observation (Montheillet, 2008), (Dowling, 2007):

- A macroscopic scale goes from the fraction of millimeters to meters and considers the whole piece as a homogeneous part. It is the domain of mechanical metallurgy that regroups all mechanical testing and allows the study of the macroscopic behavior of the material, particularly, establish the empirical constitutive laws.
- A mesoscopic scale (from micrometers to one millimeter) corresponds to the metal grains level. It studies of the deformation at a crystal levels and takes into account the material as an aggregated polycrystalline. This scale is generally related to the mechanical analysis of fracture and crystallographic textures measurement.
- A microscopic scale is between nanometers to one micrometer and is the level of crystalline defects. This is the domain of the plasticity based on the dislocation theory. This step allows the understanding of the major part of the plastic deformation mechanisms and the establishment of constitutive laws based on physical considerations.
- A nanoscopic scale, from fraction of nanometer to one nanometer, is called the atoms level. It steps on the study of the material structure and the precipitation mechanisms.

These four scales show how the forming metallurgy enlarges upon a widespread investigation domain. As Dowling said: « Knowledge of behavior over the entire range of sizes from 1 m down to 10^{-10} m contributes to understanding and predicting the performance of machines, vehicles and structures » (2007, p. 25).

In the present work, we are interested on the link between the macroscopic and the microscopic scales. In other words, we aim at explaining how the empirical constitutive laws obtained on the macroscopic scale can be influenced by modifications occurring at the microscopic scale. Next sections highlight the understanding of the mechanical behavior of the materials from the lower end of the scale upward to the upper scale.

1.1.2 Metallurgical response to deformation

To study the mechanical behavior of a material, it is necessary to consider the microscopic mechanisms which sparked off the deformation. These microscopic changes occur at the

molecules or atoms scale. This section will briefly fly over the deformation theory on the side of metals structure and defects. The main goal of this section is to understand the mechanical behavior of materials in terms of metallurgical structure in order to improve their mechanical properties.

1.1.2.1 Plastic deformation by slip and dislocation theory

The ability of metals to deform permanently without rupture is strongly linked to their specific atomic structure, particularly the type of bonding. During a deformation process, an entire section of the metal crystal is able to move without producing fracture in the region of deformation (Allen, 1969). This global movement of atoms should require large amounts of energy, largely more than the observed strength measured during tensile tests. This discrepancy is explained by the existence of certain defects in the lattice. There are several imperfections or defects possible in the crystalline structure, from no dimension (vacancies) to three dimensions (precipitates). The most important one-dimensional defect is the dislocation. The dislocation defect is responsible for the phenomenon of slip, by which most metals deform plastically (Dieter, 1986, p. 110). According to the dislocation theory, the movement of one plane of atoms with respect to another can be accomplished with minimum energy by movement of dislocations along the slip plane (Allen, 1969, p. 494). In other words, the dislocations provide stepwise motion scaled to the spacing of atoms in crystals. This stepwise motion makes it possible to deform materials to large strains by accumulation of these small displacements (Bowman, 2004, p. 117).

The plastic deformation by slip occurs on preferred planes which are most favorably oriented and on which the applied force produces the greatest shearing stress. Thus, dislocations are continually generated during plastic flow, making slip easier on any given plane (Allen, 1969, p. 495). There is another mechanism of deformation different from the slip which is important in some metals: Twinning. Twinning results when the deformation of the metal is such that adjacent planes of atoms are realigned as a reoriented crystal lattice (Allen, 1969, p.

497). The mechanism will not be developed here because it is not the mechanism involved in the studied materials.

1.1.2.2 Importance of defects

As discussed earlier, the plastic deformation of crystals is directly linked to the movement of dislocations. Bowman (2004) notifies that nearly perfect crystals (with very few dislocations) have a very high resistance to plastic deformation, but deform at relatively low stresses after dislocation multiplication taken place. That is to say, the capacity to deform a metal depends on the ease of dislocations movement. So, if the dislocation encounters a region where the atoms are displaced from their usual positions, a higher stress is required to force the dislocation to pass the region. Discontinuities in materials such as vacancies, dislocations, grain boundaries, and precipitates serve as "stop signs" for dislocations (Askeland and Phulé, 2003, p. 159). The strength of a metallic material can, therefore, be controlled by controlling the number and type of imperfections. Thus, strengthening mechanisms represent the key of the understanding for the deformation of polycrystalline materials.

1.1.2.3 Strengthening mechanisms

There are three different strengthening mechanisms based on the three categories of "defects" in crystals. The point defects such as interstitial atoms disrupt the perfection of the crystal structure and slow down the dislocation which has to encounter. By introducing substitutional or interstitial atoms a solid-solution strengthening is caused. As well, surface imperfections such as grain boundaries cause the same effect. At each grain boundary, the movement of dislocations is blocked and higher stresses are needed to keep slipping the dislocation. Increasing the number of grains leads to an increase of grain boundaries so, a grain-size strengthening takes place (Askeland and Phulé, 2003, p. 160). Finally, the third strengthening method, most common in metallic materials comes from dislocation defects. The presence of dislocations alters the perfection of the crystal and their multiplication causes more stop points for the dislocation motion. This strengthening mechanism during

deformation by increasing the number of dislocations is called Strain Hardening (Bowman, 2004, p. 157). Knowing that dislocation motion causes plastic deformation, when there are too many dislocations, they interfere with their own motions in addition to the interaction with the precipitates. The result is an increased strength, hence strain hardening (Dieter, 1986). The strain hardening as well as the amount of precipitates influences directly the mechanical properties of the material.

1.1.3 Mechanical point of view

Previously, material deformation has been presented with a metallurgical point of view. It has been shown that the mechanical properties of metals depend on their metallurgical structure and to well-understand those properties, it is necessary to understand the relationship between mechanical behavior and microstructure. Now, the mechanical properties are approached at the other end of the scale: the macroscopic level. A common way to study the mechanical behavior of material is through standardized mechanical tests to measure the properties.

1.1.3.1 Mechanical properties definitions

The tension test is the most common method used to evaluate the resistance of a material to deformation and failure. It consists on stretching a uniform test specimen along its central axis and records simultaneously the increase of the uniaxial tensile force and the elongation of the specimen. Here, a highlight is made on the response obtained after such a test. More details about the test in practice are available on section 2.2.1. The stress-strain curve is a representation of the performance of the specimen as the applied load is increased monotonically to fracture (Moosbrugger, 2002). Figure 1.1 presents a typical stress-strain curve for a metal obtained from the load-elongation measurements made on the test specimen.

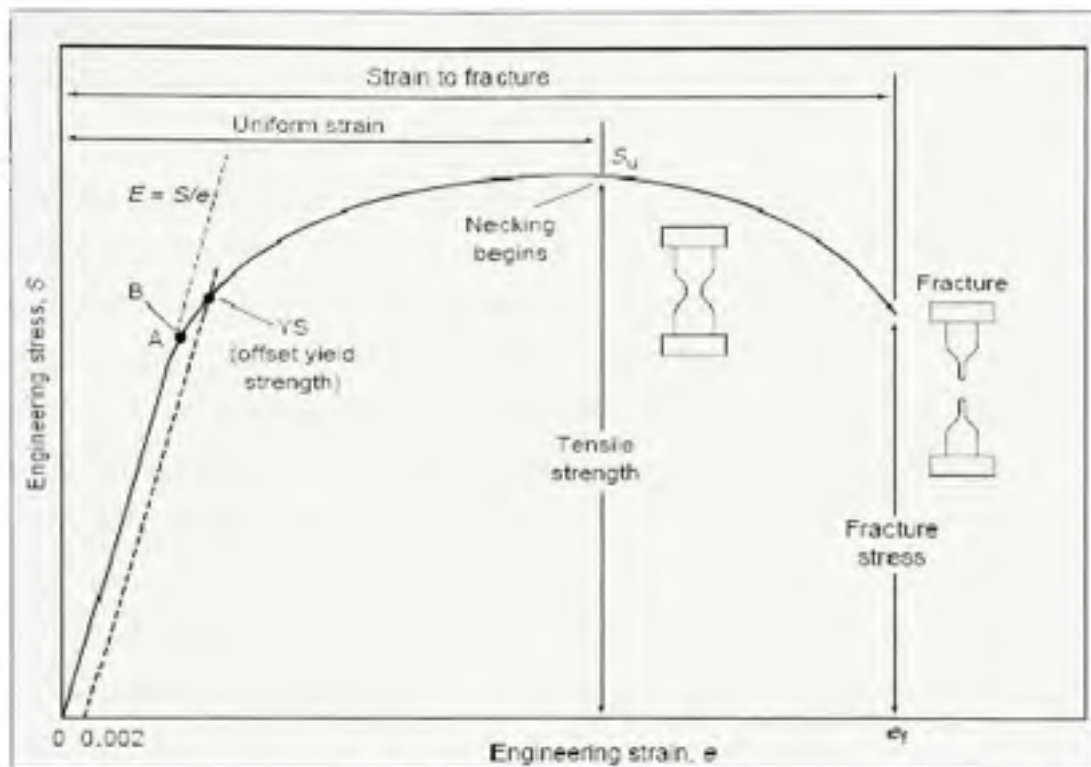


Figure 1.1 Typical engineering stress-strain curve.
From Moosbrugger (2002)

The engineering stress (S) plotted in this diagram corresponds to the average longitudinal stress in the tensile specimen obtained by dividing the applied load by the original area of the cross section of the specimen. The engineering strain (e) is the average strain obtained by dividing the elongation of the gauge length of the specimen by its original length.

The engineering stress-strain diagram can be separated in three parts. The linear segment of curve goes from the origin, 0 to point A and is called the elastic region. In this portion, the stress is linearly proportional to the strain and when the stress is removed, the strain goes back to zero. The most important elastic property is:

- *The modulus of elasticity or Young modulus (E):* it corresponds to the slope of the elastic part of the stress-strain curve. It is a measure of the stiffness of the material. The young modulus is related to the binding forces between atoms. So, it is considered microstructure insensitive since its value is dominated by the strength of atomic bonds, which cannot be modified by microstructure features. On the other hand, it can be

affected by crystal orientations. Heat treatments and cold work can modify E only if they affect the crystallographic orientations texture.

The second part of the stress-strain curve corresponds to the uniform plastic deformation. In this region, from point A (or B) to ultimate tensile strength (S_u), the specimen is permanently deformed even if the load is released to zero. For most materials, the point at which plastic deformation begins is difficult to define with precision (Dieter, 1986, p. 278). Various criteria for the beginning of yielding are used as shown in Figure 1.1:

- *The proportional limit (A)* is the level of stress above which the relation between stress and strain is no more linear
- *The elastic limit (B)* is the maximum stress that can be applied to the specimen without permanent deformation. In other words, it is the critical stress value needed to initiate plastic deformation. In metals, this is usually the stress required for global dislocation motion.
- *The yield strength (YS)* is the stress required to produce a small specified amount of plastic deformation usually defined at an offset strain value of 0.2%. It is the most common parameter used to define the yield point. As depicted in Figure 1.1, a line starting with this offset value of strain and parallel to the elastic part of the curve is drawn. The stress value corresponding to the intersection of this line and the engineering stress-strain curve is defined as the offset yield point. The yield strength obtained by an offset method is widely used for design and specifications purposes, because it avoids subjective estimation of the plastic deformation starting point.

The strain hardening is the increase in the deformation resistance of the material with increasing strain. The volume of the specimen remains constant during plastic deformation and as the specimen elongates, its cross-sectional area decreases uniformly along the gauge length. During the uniform plastic deformation, the strain hardening compensates for this decrease in area and the engineering stress continues to rise with increasing strain. When the stress reaches a maximum, the decrease in specimen cross-sectional area becomes greater than the increase in deformation load arising from strain hardening and the neck occurs.

The latest portion of the stress-strain diagram goes from S_u to fracture. In this section, deformation does not remain uniform. Some properties are linked with this part:

- *The Tensile Strength (S_u) or Ultimate Tensile Strength (UTS)* is the stress obtained for the highest applied force, which automatically correspond to the maximum stress on the engineering stress-strain curve for ductile materials. This value has only a little fundamental significance with regard to the strength of a material as it should only be regarded as the measure of the maximum load that it can withstand under the very restrictive conditions of uniaxial loading (Dieter, 1986, p. 278). The necking effect tends to distort the measurements since it is difficult to compensate for it to calculate the actual local stress strain values.
- *The Necking strain ($N \%$)*: At some point, a region deforms more than the others and a significant local decrease in the cross-sectional area occurs. This phenomenon is known as necking and will be developed in section 1.1.3.2. The deformation reached when necking starts is evaluated as the necking strain, which corresponds to the strain at the tensile strength as the elastic return is negligible in the studied materials.
- *The Elongation (e_f) or Breaking strain ($A \%$)* is one of the conventional measures of ductility. Ductility measures the amount of deformation that a material can withstand without breaking. The elongation describes the permanent plastic deformation before failure and corresponds to the engineering strain at fracture.

Others important concepts on the mechanical behavior of materials have to be defined in order to well-understand the entire material deformation phenomenon:

- *The true stress-true strain curve* uses the instantaneous dimensions of the specimen at each point during the test for the properties evaluation whereas the engineering stress-strain curve used the initial dimensions of the specimen in the calculations. Beyond the point of maximum load, the metal continues to strain hardens up to fracture. So, the true stress increases after necking because, although the load required decreases, the area decreases even more. The true stress- true strain curve is often called “flow curve” when considering only the uniform plastic deformation zone. The equations used to calculate

the true stress strain values are based on the volume constancy assumption and are expressed in the following terms:

$$\sigma_{\text{true}} = \sigma_{\text{eng}} (1 + \varepsilon_{\text{eng}}) \quad (1.1)$$

$$\varepsilon_{\text{true}} = \ln (1 + \varepsilon_{\text{eng}}) \quad (1.2)$$

1.1.3.2 The necking phenomenon

Necking can be defined as a non-uniform or localized plastic deformation resulting in a localized reduction of cross-sectional area of a tensile specimen. This phenomenon is seen only in a tensile test and corresponds, in most cases, to a mechanical instability in tension and not a damage problem. The necking begins at maximum load where the increase in stress due to decrease in the cross-sectional area of the specimen becomes greater than the increase of stress due to strain hardening. The formation of a neck in the tensile specimen introduces a complex triaxial state of stress in that region.

1.1.3.3 Material work hardening description

In order to easily describe the stress-strain curves and strain hardening behavior of metallic materials, flow curves of metals are usually described by mathematical expressions. In the case of cold working, the hardening or constitutive equation is expressed as follows $\sigma_p = f(\varepsilon_p)$. The most common expression describing the strain hardening behavior is a simple power law relation between true stress and true plastic strain:

$$\sigma = K \times \varepsilon_p^n \quad (1.3)$$

Where n is the strain hardening exponent and K the strength coefficient.

Based on the power law equation and after several calculations, Dieter (1986, pp. 289-292) suggests a simple relationship for the strain at which necking occurs:

$$\varepsilon_u = n \quad (1.4)$$

Where ε_u is the true uniform strain and n is the strain hardening exponent.

- *The strain hardening coefficient (n)* is defined as a parameter that described the susceptibility of a material to work harden. It evaluates the effect that strain has on the resulting strength of the material. This dimensionless coefficient is calculated by the ratio $\frac{\partial(\ln\sigma)}{\partial(\ln\varepsilon)}$ (Kleemola and Nieminen, 1974).The parameter n is schematically the slope of the plastic portion of the true stress-true strain curve when plot on a logarithmic scale. The strain hardening exponent values vary between 0 and 1, from perfectly plastic solid to an elastic solid.
- *The strength coefficient K* is an experimental constant computed from the fit of data to assume power curve according to the American Society for Testing and Materials (2000). It is equal to the true stress at $\varepsilon_p=1$.The strength coefficient does not have a physic meaning, it is just a fitting parameter with units of stress.

Deviations from Eq 1.3 are frequently observed, particularly at low and high strains. As a result, several empirical equations have been proposed to describe experimental stress-strain curves. Here, five of the most common relations have been treated and are presented below:

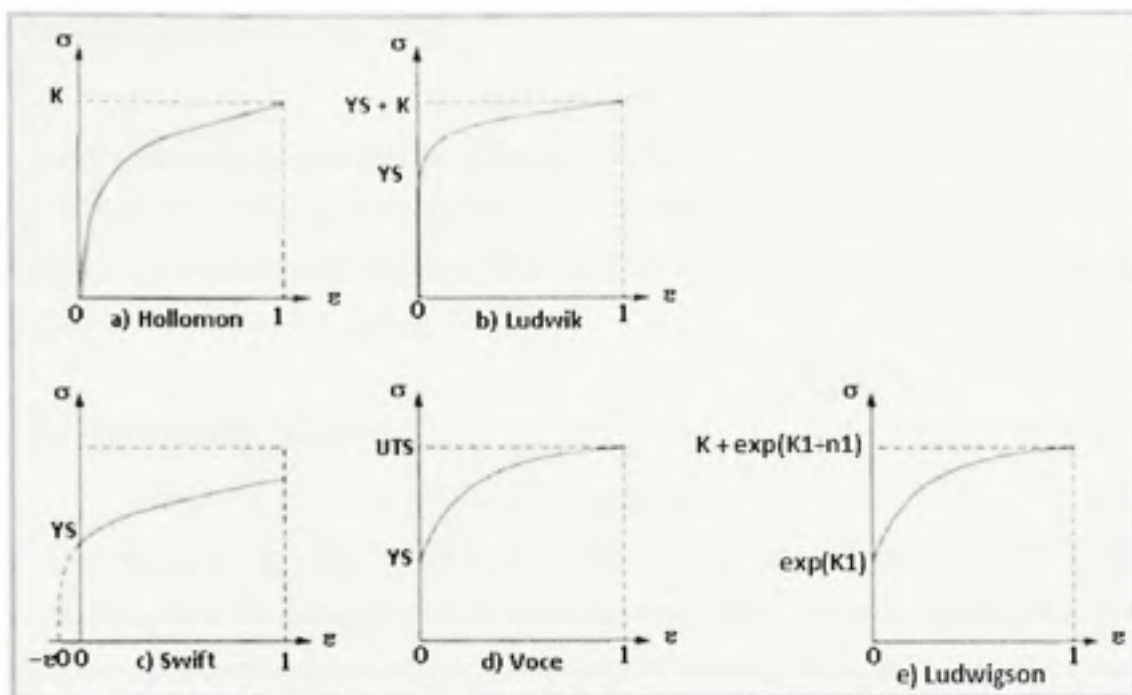


Figure 1.2 Schematic representation of the usual hardening equations.
adapted from Montheillet (2008)

- *The Hollomon equation (Figure 1.2-a):*

$$\sigma = K_H \times \varepsilon_p^n \quad (1.5)$$

The Hollomon equation is equivalent to the power equation given above. The yield strength associated to this relation is null because it corresponds to $\varepsilon_p=0$. This very simple equation is suitable for low to medium carbon steels and low YS alloys (Montheillet, 2008).

- *The Ludwik equation (Figure 1.2-b):*

$$\sigma = \sigma_0 + K_{LK} \times \varepsilon_p^n \quad (1.6)$$

The Ludwik equation allows to introduce a YS criterion (σ_0) and K_{LK} and n , equivalent parameters in analogy to the Hollomon relation. Actually, the Ludwik curve is obtained by translating the Hollomon curve parallel to the stress axis and shift to YS quantity.

- *The Swift equation* (Figure 1.2-c):

$$\sigma = K_S \times (\varepsilon_0 + \varepsilon_p)^n \quad (1.7)$$

The swift equation proposes another strategy to introduce a non null stress for zero plastic strain. The curve is obtained by a translation of the Hollomon law parallel to the strain axis and shift to $-\varepsilon_0$ quantity (Montheillet, 2008). Swift and Ludwik equations are generally used when the user do not want to ignore the YS.

- *The Voce equation* (Figure 1.2-d):

$$\sigma = \sigma_v - K_v \times \exp(n_v \varepsilon_p) \quad (1.8)$$

Here, K_v and n_v are material constants that differ from the usual K and n presented up to now. σ_v represents the constant reached when the strain goes to infinity, in other words the UTS. This equation refers to the dynamic recovery mechanisms at large deformations and is generally used for large strains and for hot working applications.

- *The Ludwigson equation* (Figure 1.2-e):

$$\sigma = K_L \times \varepsilon_p^n + \exp(K_l + n_l \varepsilon_p) \quad (1.9)$$

This equation is suitable for materials which deviate markedly from equation (1.3) at low strains (Dieter, 1986, p. 288) such as austenitic stainless steels. $\exp(K_l)$ is approximately equal to the proportional limit (Figure 1.1 point A) and n_l allows the deviation of stress from equation (1.1) to be quantified.

All the presented mathematical equations aimed to describe the hardening behavior of materials but they are completely empirical and do not contain any mechanisms behind them.

1.2 Characterization differences between tubes and sheets

The objective of the work is to characterize various materials for tube hydroforming applications. Up to now, people used to work with material properties of the flat sheet from which the tube is made. The properties are measured from tensile testing of the sheet metal

prior to rolling (Sokolowski and al., 2000). But the tube making process may have an influence on the mechanical and microstructural properties. In fact, rolling, welding, sizing subsequent operations consume part of the formability of the sheet metal. Thus any material properties such as flow stress, strain hardening, yield strength, etc. may not be the same for sheet and tube even if they come from the same grade and composition sheet (Koç, Aue-ulian and Altan, 2001).

Actually, there are several methods to manufacture tubes and depending on the one chosen, the impact on the formability differs:

1. The most common, cheapest but worst method of producing large quantities of tubes for HF applications is roll-forming followed by a welding process. The weld seam in the tube leads to a non-homogeneity in the material properties and is one of the least deformed regions of a hydroformed part. Some studies have been done on quantifying the available formability used up during tube making and have been summarized by Koç (2008, p. 96). He concludes that the method proposed even if it provides an approximate assessment of the amount of formability used to form a flat sheet into a tube, this effect strongly depends on the tube making method and may vary from one set-up to the other.
2. Tubes, as in our case, can be made by extrusion. This method is interesting because there is no weld line but one of its main drawbacks is the non uniformity of the wall-thickness around the cross section (Koç, 2008, pp. 95-96). In addition, the extrusion process being specific, it generates errors to use the material properties coming from a laminated sheet to attempt characterize an extruded tube.

Another issue with the material characterization method for tubes is the testing methods. The simplest way to obtain formability measurements is to conduct a tensile test. Tensile testing on specimens cut from tubes can be one way to obtain material properties of the tubes. However, the accuracy and appropriateness of these results for hydroforming purposes may be questionable. Koç and al. (2001) gives these three reasons:

- In order to test the specimens cut from tubes, curvature due to tubular form has to be straightened. This would alter the specimen's properties.

- Tensile testing is done under uniaxial loading, and hence uniaxial state of stress exists whereas in HF biaxial even triaxial state of stress also exists.
- The friction condition in HF process may not be repeated in tensile testing method.

The difference of the state of stress in tensile test compared to the one undergoing during hydroforming leads to an under-estimation of the strain localization during HF. In other words, the necking seems to occur prematurely in a tensile test than in a HF. The true stress-strain curve has to be extrapolated in order to try reach the level of deformation expected in HF and a new criterion has to be found.

To be able to carefully characterize the aerospace alloys for HF applications, various characterization methods have been tested, from uniaxial test of flat sheets to biaxial tests on tubes.

1.3 Aerospace alloys

In order to study the properties of sheet metals for aerospace applications, investigations were performed on various materials that are representative of PWC production. Austenitic stainless steels are used for applications requiring high mechanical properties and moderate corrosion resistance, while martensitic stainless steels are used for components designed for higher temperatures applications and superalloys as well.

1.3.1 Stainless Steel 321

Stainless Steel (SS) 321 is not a conventional aeronautical alloy, even if it can be found for particular aerospace applications (Mokrzycki and Savoie, 2006). This alloy is a perfect candidate for this work as it is relatively easy and cheap to get and can be used to put in place the characterization methods. Therefore, a complete study has been conducted on this alloy for both, tubes and sheets.

1.3.1.1 Chemical composition

SS 321 is an austenitic chromium - nickel stainless steel stabilized by titanium against intergranular chromium carbide precipitation. In this type of steel, carbon combines preferentially with titanium to form harmless titanium carbides and leaves chromium in solution to maintain full corrosion resistance (Boyer, 1990, p. 203). Table 1.1 gives the chemical composition of the SS 321.

Table 1.1 Chemical composition of SS 321
From Chandler (1996)

| Element | %weight |
|-------------------|-----------------|
| Carbon | 0.08 |
| Manganese | 2.0 |
| Phosphorus | 0.045 |
| Sulfur | 0.03 |
| Silicon | 1.0 |
| Chromium | 17.00 – 19.00 |
| Nickel | 9.0 – 12.00 |
| Titanium | >5 × %C, < 0.70 |
| Nitrogen | <0.10 |
| Iron | balance |

1.3.1.2 Mechanical properties

SS 321 is extremely tough and ductile, and responds well to deep drawing, bending and forming. It can be hardened only by cold work. Annealing heat treatments are used to relieve stresses, increase softness and ductility, as well as to provide additional stabilization against Chromium carbide formation (Chandler, 1996). Representative tensile properties of SS 321 in the annealed condition as well as stress-strain curves for different deformation

temperatures can be found in the literature (Boyer, 1990). Table 1.2 provides the tension of annealed SS 321 at room temperature. On Figure 1.3, the stress-strain curves under tension at various temperature levels are plotted.

Table 1.2 Typical tensile properties of stainless steel 321
From Boyer (1990)

| SS 321 | Condition | 0.2% Yield strength (MPa) | Tensile strength (MPa) | Elongation (%) | Elastic modulus (GPa) | Hardness (HRB) |
|--------|-----------|---------------------------|------------------------|----------------|-----------------------|----------------|
| | annealed | 240 | 620 | 45 | 193 | 80 |

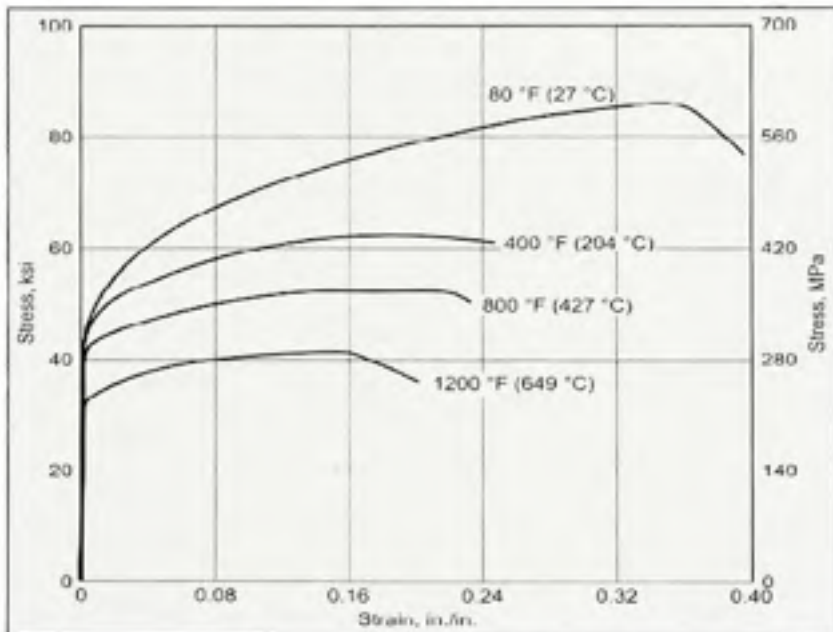


Figure 1.3 Stress- strain curves of SS 321.
From Boyer (1990)

1.3.2 Stainless Steel 17-4 PH

Stainless steel 17-4 PH is a very interesting alloy for aerospace applications because of its high toughness and despite its limited deformation possibilities. Moreover, its sensitivity to heat treatments makes it attractive for hydroforming. For instance, in the case of multi-stage

forming processes, intermediate heat treatments restore the formability used up by previous operations and enable to envisage large cumulative straining and complex deformation paths. Because of material availabilities, the focus of the work will be only on sheet material. The challenge with this alloy is to characterize it in several heat treated conditions and find the best method to extend its formability to make it hydroformable. The heat treatments experimented will be limited to those already in use at PWC.

1.3.2.1 Chemical composition

Table 1.3 gives the chemical composition of SS 17-4 PH.

Table 1.3 Chemical composition of SS 17-4 PH
From ASM International (2002)

| Element | % wt |
|-------------------------------|---------------|
| Carbon | <= 0.07 |
| Manganese | <= 1.00 |
| Phosphorous | <= 0.04 |
| Sulfur | <= 0.03 |
| Silicon | <= 1.00 |
| Chromium | 15.00 – 17.50 |
| Nickel | 3.00 – 5.00 |
| Copper | 3.00 – 5.00 |
| Niobium & Tantalum | 0.15 – 0.45 |
| Iron | balance |

As shown in Table 1.3, the important quantity of chromium gives to this alloy a high corrosion resistance. In addition, the presence of copper will play an important role in the metallurgical behavior of this alloy. Due to its composition, SS 17-4 PH is a precipitation hardening martensitic stainless steel. It has the unique ability to develop high mechanical

strength with relatively simple heat treatments and without any loss of ductility and corrosion resistance. This is made possible by the use of one or both of the hardening mechanisms: martensitic formation and precipitation hardening (Peckner and Bernstein, 1977)

1.3.2.2 Mechanical properties and microstructure

Alloy 17-4 PH has a martensitic structure and possesses the highest possible yield strength among the precipitation hardening stainless steels. This alloy is most often supplied from the mill in solution-annealed state (condition A). Its microstructure is composed of a low-carbon martensite and up to several volume percent of δ -ferrite stringers (Wu, 2003). By subsequent precipitation hardening treatments on the solution annealed condition, a wide range of mechanical properties can be obtained. Several studies on precipitation mechanism of 17-4 PH stainless steel are based on the fact that its precipitation seems to be essentially the same as in Fe-Cu and Fe-Cu-X alloy (Russel and Brown, 1972; Youle and Ralph, 1972). Precipitation starts with the formation of coherent copper rich clusters, which, after further aging, transform into incoherent FCC ϵ -copper precipitates. 17-4 PH can be variously hardened to obtain the desired properties. Most common heat treatments lead to unaged (condition A), peak-aged (H900) and over-aged (H1150) conditions. Table 1.4 gives the mechanical properties of 17-4 PH for these different conditions.

Table 1.4 Typical mechanical properties of 17-4 PH
From Peckner and Bernstein (1977)

| Form | Condition | 0.2% yield strength (MPa) | Tensile strength (MPa) | Breaking Elongation (%) | Elastic modulus (GPa) | Hardness (HRC) |
|----------------------|-------------|---------------------------|------------------------|-------------------------|-----------------------|----------------|
| Sheet cold flattened | Condition A | 1000 | 1103 | 5.0 | - | 35 |
| | H900 / 1* | 1379 | 1448 | 7.0 | 199.9 | 45 |
| | H1150 / 4** | 1034 | 1103 | 11.0 | 200.6 | 35 |

Figure 1.4 provides stress-strain curves of a SS 17-4 PH bar from room temperature (24°C) to elevated temperatures (482 °C). Figure 1.5 also presents the stress-strain curves of 17-4 PH alloy in the various heat treated conditions specified in Table 1.4.

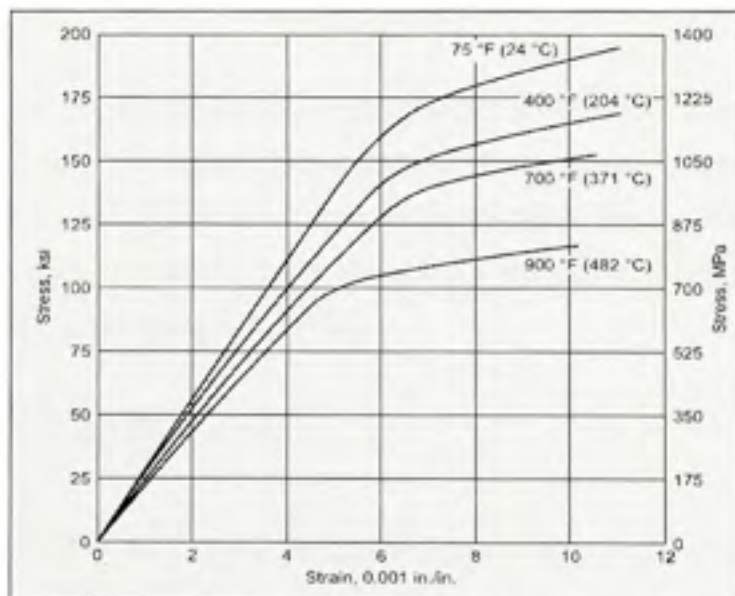


Figure 1.4 Stress-strain curves of 17-4 PH bar at various temperatures.
From Boyer (1990)

* Hardening at 900°F ± 15°F (482°C ± 9°C) during 1 h.

** Hardening at 1150°F ± 15°F (621°C ± 9°C) during 4 h.

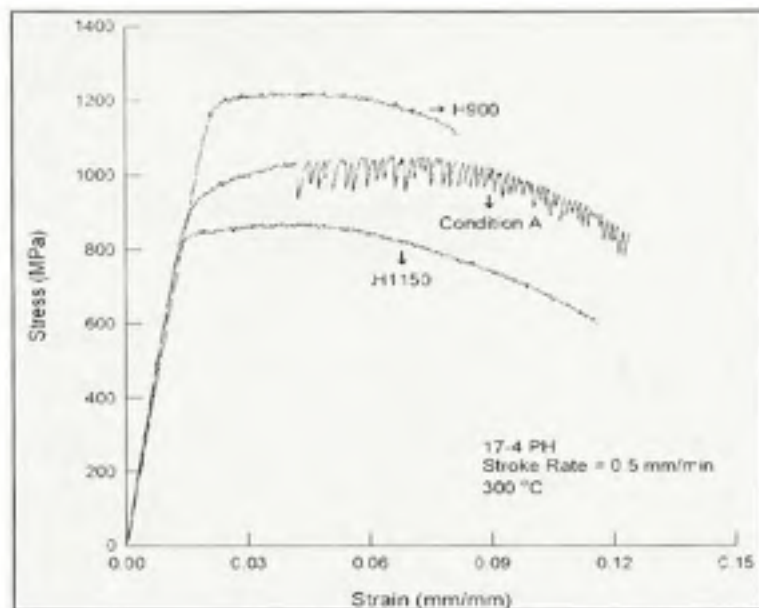


Figure 1.5 Stress-strain curves of 17-4 PH at different conditions.

From Wu (2003)

The main observation extracted from these results is that in this alloy the necking occurs very early (around 4%) and an important deformation after necking is observed. The strain reached before neck seems to be the highest in condition A but significant serrations are observed on the condition A curve. These serrations were interpreted by Wu (2003) during his thesis as dynamic strain aging in 17-4 PH.

1.3.3 Superalloy Inconel 718

Inconel 718 (INC718) is the only superalloy studied in this work. It is one of the most widely-used nickel superalloys and has excellent physical properties which make it interesting for extensive use in aerospace components.

1.3.3.1 Chemical composition

INC718 exhibits excellent physical and mechanical properties, which remain from cryogenic to elevated temperatures ($0.8 \times T_g$). It maintains high strength and excellent corrosion

resistance at high temperatures (Song and Huh, 2007). The chemical composition of INC718 is presented in Table 1.5.

Table 1.5 Chemical composition of INC 718
From Boyer (1990)

| Element | %wt |
|-------------------------------|---------------|
| Carbon | <= 0.10 |
| Silicon | <= 0.75 |
| Manganese | <= 0.50 |
| Copper | <= 0.75 |
| Nickel | 50.00 – 55.00 |
| Chromium | 17.00 – 21.00 |
| Niobium & Tantalum | 4.50 – 5.75 |
| Molybdenum | 2.80 – 3.30 |
| Aluminum | 0.20 – 1.00 |
| Titanium | 0.30 – 1.30 |

1.3.3.2 Mechanical properties and microstructure

INC 718 superalloy consists of an FCC γ -matrix with intergranular β -precipitates, (Nb, Ti) C carbides and a high volume fraction of embedded γ' and γ'' precipitates (Song and Huh, 2007). These precipitates impart reasonably high tensile and creep strength at elevated temperatures while maintaining adequate ductility, fracture toughness and fatigue properties. According to the literature (Slama and Cizeron, 1997), the various hardening carbides are formed jointly or successively depending on the temperature range and the aging time.

The tensile properties of INC718 alloy at room temperature change according to different heat treatment conditions, as presented in Table 1.6.

Table 1.6 Typical mechanical properties of INC 718
From Boyer (1990)

| Conditions | 0.2% yield strength (MPa) | Tensile strength (MPa) | Breaking Elongation (%) | Elastic modulus (GPa) |
|-------------------------|---------------------------|------------------------|-------------------------|-----------------------|
| Cast & Age-Hardened* | 828 | 1000 | 10 | - |
| Annealed** | 414 | 897 | 45 | 204 |
| Annealed & Age-Hardened | 1034 | 1310 | 25 | - |

The stress-strain curve of INC718 annealed and aged bar at room and elevated temperatures is presented in Figure 1.6 and his tensile properties as a function of temperature in Figure 1.7.

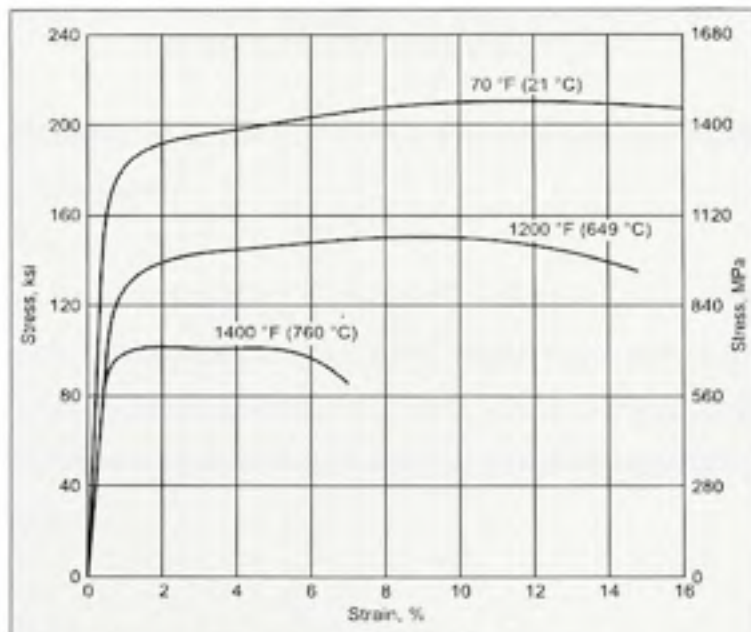


Figure 1.6 Stress-strain curve of Inconel 718 bar at various temperatures.
From Boyer (1990)

* Age-Hardening at 1325°F (718°C) during 16h

** Annealing at 1750°F (955°C) during 1h

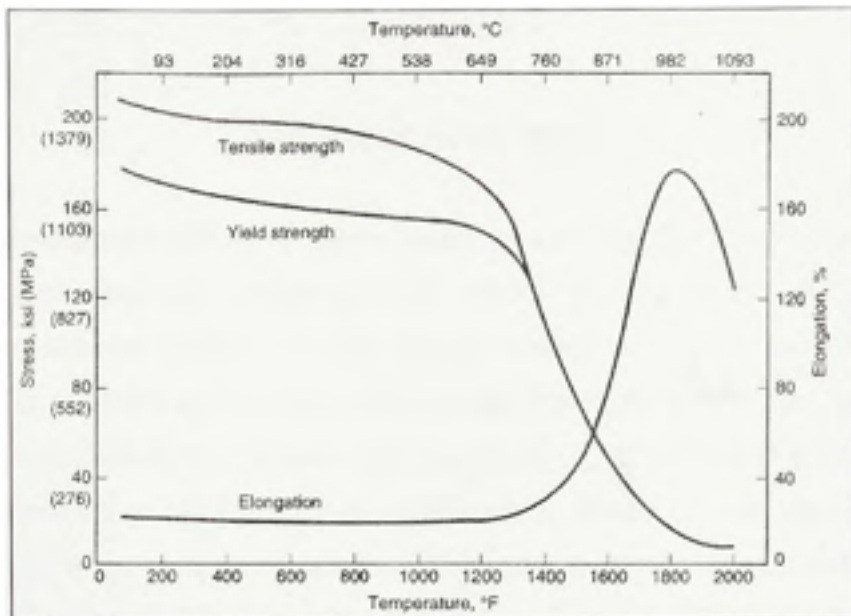


Figure 1.7 Tensile properties of aged Inconel 718 bar.
From Special Metals Corporation (2007)

As can be seen from these figures, INC718 has a wide plastic range which is interesting for deformation by hydroforming.

INC718 is the most concerned material in the global project. Its complex microstructure with several precipitates is interesting to study, notably thanks to the effects of heat treatment on its microstructures and hardening potential. However, it is very expensive and difficult to get. So, very little work has been conducted on this material available only in sheet form.

CHAPTER 2

EXPERIMENTAL PROCESS

The experimental tests will allow documenting the mechanical behavior of each material. It is therefore very important to track precisely sample deformations during the tests. For that reason, two different methods for deformation measurement have been tested. A video-extensometer, available at ETS, was used to measure deformation by tracking the movement of some dots marked on the specimen and an Aramis system, an optical grainy pattern image correlation through a 3D deformation measurement, which was set up at AMTC. Also, different mechanical testing methods used in the present work are presented in this section, namely: uniaxial tensile testing and free expansion testing also called hydro bulge testing.

2.1 Deformation measurements methods

Tensile tests have been chosen to compare both deformation tracking methods as it is one of the most commonly used tests for evaluating mechanical behavior of materials under uniaxial loading. It consists of slowly pulling a sample of material in tension until it breaks. During the test, force-displacement data are monitored and recorded to provide a quantitative measure of how the test item deforms under an applied tensile force. Both video-extensometer and Aramis system give information on the specimen's extension by using a slight different way.

The video-extensometer measures the displacement between dots whereas Aramis records the deformation of the points painted on the sample. The video-extensometer cannot report accurately the occurrence level, intensity and origin of strain localization. The deformation depends on the position of the failure. This inaccuracy may generate errors and infers imprecision around the video-extensometer method. The Aramis method covers a larger zone of deformation which will include inevitably the failure. However, the frequency of the images record in the case of Aramis is limited by the capacity of the computer used and becomes far less than in the video-extensometer. This may be a drawback of the Aramis

method. The classical extensometers have not been tested because of their main drawback which is the possible damage of the sample due to the contact. To set up the best characterization method in our case, it is important to compare both deformation measurement methods in order to choose the appropriate one. The latter will be used to extract the strains which will allow the evaluation of the hardening coefficients in further constitutive equations.

To illustrate the different deformation measurement methods, data plotted in this section comes from results obtained on 17-4 PH specimens extracted from sheets in the as received state (Condition A) as specified in ASTM Spec A8 (ANNEX I). The tested samples were taken along the rolling direction (RD) of the sheet. Figure 2.1 shows the relative direction of the samples to the processing geometry.

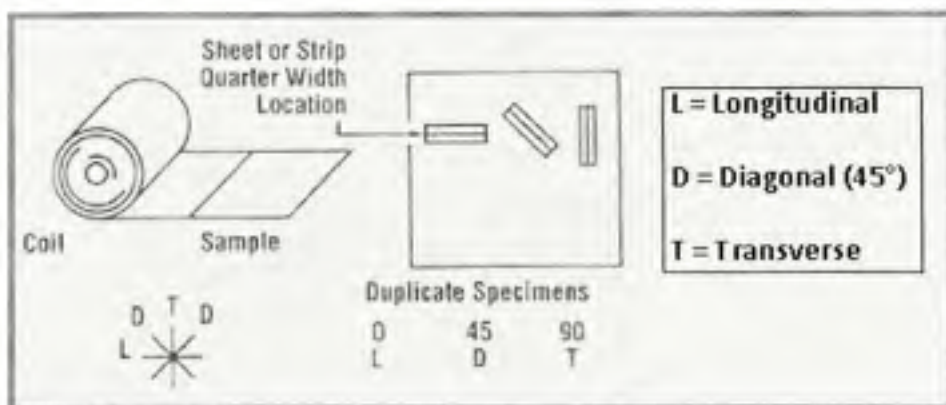


Figure 2.1 Location of sampling for tension testing of sheet products².

2.1.1 Video-extensometer method

A video extensometer is used for non contact and accurate deformation measurements without the drawbacks of contact extensometers. Furthermore, it allows to document usual tensile properties (yield strength, ultimate tensile strength and elongation).

² Selected stamping and formability measurements: <http://www.a-sp.org/database/viewsec.asp?sec=594>

2.1.1.1 Procedure

The video-extensometer used is a Messphysik ME-46. The system comprises a video camera DCC, several lenses, a computer with the application software. Prior to test, the widths and thicknesses of the specimens are measured at three different locations along the gauge length (at both ends and at the middle of the gauge length) using a caliper. Then, nine dots are drawn manually with a permanent marker at the middle of the gauge length with a specific pattern as presented in Figure 2.2. During the tensile test, the position in 2D of each dot is recorded with a high speed camera (registered marks). With the aid of measurement software (Dot Measurement), the points are numbered, digitized and so that the distance between points 1 and 3 is always equal to one. In order to get valid results, contrast between the dots and the background is maximized. For that reason, light intensity has to be adjusted using a lens diaphragm.

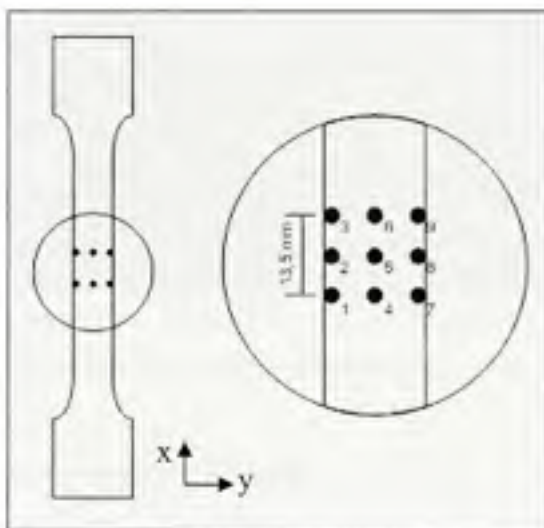


Figure 2.2 Position and numbering of measurement dots.

The tests were conducted on a MTS machine (series 810) with hydraulic fixtures, available at ETS. Amplification modules were used for a maximum load of 100kN and a maximum displacement of 100 mm (Figure 2.3). The position of dots and the force / displacement parameters of the tensile machine are recorded at 33 Hz whereas the position of points along both axis are recorded in the direction of the applied load (X axis) and in the transverse direction (Y

axis) in a text file at the rate of 4 Hz. The loading rate is 0.06 mm per second. These numbers have been chosen to remain consistent compare to previous work done by PWC (Mokrzycki and Savoie, 2006). The difference between the recording frequencies may affect the precision of the test but the relatively slow testing rate compensates for the loss of data. The load is recorded and will be used to calculate the stress. The position of dots will be used for strain calculations. These data will allow the evaluation of stress-strain curves.

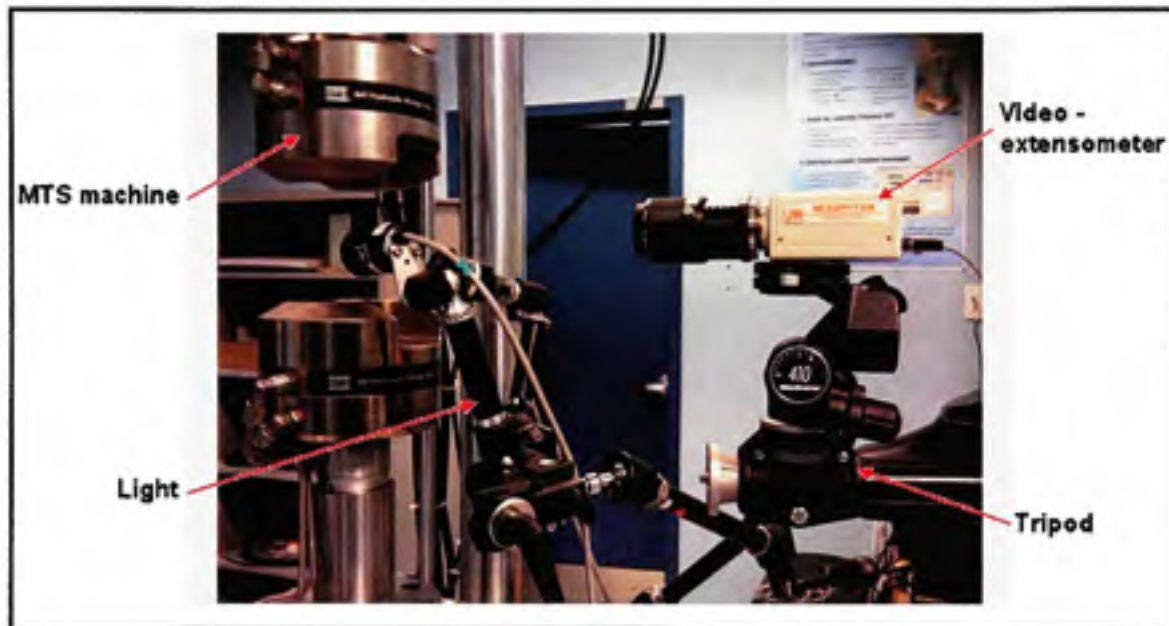


Figure 2.3 Tensile test with video-extensometer assembly.

2.1.1.2 Preliminary results on 17-4 PH

The tests have been conducted on six 17-4 PH samples in rolling direction (RD) randomly chosen. The stress-strain curves obtained are presented in Figure 2.4.

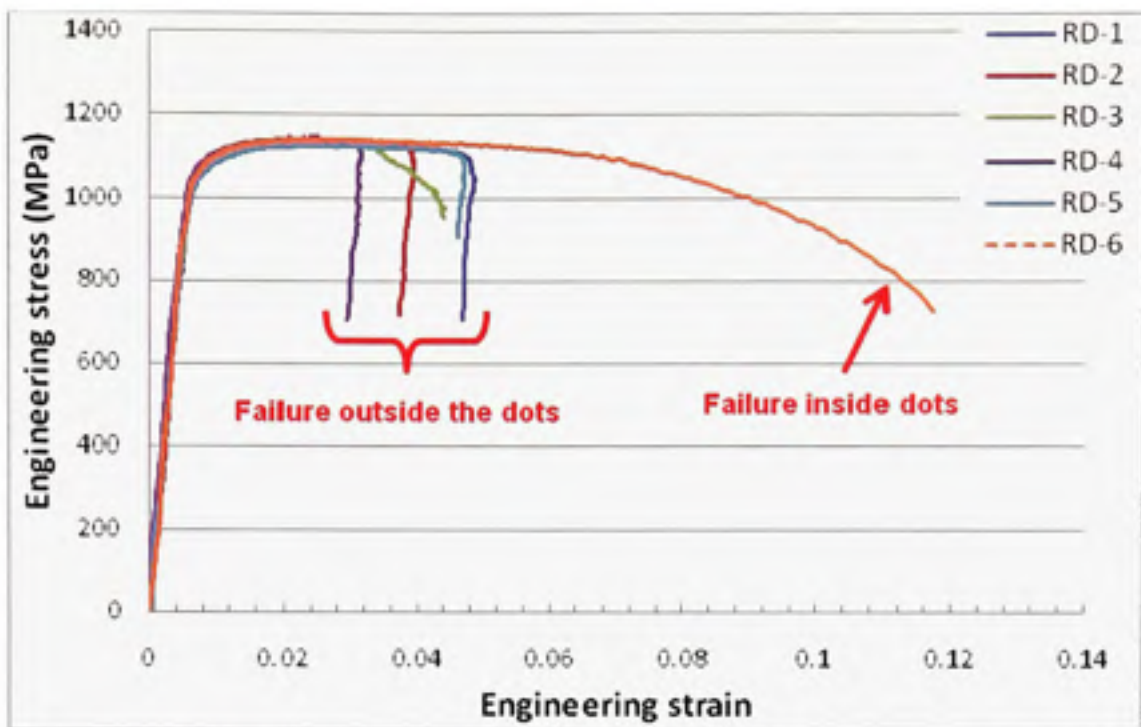


Figure 2.4 Tensile engineering stress-strain curves for 17-4 PH RD direction.

The behavior of the tested samples is reproducible from the elastic part up to the YS. But, a big difference between the first five samples (RD-1 to RD-5) and the sixth one is observed. The stress-strain curves are quite different after the neck point and the rupture strain goes from 5% to almost 12 % for the same material, the same direction. The only difference between those samples is the position of the necking relative to dots location as shown in Figure 2.5.

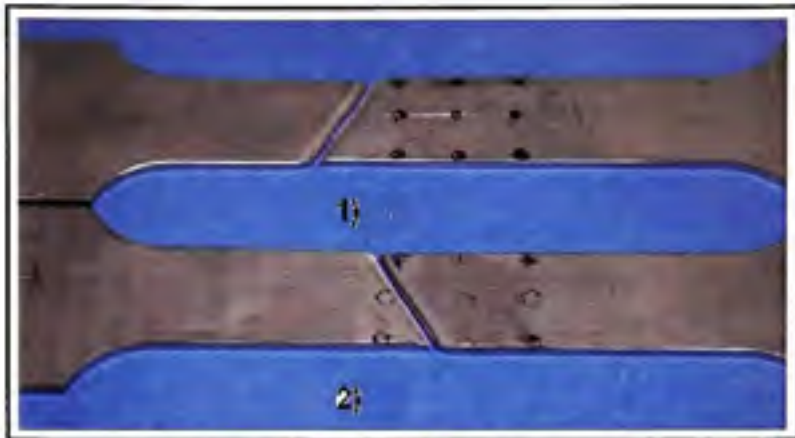


Figure 2.5 17-4 PH RD broken samples:

- 1) Failure outside the dots (RD-1)
- 2) Failure inside the dots (RD-6).

If the necking appears between the 9 dots, the distance between the upper dots and the lower ones increases dramatically and the recording strains take into account the necking strain in addition to the conventional plastic deformation. This issue causes a significant and non negligible error in the evaluation of the necking strain. For instance, the necking strain obtained in the case of sample RD-6 is about 6.5% when in sample RD-1 we hardly reach to 3%. In fact, if rupture takes place outside the dots, the recorded deformation could be lower than the actual deformation since it can be far from the recorded part of the sample. This can suggest that a failure either inside or outside the dots does not reflect the real plastic deformation.

2.1.1.3 Advantages / Drawbacks of video-extensometry

The video-extensometer is a widely used method to measure deformation. Its principal advantage is the easy set up. It takes generally less than an hour to prepare a test. It is also a very accurate method for calculating some mechanical properties such as the elastic modulus and the yield strength. However, this method presents one important drawback concerning the evaluation of the necking strain. The stress-strain curve shape obtained at the end of the test widely depends on the position of the failure (inside or outside the dots). This aspect will

bring important errors on the evaluation of the hardening laws since a maximum precision is required on the deformation measurement.

To counter pass these issues, the Aramis® system, which can be considered as an improved video-extensometer with two cameras instead of only one, has been tested on the 17-4 PH specimens.

2.1.2 Strain field measurement method by image correlation of random pattern

The Aramis system is a non-contact optical 3D deformation measuring system. It documents, analyzes, and calculates the distribution of material deformation. The graphical presentation of the measured variables provides a convenient understanding of the sample's behavior. It can be used for tensile testing or more complex forming processes, such as free expansion. The Aramis system has quite a wide range of applications. It can record data with local resolution, high 3D strain field accuracy under static and dynamic loading.

2.1.2.1 Description of the method

The Aramis system consists of a sensor with two CCD cameras (for 3D set up), a trigger box to synchronize images with other process parameters at a high frame rates and a high performance PC system with Aramis application software. Figure 2.6 shows the different parts of the Aramis system.

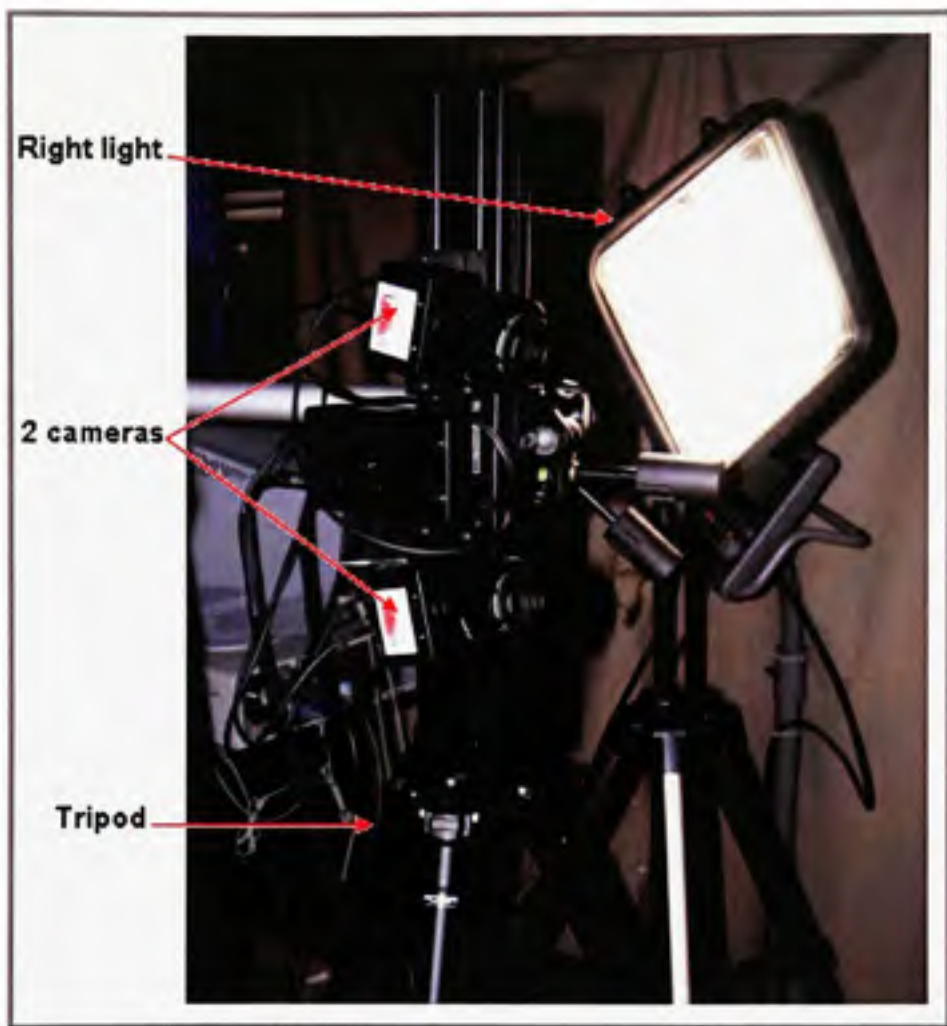


Figure 2.6 Aramis system components.

The Aramis software permits the specimen's surface geometry to be recognized by digital images and allocates coordinates to the image pixels. The first coordinates are gathered when recording the reference condition. This image is the undeformed state of the specimen. During sample deformation, further images are recorded. Aramis observes the deformation of the specimen through the images by means of a large number of square image details called facets. A facet is a small square of 15×15 pixels which is approximately the size of one black dot. Each image is divided into many facets. The facets are identified by the individual gray level structures of the individual pixels within the facet. The system determines the 2D coordinates of the facets from the corner points and the resulting centers. Using

photogrammetric methods, the 2D coordinates of a facet, observed by the left and right cameras, lead to the calculation of the 3rd dimensional coordinate. A color spray pattern on the specimen surface is necessary, especially for homogeneous surfaces' specimens. If the speckle pattern is sufficiently stochastic, each facet presents a unique pattern of a few dots within the image so that the software can calculate the position as well as the deformation of the facets along the test through the recorded images. The specimen deformation is calculated by comparing the dots position and shape on the deformation stages to their position on the first image corresponding to no deformation. Aramis system is used to measure with high temporal and local resolution as well as high accuracy, 3D deformation and strain in material specimens.

2.1.2.2 Procedure

The Aramis set up procedure is divided in four steps: painting, calibration, the test itself and the computation.

Painting

The Aramis ability to capture strains during the deformation is closely bounded to the quality of the paint applied to the samples. The biggest issue is to obtain maximum contrast between the white paint and the black dots randomly sprayed on all samples. The white paint should be flat to avoid reflection and thin enough to avoid unsticking. A distance of approximately 15 cm should be considered between the sprayer and the sample in order to get the desired layer of paint. To apply the black dots, an airbrush is used instead of a black spray. To obtain a good contrast, the operative pressure of the airbrush should be around 200 Kpa (30 Psi) with a distance of about 2 meters from the sample. Otherwise the dots might be too big. Figure 2.7 shows an example of a good painting pattern.



Figure 2.7 Example of a good pattern.

Calibration

The second concern is the calibration of the Aramis system. This step allows calibrating the software with the proper distances between the cameras and the sample as well as adjusting the cameras' angle. In other words, the calibration step allows the system to be at a known distance from the sample and it should observe clearly the whole specimen during the full test. The lighting is also an important parameter to take into account for proper results. In fact, the entire specimen has to be uniformly enlightened with no part in the darkness to avoid some missing data. This part is very critical and should be conducted very carefully to get the best out of the system. Also, whenever the calibration is done, nor the tripod nor the cameras should be moved during the test, otherwise the calibration has to be redone.

Test procedure

After the calibration, the test can be carried out. The Aramis procedure for both tensile and free expansion tests is quite similar and only the procedure of the tensile test is detailed here. The sample is fixed onto the tensile machine. The test is started manually at the same time on both: the tensile machine and the Aramis system. Aramis captured images at the frame rate of 3 Hz. At the end of the test, all the stages (corresponding to each image) is computed and post processed in order to extract the desired data; for example the strains values. The images could be assembled to record a movie or just to see the strain localization (necking). The load levels are obtained by extracting data from the tensile machine and in order to calculate the local stress field.

3D Computation

At the end of the test, a computation is needed to extract the deformation. For facet computation, the definition of the starting point is required. The starting point is manually chosen on the first image (no deformation) by the operator. In both camera images these points are marked. The computation part consists on putting together the images captured by each camera to reach a 3D level and calculate the strains based on the displacements and shapes of the facets inside the images.

2.1.2.3 Preliminary results on 17-4 PH

Two RD specimens of 17-4 PH have been tested using Aramis system for method comparison. These specimens were extracted from the same batch as the samples tested with the video-extensometer. The stress-strain curves obtained using Aramis system are reproducible and close to each other. Interestingly, the strain distribution along the specimen can be tracked in live through the images extracted from Aramis as shown in Figure 2.8.

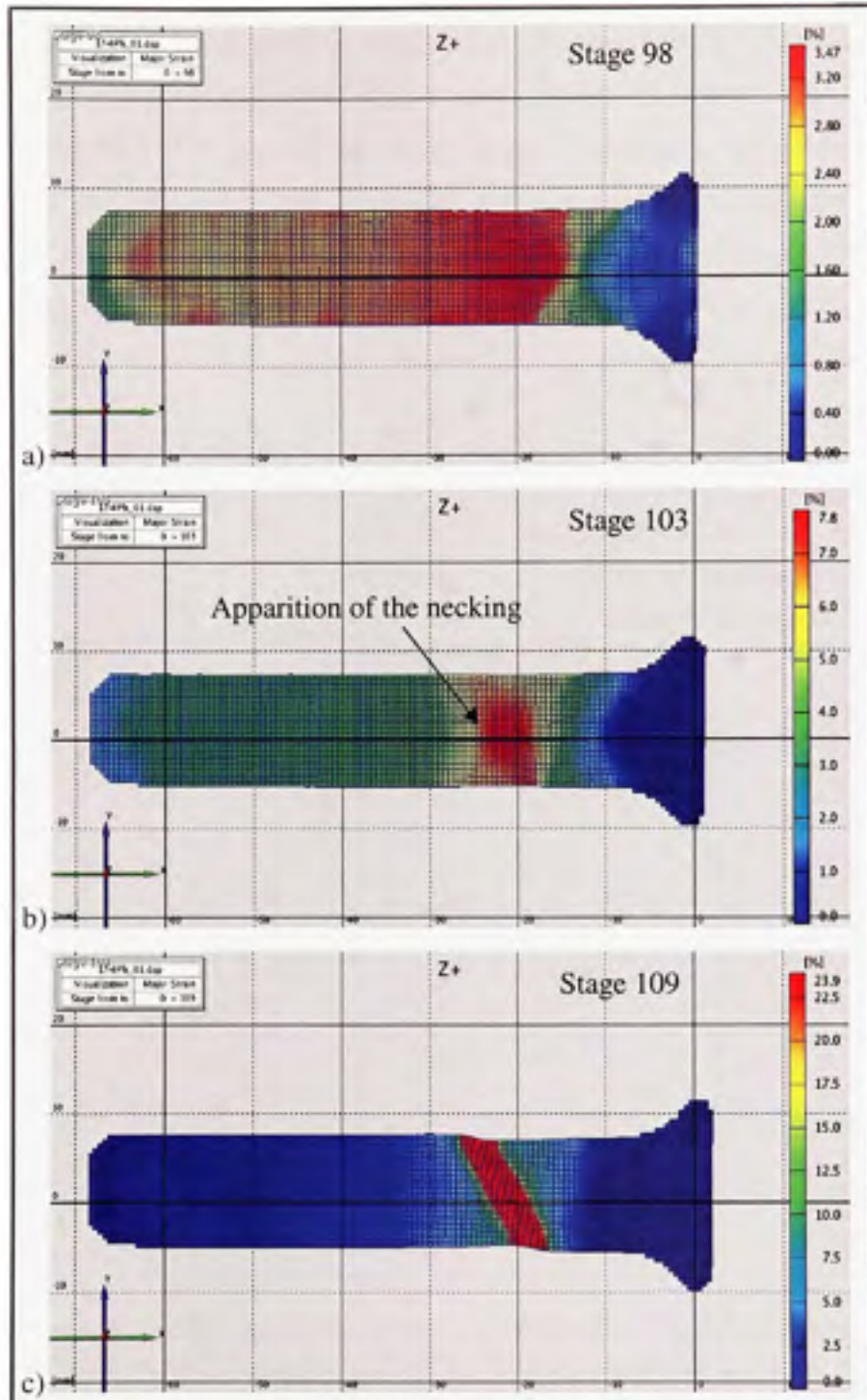


Figure 2.8 Images extracted from Aramis at different levels of deformation of a 17-4 PH specimen during tensile test

a) During uniform plastic deformation
 b) showing the neck location c) just before rupture.

Figure 2.8 shows three stages of deformation. The first stage is the uniform elasto-plastic deformation after a strain of 2.5%, the second corresponds to the appearance of the necking after a global strain of 4.8% and the third is at rupture. The stresses are calculated with the load data from the tensile machine. The recorded data of the load and the strain maps obtained from Aramis are synchronized in order to obtain the stress-strain curves. The engineering curves obtained from both tests are very closed. Figure 2.9 represents the average stress-strain curve of the samples compared to video-extensometer results.

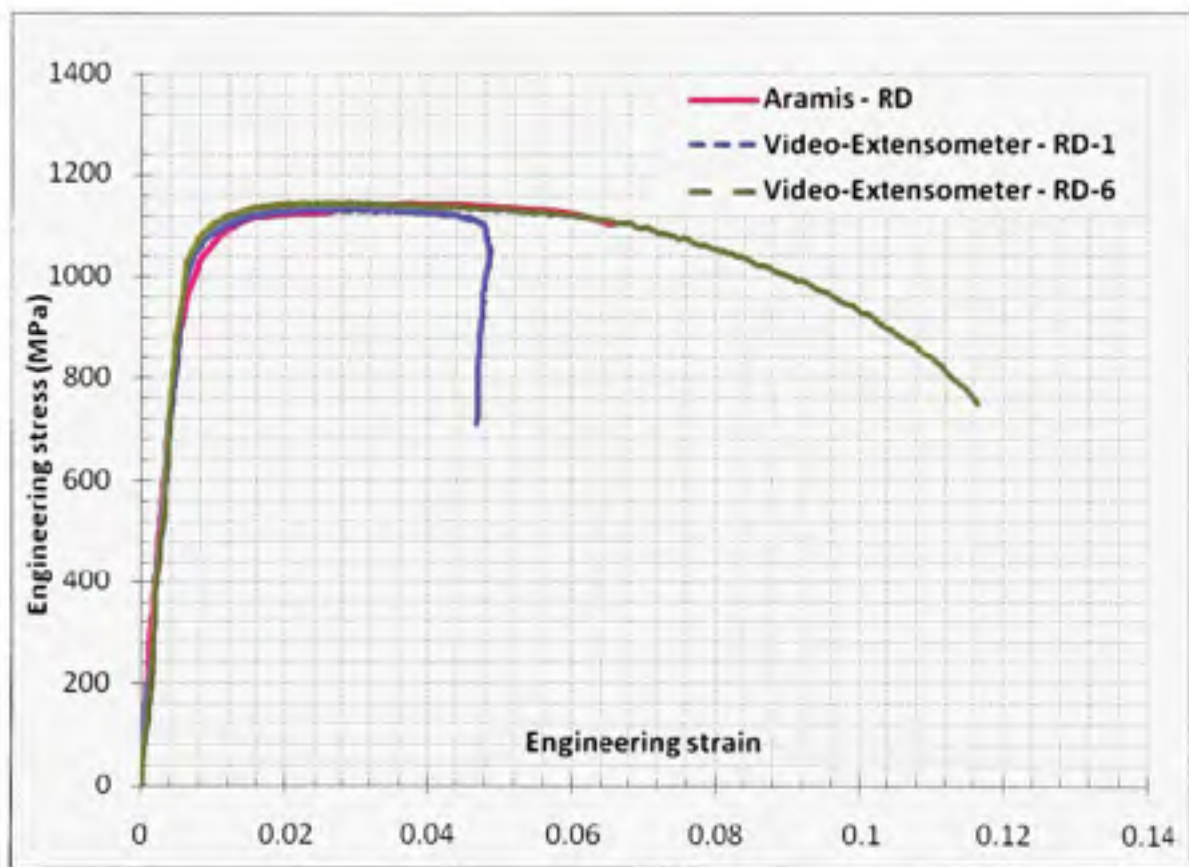


Figure 2.9 Tensile engineering stress-strain curve for 17-4 PH RD direction (Aramis) compared to curves 1 and 6 obtained by Video-Extensometer (Figure 2.4).

The strain reached at the end of the test is around 7 %. As the Aramis method covers the entire gauge length of the specimen, it is possible to follow the spatial localization of the deformation and the progressive apparition and development of the necking.

For SS 17-4 PH specimens, the elastic portion is large but it is not the case for all the materials and this low frequency is an issue due to the lower number of Aramis data points in the elastic part.

2.1.3 Choice of the characterization method

The video-extensometer method is a modern evolution of the conventional process to track the large deformation with mechanical extensometers. It can be very efficient and useful if the objective is just to extract stress-strain curves by drawing the dots in the center of the specimen and reducing the distance between the camera and the sample, the targets are well-defined during the entire test and accurate data in the range of uniform deformation can be obtained. The large number of measures brings additional precision to the calculation of some mechanical properties such as E or YS. On the contrary, if one wants to cover the whole specimen's gauge length and document the necking location, the number of dots should increase significantly and the distance to the sample as well. Consequently, a lot of precision is lost which is not interesting for our purposes.

The Aramis system is definitively more accurate in the plastic domain, precise and fit very well to our work. Its numerous functionalities give access to an optimized data acquisition and strains maps visualization. For material characterization, the local and global deformation can be tracked precisely and the onset of the necking can be identified accurately. Even if, the setting up is time consuming, this method is definitely more accurate for material characterization when it is essential to track precisely the necking location.

2.2 Mechanical tests

2.2.1 Tensile testing

The tensile testing is one of the most commonly used tests for material characterization. It consists of pulling a sample slowly until it breaks. During the process, force-displacement

data, a quantitative measure of how the test item deforms under an applied tensile force, are monitored and recorded (Miles, 2006). It is used to determine the stress-strain curves of materials. For sheet metals, the specimen is cut to dimensions specified by ASTM Spec A8 (ANNEX I). For tubes, tensile specimens are cut around the tube in the same way specified by ASTM. Tubes were cut in 90° intervals as shown in Figure 2.10.

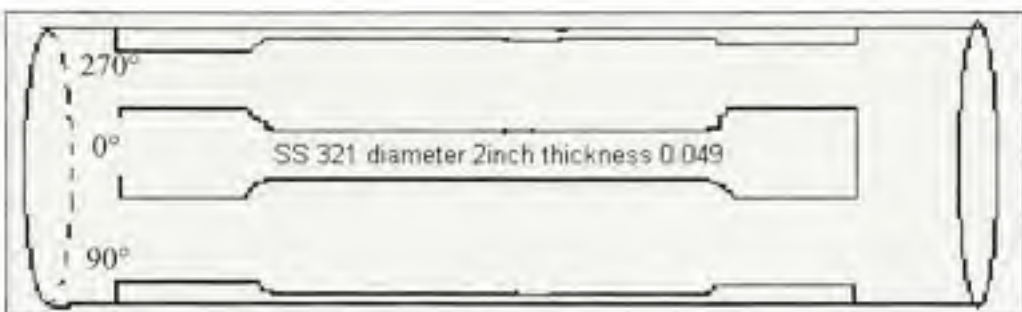


Figure 2.10 Orientation of tensile samples cut around a tube (curved specimens).

The tests were conducted on a MTS 810 hydraulic tensile machine under displacement control. The test procedure comes from previous tests conducted at AMTC on similar materials and consists on a stretch velocity about 0.04 mm/s until the yield strength and 0.16 mm/s from that point to the fracture. This receipt has been applied to materials with more than 40% elongation. For the others, a loading rate of 0.04 mm/s until rupture has been practiced. This jump on the loading rate resulted in a tiny jump in the stress-strain curves. During the test, the time, the axial displacement as well as the axial force are recorded. By using the time, force data from the tensile machine and the strain data from Aramis are correlated in order to evaluate the stresses and strain and build stress-strain curves.

The mechanical properties are evaluated based on the engineering stress-strain curve. To obtain the Young's modulus E, the elastic part is identified going from 0 to a point just before the curve slope changes from linear to curve. The slope of this part corresponds to E. A line is plotted parallel to the elastic part and YS is identified as the cross point between this line and the data points. In the case of SS 321, the elastic part was very short as YS is low and the record frequency of the data points associated to the Aramis system was also low. As

a result the number of points in the elastic part is too small and this affects a lot the precision in the evaluation of E. In fact, in this case, the calculation of YS has been done using a constant $E = 193 \text{ GPa}$ as given by the literature (Table 1.2).

The necking strain is evaluated as the strain reached at the UTS since the strain of the elastic return, for the studied materials, is small compare to global strain.

The tensile test is the simplest way to obtain quantitative measure of a material formability. Even if the deformation during a tensile test is only in one direction, it gives a very good idea of the mechanical properties of the material sheet or tube. In addition, it is very easy and inexpensive to carry out. As the objective of this work is to feed material models to hydroforming simulation and compare the predicted results with experimental data, it is essential to perform characterization tests which are as close as possible to the hydroforming process. Thus, some free expansion tests have been conducted in addition to the tensile tests to find the biaxial behavior of the material.

2.2.2 Free expansion test

In the case of hydroforming, the deformation of the tube is in two directions. So, many authors (Chen, Soldaat and Moses, 2004; Gholipour, Worswick and Oliviera, 2004; Koç, Aue-u-lan and Altan, 2001; Kuwabara and al., 2003; Levy, Van Tyne and Stringfield, 2004) consider that a flow curve (stress-strain curve) representing the biaxial behavior of the entire tube is more reliable than the extrapolation of a flow curve obtained from a tensile test. The free expansion test is used to determine mechanical properties in a biaxial state of strain. This process could be used for sheet as well as for tubes. But as the test procedures should be as close as possible to the hydroforming process only the material properties of tubes have been tested.

2.2.2.1 Procedure

The free expansion test are performed in a hydroforming press. In free expansion test, the tube is placed between the upper and lower dies, and closed using the hydraulic press. During the experiment, the tube is pressurized internally and the unclamped region deforms until burst. Figure 2.11 presents schematically the different steps of a free expansion test. The internal hydraulic pressure is measured continuously through the press control system. The bulge height and the tube deformation are recorded with the Aramis system. These data can be used to determine the effective stress versus the effective strain of the tube material in order to build the flow curves of the tube.

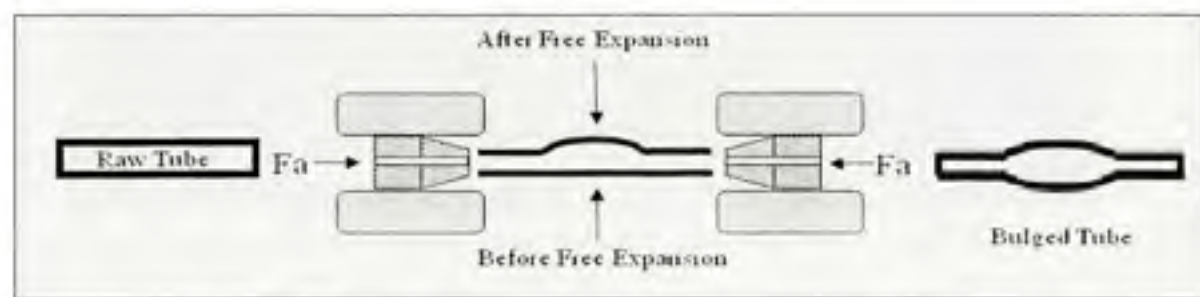


Figure 2.11 Schematic view of the free expansion process.

Adapted from Sanchez and Gholipour (2008)

Two types of tests can be performed. When an axial force (F_a) is applied, it is a free expansion test with End-feed. The tube expansion is then due to the combination of axial displacement and internal pressure whereas without end-feeding the axial displacement is blocked. With a test with End-feeding higher deformation is reached which is very interesting but it is very difficult to set up. In our case, only no end-feeding free expansion tests were run.

The hydroforming press used is located at AMTC. It is an Interlaken 1000-Ton press with 60 000 psi (413 MPa) pressure intensifiers to hydroform sheet or tube. A programmable pressure and position control ensures repeatability of the process. The associate control system gives access to the process parameters. During the test, the Aramis system is

positioned in front of the tube, as shown in Figure 2.12, and records images at a rate of 6 frames per second. The frequency of the frames could be increased for the free expansion tests because the deformation close to burst is much faster than the tensile test.

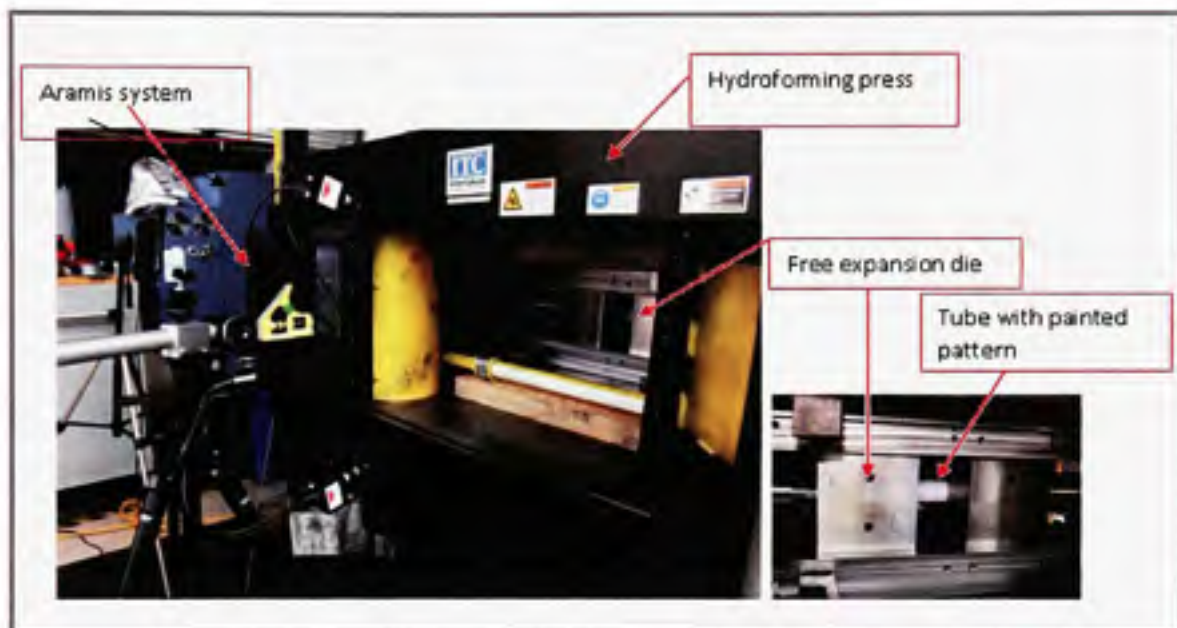


Figure 2.12 Free expansion test with Aramis set up.

From the Aramis, it is possible to extract the strain distribution along the tube during the test as well as the bulge height increase as a function of the time. The hydroforming press gives us the water pressure during the test. By correlating these two pieces of information, we can find the deformation history of the tube in term of stress versus strain data.

The Aramis system procedure applied for free expansion tests is similar to what is done for the tensile tests except that in the case of free expansion tests, the bulge height is extracted for the calculations. The deformation maps have been extracted to observe the strain distribution during the test.

2.2.2.2 Stress-strain curves from free expansion tests

The stress-strain curve extraction is essential for material characterization. Several works have been done based on analytical methods to obtain biaxial stress-strain curves from the bulge height as a function of the internal pressure extracted from the free expansion tests (Hwang, Lin and Altan, 2007; Koç, Aue-u-lan and Altan, 2001; Sokolowski and al., 2000). A matlab procedure based on these articles is developed to extract the stress-strain curves for FX tests. It is important to note that the details concerning the equations used for curves extraction presented here were not within the purpose of the present work and have been taken from Falco thesis (2008).

Theory

Several methods can be used to determine the tubular material properties: analytical method, finite element iterative method, energy balance method. The aforementioned authors reported different analytical methods based on force equilibrium theory. The one developed at AMTC draws its inspiration from Hwang and al. (2002); (2004); (2007).

Considering the bulge as an arc of ellipse, the two ends of the tube are fixed completely (no end-feed) and only the bulge height has to be measured. Figure 2.13 presents a schematic diagram of the tube bulging geometry including the main parameters took into account in the analysis.

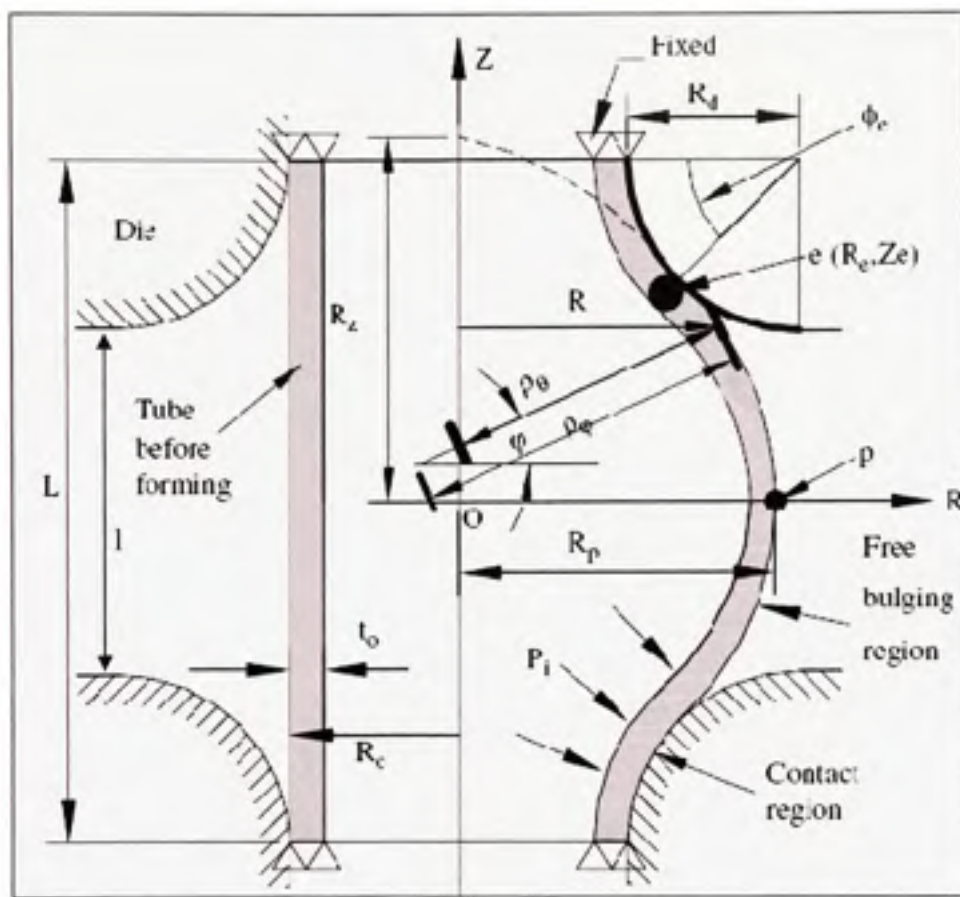


Figure 2.13 Schematic diagram of the bulge test with the geometrical parameters.

Adapted from Hwang, Lin, and Altan (2007)

The tubes ends being fixed, the strains at the pole are in the hoop and thickness directions and are evaluated by the following equations:

$$\varepsilon_\theta = \ln \left(\frac{R_p - (t_p/2)}{R_0 - (t_0/2)} \right) \quad (2.1)$$

$$\varepsilon_t = \ln \left(\frac{t_p}{t_0} \right) \quad (2.2)$$

with R_p the half length of the minor axes of the elliptical tube surface, t_p the tube thickness at the pole and R_0 and t_0 respectively the initial tube outer radius and the initial thickness. t_p is evaluated at every deformation steps using an iterative method and R_p is calculated from

geometrical considerations involving the coordinates of the contact point e, between the tube and the die:

$$R_p = \sqrt{R_e (R_e + Z_e \tan \phi_e)} \quad (2.3)$$

From the von Mises yielding criterion and the volume constancy, the effective strain is obtained as:

$$\bar{\varepsilon} = \frac{2}{\sqrt{3}} \sqrt{\varepsilon_\theta^2 + \varepsilon_\theta \varepsilon_t + \varepsilon_t^2} \quad (2.4)$$

For the calculations, it is assumed that the tubes are thin-wall. So, the stress state can be considered as a plane stress state. Figure 2.14 explained the state of stress at the bulge pole.

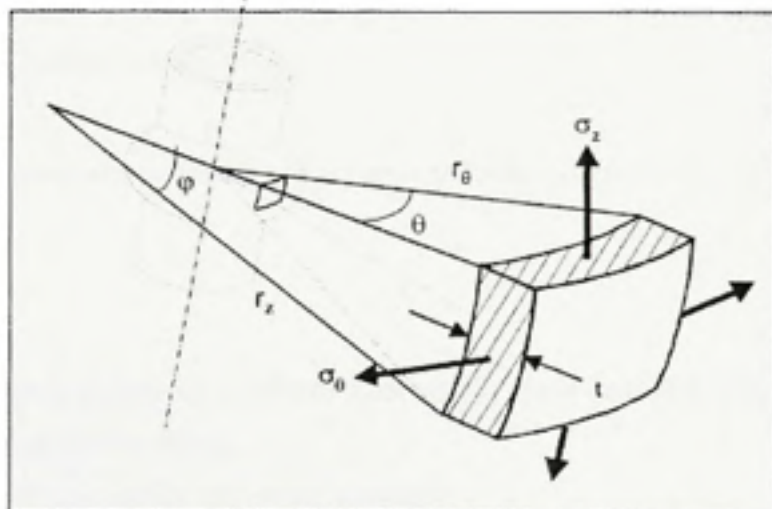


Figure 2.14 The state of stress at the tip of bulge region.
Adapted from Koç, Aue-u-lan and, Altan (2001)

The effective stress is then:

$$\bar{\sigma} = \sqrt{\sigma_\theta^2 - \sigma_\theta \sigma_\phi + \sigma_\phi^2} \quad (2.5)$$

To calculate the stresses, it is necessary to take into account the thickness reduction. Some mathematical equations are then required since the measurement of the thickness at each step of the deformation is not available:

- The force equilibrium for the element at the pole of the elliptical surface:

$$\frac{\sigma_\varphi}{\rho_{\varphi P}} + \frac{\sigma_\theta}{\rho_{\theta P}} = \frac{P_i}{t_p} \quad (2.6)$$

- The volume incompressible condition:

$$\varepsilon_\theta + \varepsilon_t + \varepsilon_\varphi = 0 \rightarrow \varepsilon_\varphi = (-\varepsilon_\theta + \varepsilon_t) \quad (2.7)$$

- The Lévy-Mises plastic equation:

$$\frac{\varepsilon_\varphi - \varepsilon_\theta}{\sigma_\varphi - \sigma_\theta} = \frac{\varepsilon_\theta - \varepsilon_t}{\sigma_\theta - \sigma_t} \quad (2.8)$$

with ε_θ , ε_t , ε_φ respectively the hoop, radial, and longitudinal strains, and σ_θ , σ_t , σ_φ the hoop, radial, and longitudinal stresses. ($\rho_{\theta P}, \rho_{\varphi P}$) are the radii in meridian and tangential directions at the pole P and P_i the internal pressure.

Based on all these equations, the biaxial stresses and strains can now be calculated from free expansion tests.

Matlab code

A matlab program is developed to obtain stress-strain curve with the AMTC's method that needs the following data as inputs:

- tube geometry: tube radius and initial thickness;
- die geometry: die radius (R_d) and distance between the dies (l) (dies free expansion zone);
- pressure and axial force (if necessary): output files from the press;
- bulge height: output file from Aramis.

The program reads directly the output files and the other values and starts the analysis. This program is fully described in the master thesis of Falco et al. (2008). A user-friendly interface has been built to allow the extraction of a stress-strain curve from the free expansion test. The input data are entered directly on the interface as shown in Figure 2.155

and the output files are uploaded inside a folder and the Matlab program interface plots the calculated stress-strain curve.

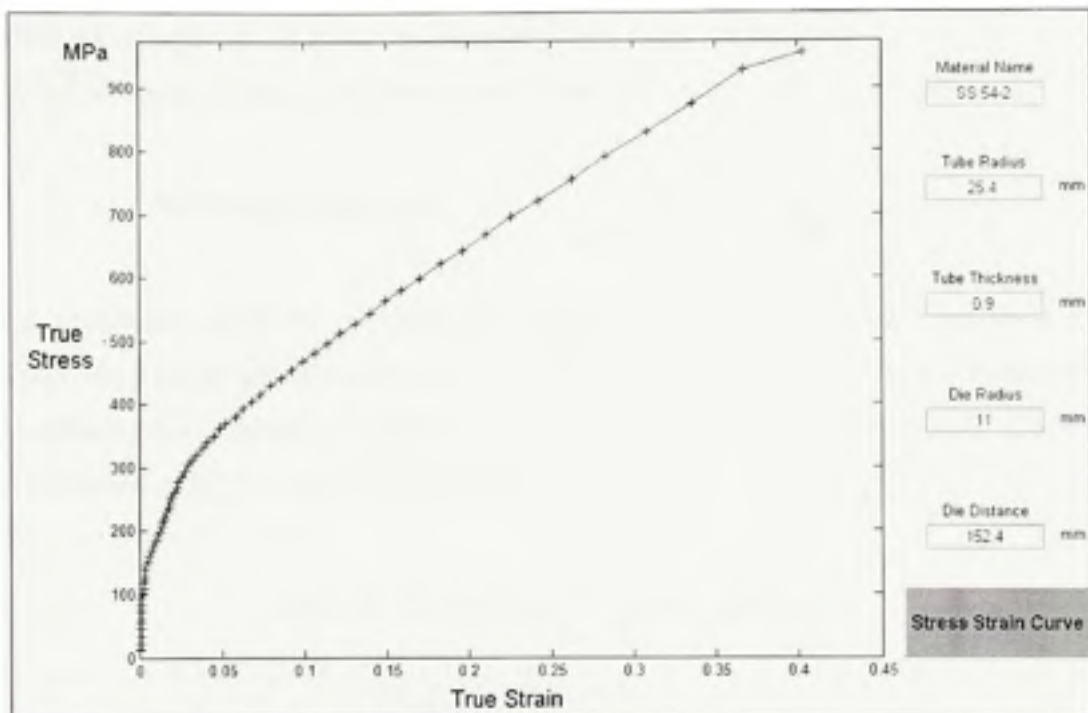


Figure 2.15 Matlab program interface.

The Matlab code is in development to increase the accuracy of the biaxial stress-strain curves by improving the bulge height measurement, reading the thickness values from Aramis during the test, and reducing the number of assumptions.

The stress strain curves obtained by the mechanical tests are used to generate the hardening equations essential for the FEM simulations. In order to automate their extraction and generate the appropriate hardening coefficients in each deformation case, a methodology developed to extract the necessary data from the curves is described in the next chapter.

2.3 Hardening laws extraction

This section will explain the process developed to extract the appropriate hardening coefficients in each material law to see which one best fit the stress-strain data obtained either by the tensile tests or calculated based on the free expansion tests for the materials.

2.3.1 Hardening equations

Many constitutive equations were proposed to describe the work hardening behavior of the material. They are empirical relationships between the true stress and the plastic true strain. The hardening laws chosen to describe the flow behavior of the studied aerospace alloys have been presented in 1.1.3.3 and are listed below:

Table 2.1 Considered constitutive equations

| Name | Flow Relationships |
|-----------|---|
| HOLLOMON | $\sigma = K_H \times \varepsilon_p^n$ |
| LUDWIK | $\sigma = \sigma_0 + K_L \times \varepsilon_p^n$ |
| LUDWIGSON | $\sigma = K_L \times \varepsilon_p^n + \exp(K_1 + n_1 \varepsilon_p)$ |
| VOCE | $\sigma = \sigma_V - K_V \times \exp(n_V \varepsilon_p)$ |
| SWIFT | $\sigma = K_S \times (\varepsilon_0 + \varepsilon_p)^n$ |

In these equations, K and n represent the strength coefficient and the strain-hardening exponent respectively. σ_0 and $\exp(K_1)$ correspond to the yield strength and in the Ludwik and Ludwigson equations respectively and ε_0 , in Swift, can be consider as the amount of strain hardening that the material received prior to the tension test (Datsko, 1966, pp. 18-20). In Ludwigson, n_1 is a parameter able to quantify the deviation of stress from the conventional

power law (Hollomon) (Datsko, 1966; Moosbrugger, 2002). The Voce's coefficients K_v and n_v are defined as materials constants.

2.3.2 Fitting method

The fitting method used in this work is the least squares one. This method is widely used for regression analysis. It consists on minimizing the difference between experimental data and modeled data in the least square sense. In other words, the best fitted model will have its sum of squared residuals minimized (the residual in being the difference between an observed value and the value provided by the model). In other words, the residual is a fitting error. The objective of a fitting analysis is to adjust the parameters of a model function to best fit all the data in a given set. In our case, the models are all the potential hardening equations and the data set is the stress-strain data obtained from tensile or free expansion tests. The various steps of the least-squares fitting methods are detailed below for the Hollomon equation:

- let $(\sigma_i, \varepsilon_i)$, $i = 1, \dots, n$ be a data set with ε_i as an independent variable and σ_i a dependant variable. $(\sigma_i, \varepsilon_i)$ is considered as a pair;
- let choose the Hollomon equation as the model function: $\sigma_H = K * \varepsilon_H^n$ where K and n are the adjustable parameters;
- the residual of each pair of data can be calculated: $r_i = \sigma_i - \sigma_{Hol,i}(K_{Hol}, n)$ where σ_i is the experimental data and $\sigma_{Hol,i}$ is the predicted strain with the Hollomon model;
- the sum of the residual squares have to be minimized for best fitting in a least squares sense: $S - R = \sum_{i=1}^n r_i^2$;
- the optimized K and n parameters are found as well as the best fitted calculated stress.

Since all the stress-strain curves do not contain the same number of data points on the uniform plastic deformation range, to evaluate and compare the quality of the fit, a new parameter S/N, which corresponds to S divided by the number of points, is introduced.

2.3.3 Matlab program

In order to automate the characterization process notably the fitting step and apply it to all the collected data, a Matlab program has been implemented.

2.3.3.1 Procedure

The inputs for the Matlab program are the true stress data and the corresponding true strain data, as well as the starting point for the coefficients to lead the iterations. The outputs are a plot of the σ - ϵ data as well as the fitted curves, a table of the coefficients of each law and a file containing the calculated stresses for each law using the obtained best-fit coefficients.

2.3.3.2 Main program

The entire program can be found in ANNEX II. The program flowchart is resumed in Figure 2.16.

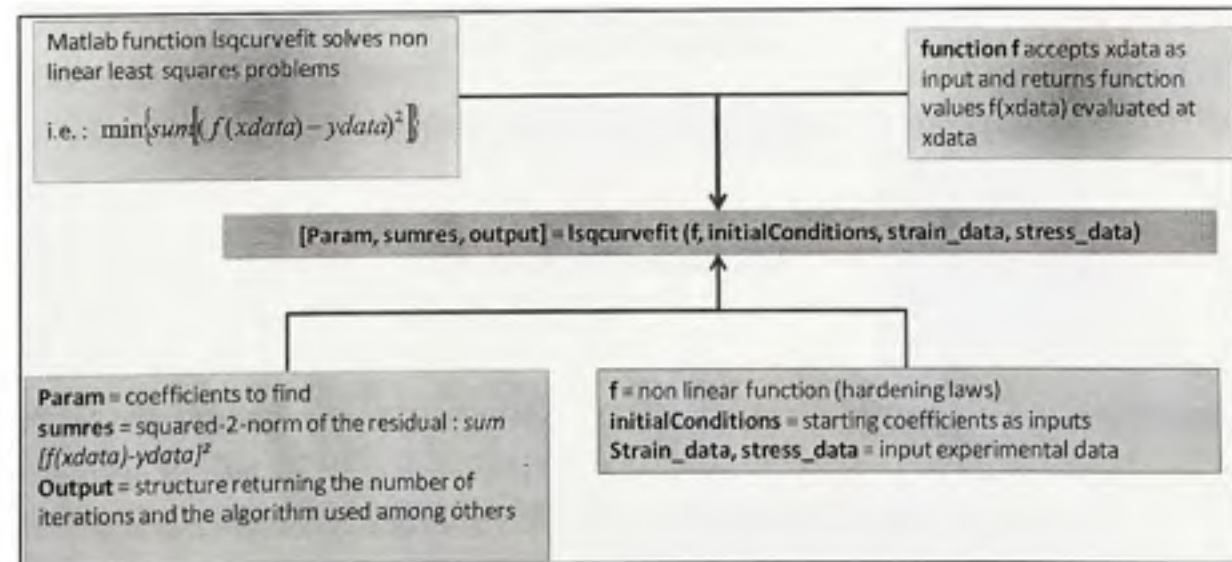


Figure 2.16 Diagram presenting the Matlab main program.

The Matlab function used, *lsqlcurvefit*, solves non linear least squares problems. The input arguments are then each non-linear hardening equation, the starting coefficients, and the experimental true stress and strain data. The starting coefficients give a starting point to the program and, when they are well-chosen, allow a reduction of the calculation time and the number of iterations. The output arguments are a matrix containing the coefficients to find, the sum of the squared residuals of the best solution and the output structure which give information on the optimization itself.

2.3.3.3 Block diagram

The diagram shown in Figure 2.17 simplifies the procedure used inside the Matlab program. The hardening equations are placed inside subroutines called one after the other. The results of the fitting are written in a table.

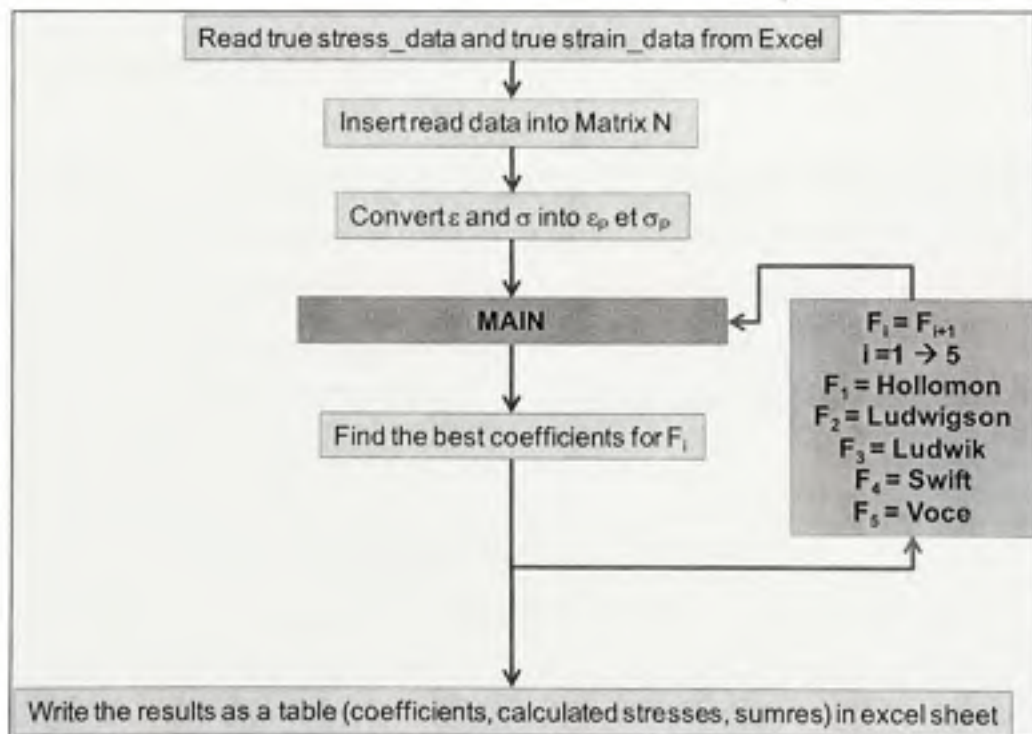


Figure 2.17 Matlab block diagram to find hardening laws best coefficients.

CHAPTER 3

ON THE EFFECT OF SPECIMEN GEOMETRY (SS 321)

This chapter is concerned with the set up of the mechanical characterization for hydroforming. As detailed in section 1.2, the mechanical test performed to obtain the material properties as well as the specimen geometry are crucial elements for appropriate future material models. Various specimens' geometries, from flat sheet to tube, have been tested on one aerospace alloy to study the impact of the specimen geometry on the obtained hardening equations. The characterization method conducted is enforced step by step. This approach is completely opposite to a batch to batch comparison and is relevant to find the appropriate characterization method. Both tensile and free expansion tests have been performed and only the Aramis system has been chosen to record the deformation of the specimens. All the tests have been performed at AMTC.

3.1 From sheets (flat samples)

Flat samples are particularly relevant for anisotropy measurements. The samples tested have been cut in the three directions of a given sheet as presented in Figure 2.1. The studied directions are the Rolling Direction (RD), the Transverse Direction (TD) which is 90° from the RD and the 45° Direction (45D) which is between the RD and the TD. The objective is to study how the properties can be different from one direction to the next and what is the repercussion on the hardening laws.

3.1.1 Stress-Strain curves and mechanical properties

Figure 3.1 presents the engineering stress-strain curves obtained in the three directions using Aramis. Every test is repeated twice and a third test is eventually performed if significant variations are found. The curves displayed correspond to the average of two to three tests.

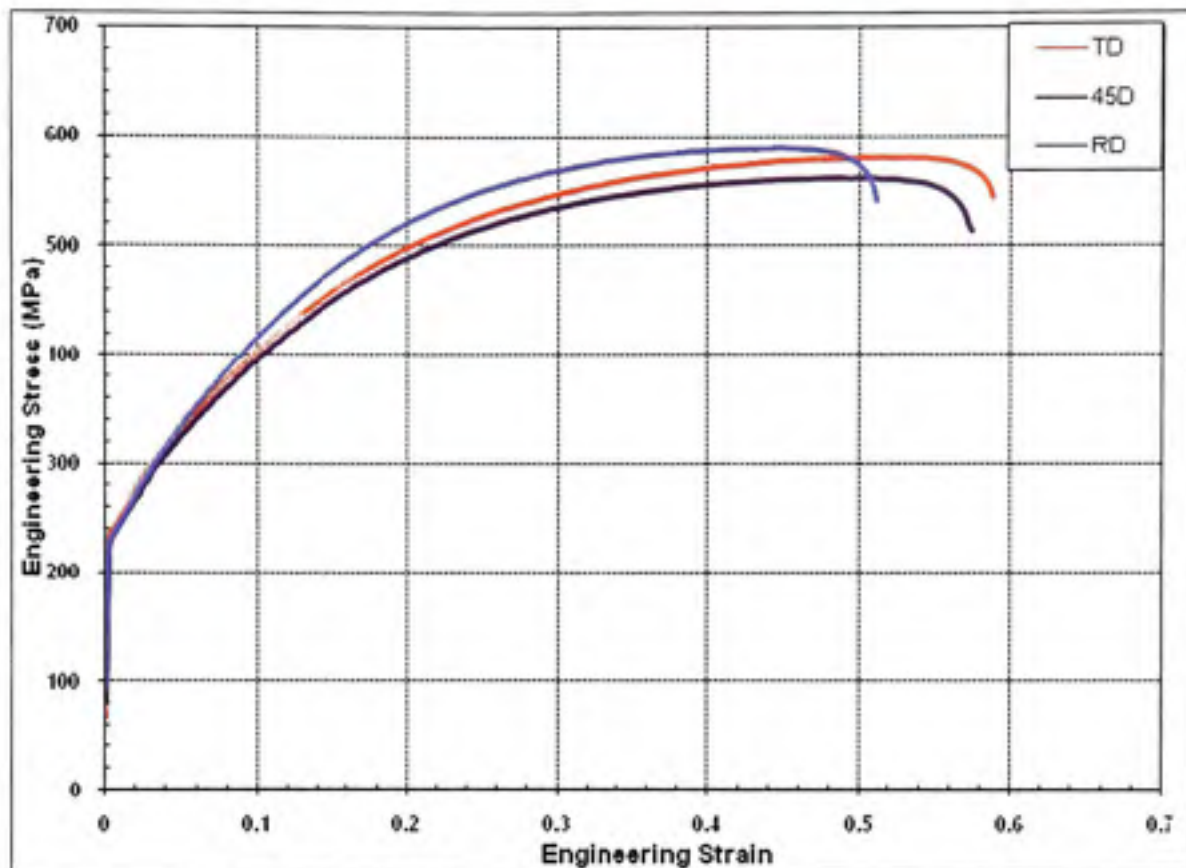


Figure 3.1 Engineering stress-strain curves of SS 321 flat samples (1 mm thickness) in the three directions.

The elastic zones of the curves are similar and the plastic zones are slight different even if the curves shape remains the same. The effect of the direction is more visible beyond the YS until the rupture. The differences can be quantified better with Table 3.1.

Table 3.1 Mechanical properties of SS 321 flattened samples in 3 directions

| | E (GPa) | YS (MPa) | UTS (MPa) | Necking strain | Breaking strain |
|------------------|---------|----------|-----------|----------------|-----------------|
| 321 - RD | 183 | 230 | 592 | 0.453 | 0.515 |
| 321 - 45D | 193 | 229 | 564 | 0.488 | 0.578 |
| 321 - TD | 165 | 241 | 584 | 0.518 | 0.594 |

A significant variation of E is observed in Table 3.1. As mentioned in section 2.2.1, the procedure used to extract E does not allow its precise evaluation. Some improvements have to be considered such as the increase of the Aramis frame rate in order to increase the number of data recorded particularly in the elastic part or the addition of a laser extensometer for the same purpose. The evaluation of YS, conducted with a constant E seems to be unaffected by the material anisotropy: approximately, 2% differences are notified.

In addition, some textures measurements have been conducted to bring out the possible presence of some morphological textures. Texture is the distribution of the crystallographic orientation of grains constituting a given polycrystalline material. This measurement allows the evaluation of the anisotropy of material properties. In other words, the value of a measured property could depend on the crystallographic direction in which it is measured. By measuring the texture, we can notice if a polycrystal possesses preferred grains orientations. The common way of representing textures is to project the crystal orientation into the sample coordinates system in a pole figure. The Orientation Distribution Function (ODF), which a three dimensional representation of orientations distribution is required for quantitative evaluation of textures.

XRD texture was measured on a polished surface of samples using BRUKER D8 X-ray diffractometer equipped with a cobalt-target tube ($\lambda=1.78\text{\AA}$). Three measured incomplete pole figures of {111}, {200} and {220} were analyzed and the ODF and complete pole figures were recalculated by TextTools software. TextViewer software was used to analyze the texture results. Figure 3.2 displays the pole figures obtained for these planes.

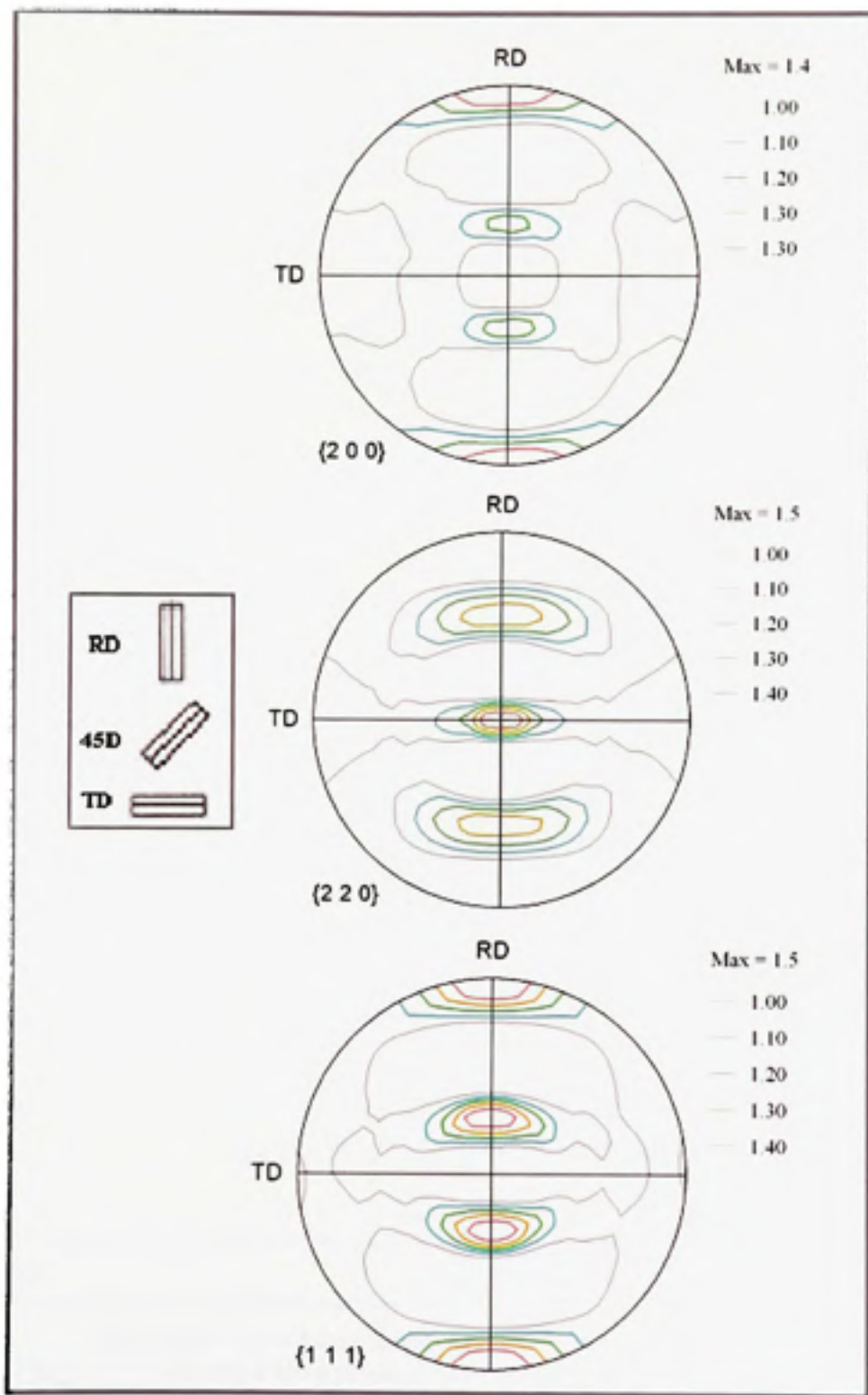


Figure 3.2 Pole figures of SS 321 on respectively
{2 0 0} {2 2 0} {1 1 1} diffracting planes.

Whatever the crystallographic direction considered, the crystallographic textures measured are very weak. The maximum intensity on pole figures is 1.5 which is too low to consider an effect of the orientation. The randomness of the texture confirms that the young modulus should have been the same in any direction. The differences observed among the mechanical properties could not be due to a crystallographic texture. The grain size and shape can generate some dispersion in the mechanical properties.

3.1.2 Hardening equations

The plastic stress-strain curves of specimens on the 3 directions have been plotted into a logarithmic scale as shown by Figure 3.3 in order to evaluate directly the hardening coefficients.

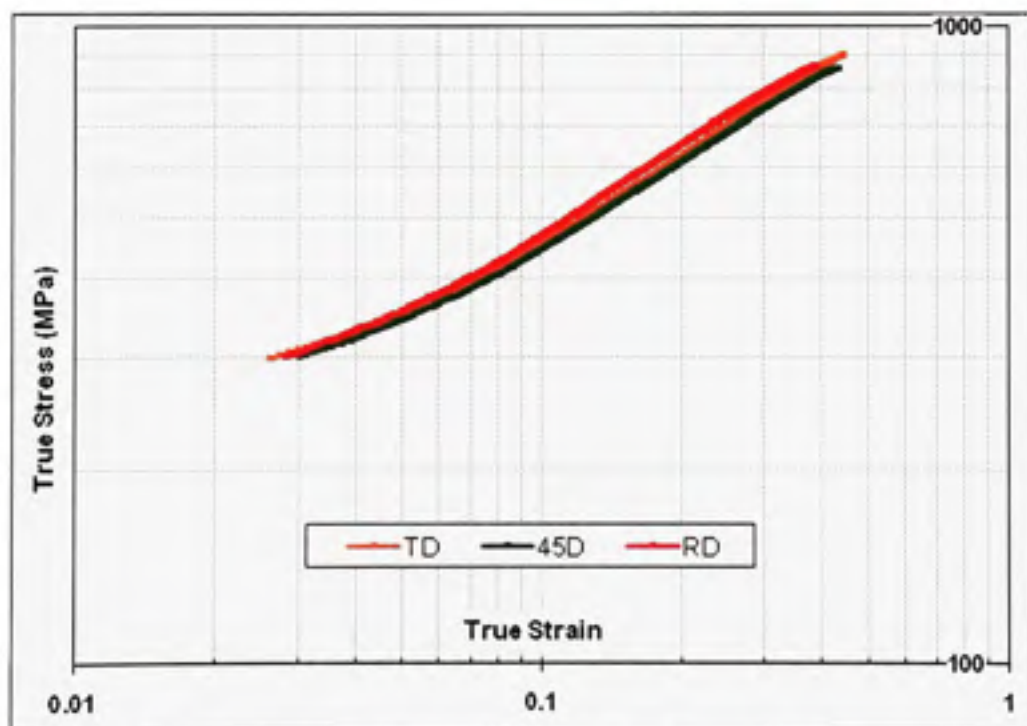


Figure 3.3 True stress-strain curves of SS 321 specimens on the 3 directions in the logarithmic scale.

The data, when plotted in the logarithmic scale, doesn't show any significant difference. So, to present the detail steps of the hardening equations extraction, the section will focus on the RD direction specimens only. Figure 3.4 presents the SS 321 RD data fitted by the hardening equations.

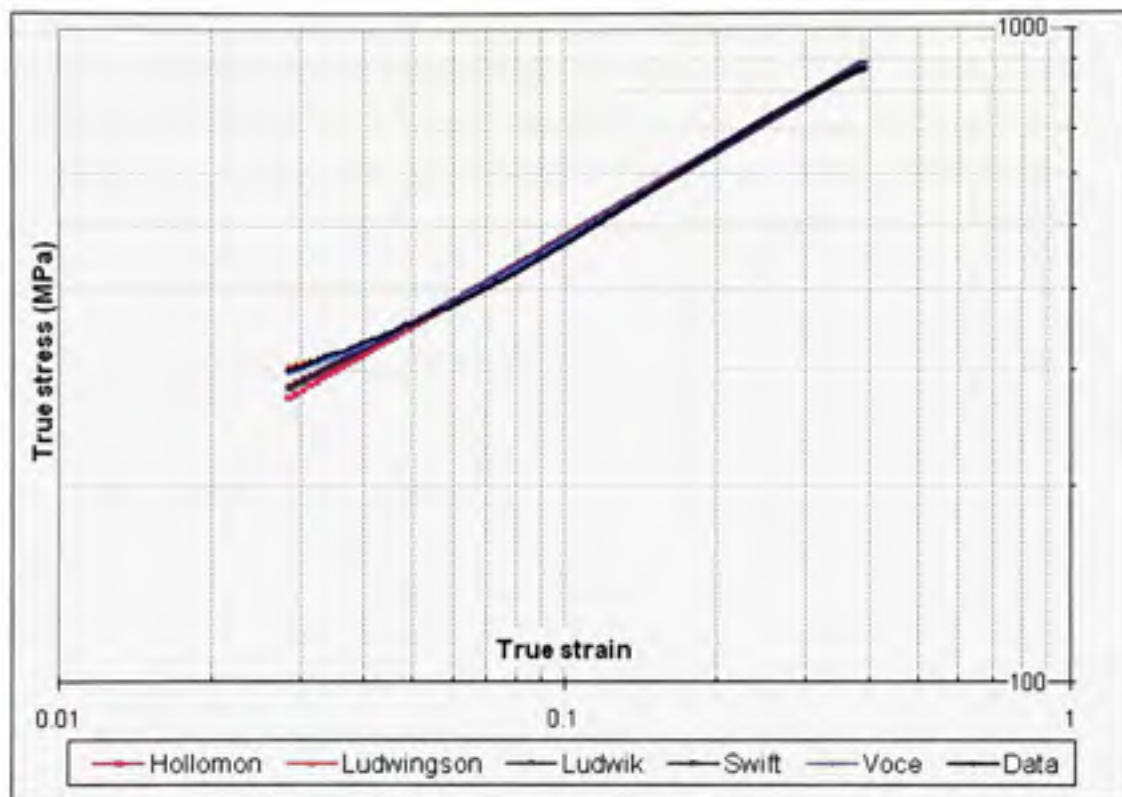


Figure 3.4 True stress-strain curves of SS 321 RD specimen fitted by calculated hardening equations in the logarithmic scale.

All the hardening equations seem to well fit the stress-strain data. Some dispersion is observed only on the strain range up to 4% (the beginning of the plastic strain). This difference can be attributed to the instabilities observed at the beginning of the plastic strain region. In fact, the transfer from the elastic part to the plastic zone is performed gradually in most of metallic materials. Thus, the use of a fixed point (offset yield strength) as the starting point of the plastic zone leads to some variations at the beginning of the curve. Table 3.2 gives the hardening coefficients of all the equations that fit the stress-strain data of SS 321 in the rolling direction.

Table 3.2 Best fit coefficients of the tested hardening equations – SS321 RD

| RD | Hollomon $\sigma = K \varepsilon_F^n$ | Ludwigson $\sigma = K \varepsilon_F^n + \exp(K_1 + n_1 \varepsilon_F)$ | Ludwik $\sigma = \sigma_0 + K \varepsilon_F^n$ | Swift $\sigma = K (\varepsilon_0 + \varepsilon)^n$ | Voce $\sigma = \sigma_v - K_v \exp(n_v \varepsilon_F)$ |
|-----|--|---|---|---|---|
| K | 1333.7 | 1348.1 | 1312.8 | 1356.9 | $K_v = 900.4$ |
| n | 0.4460 | 0.4542 | 0.4900 | 0.4700 | $n_v = -3.2968$ |
| | | $K_1 = 5.7395$ $n_1 = -73.8085$ | $\sigma_0 = 51.98$ | $\varepsilon_0 = 0.0077$ | $\sigma_v = 1117.9$ |
| S/N | 42 | 20 | 37 | 33 | 2 |

The S/N given into Table 3.2 shows roughly the qualitative fitting error of the best-fit equations. The lower is the S/N the better is the fitting. Based on Figure 3.4 and Table 3.2, it seems that the Voce equation represents the best-fit equation followed by the Ludwigson equation. The Ludwik and Swift equations are equivalents and the Hollomon leads to be the least accurate. In the same manner, the S/N follows the number of fitting parameters, that is to say the more parameters the equation contains the best will be the fitting. Even if some differences between the S/N of the equations are observed, nothing can discriminate one equation to the other at this level. All the coefficients found fit properly the experimental data.

In order to predict the appropriate equations in the levels of deformation reached during the hydroforming process, the strain has been increased up to 100% in Figure 3.5 using the equations. This extension is fundamental for FEM needs because of the underestimation of the deformation during a tensile test compared to the one produced by hydroforming as detailed in section 1.2.

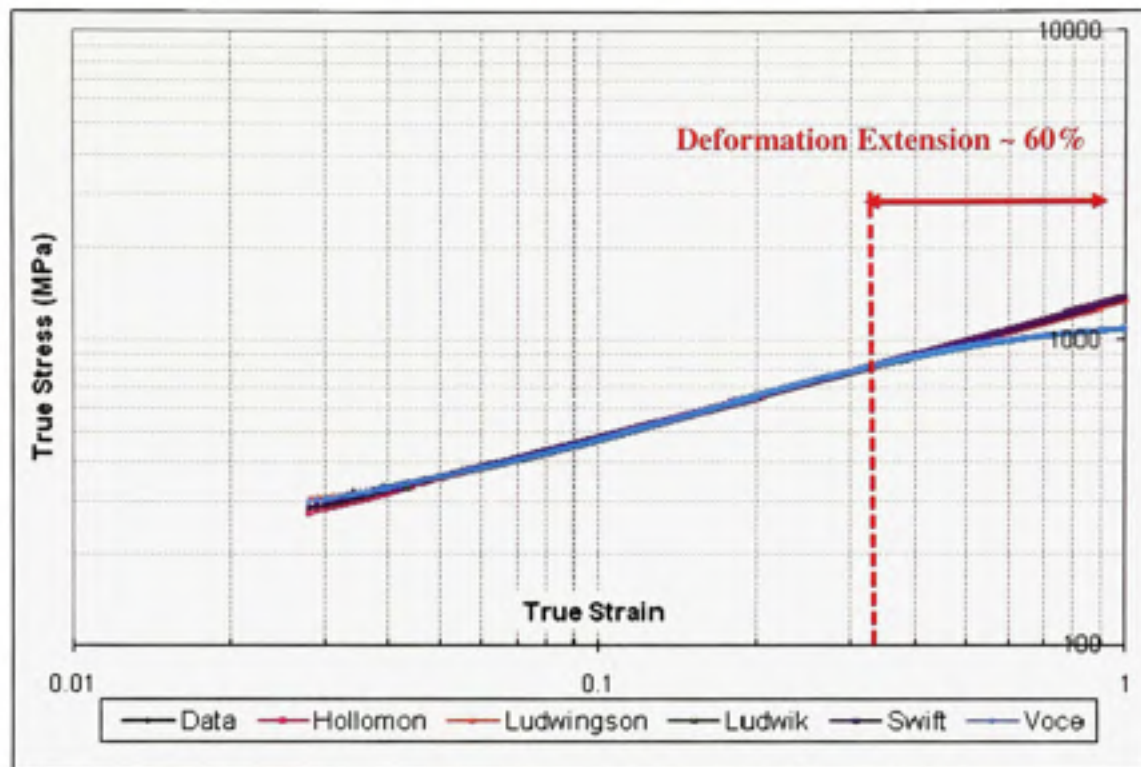


Figure 3.5 True stress-strain curves of SS 321 RD specimen fitted by calculated hardening equations extended to higher strain levels.

When the fitting results are extended up to 100%, a small divergence is observed. The fitted stress-strain curves have been plotted in the normal scale to evaluate better the differences observed for different hardening equations as shown in Figure 3.6.

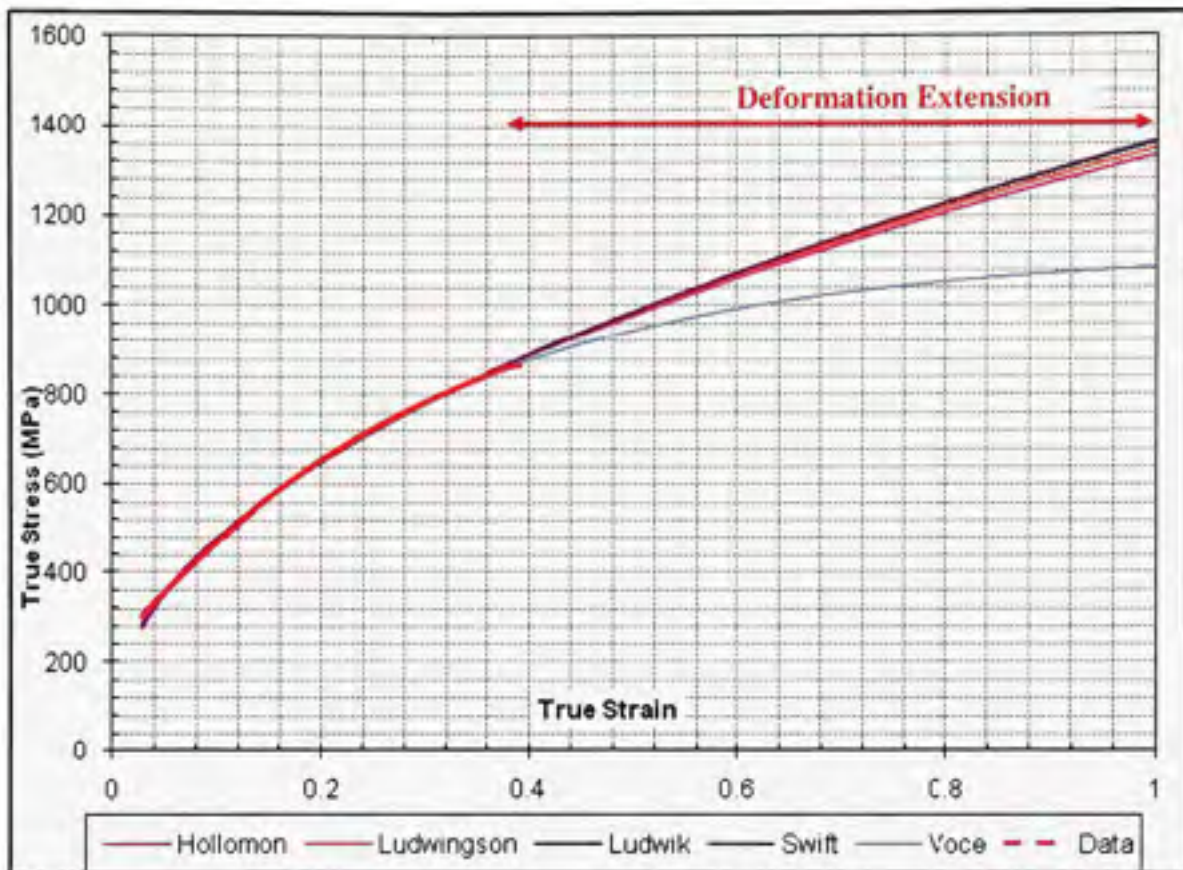


Figure 3.6 True stress-strain curves of SS 321 RD specimen fitted by calculated hardening equations extended up to 100%.

Except the Voce curve, all the other curves remain closed to each other. Depending on the equation chosen to build the material model, the extended curve will be very different. So, only the FEM simulations will be able to differentiate one constitutive equation from the others.

3.1.3 Effect of the orientation on the hardening equations

The same work presented in section 3.1.2 for the RD direction has been conducted on specimens on the other directions (45D & TD) and the results are presented in ANNEX III. The best fit coefficients obtained for these directions are presented respectively in Tables 3.3 and 3.4.

Table 3.3 Best fit coefficients of the tested hardening equations – SS321 45D

| 45D | Hollomon $\sigma = K \varepsilon_P^n$ | Ludwigson $\sigma = K \varepsilon_P^n + \exp(K_1 + n_1 \varepsilon_P)$ | Ludwik $\sigma = \sigma_0 + K \varepsilon_P^n$ | Swift $\sigma = K (\varepsilon_0 + \varepsilon)^n$ | Voce $\sigma = \sigma_v - K_v \exp(n_v \varepsilon_P)$ |
|------------|---|--|--|--|--|
| K | 1255.2 | 1274 | 1214.6 | 1287.8 | $K_v = 918.7$ |
| n | 0.4432 | 0.4555 | 0.5291 | 0.4857 | $n_v = -2.7230$ |
| | | $K_1 = 5.3838$ $n_1 = -51.5864$ | $\sigma_0 = 92.53$ | $\varepsilon_0 = 0.0153$ | $\sigma_v = 1145.4$ |
| S/N | 44 | 7 | 24 | 19 | 1 |

Table 3.4 Best fit coefficients of the tested hardening equations – SS321 TD

| TD | Hollomon $\sigma = K \varepsilon_P^n$ | Ludwigson $\sigma = K \varepsilon_P^n + \exp(K_1 + n_1 \varepsilon_P)$ | Ludwik $\sigma = \sigma_0 + K \varepsilon_P^n$ | Swift $\sigma = K (\varepsilon_0 + \varepsilon)^n$ | Voce $\sigma = \sigma_v - K_v \exp(n_v \varepsilon_P)$ |
|------------|---|--|--|--|--|
| K | 1301.6 | 1330.4 | 1253.4 | 1349.6 | $K_v = 1014$ |
| n | 0.4509 | 0.4692 | 0.5783 | 0.5146 | $n_v = -2.4022$ |
| | | $K_1 = 5.1262$ $n_1 = -38.1935$ | $\sigma_0 = 129.44$ | $\varepsilon_0 = 0.0232$ | $\sigma_v = 1151.9$ |
| S/N | 71 | 3 | 19 | 14 | 1 |

As observed for the mechanical properties, the material anisotropy seems not to have an important effect on the hardening coefficients. This material can be considered as isotropic. Nevertheless, no conclusions can be done about the choice of the best equation to describe the material behavior during multiaxial loading because any differences in coefficients may affect the subsequent material behavior in HF.

3.2 From curved specimens

This section will focus on the mechanical properties of curved specimens in comparison with flattened ones and also on the impact of the tube thickness on the hardening equations extraction.

Tensile specimens have been prepared from 50.8 mm (2") outside diameter seamless SS 321 tubes with two different wall thicknesses: 0.9 mm (0.035") and 1.2 mm (0.049"). These "curved specimens" have been machined from a tube at positions located by the angles as

shown in Figure 2.10. Most likely it is roll forming with floating mandrel. Because the tubes are seamless, it is expected that they do not have any differences regarding the position of the specimen in the tube. Thus, the manufacture label being the only written thing on the tube, it has been chosen as the reference and set as 0° position. This choice is completely random and do not have any physic explanation. The cutting orientations are in 90° interval in clockwise rotation starting at the written label-front.

3.2.1 Stress-strain curves and mechanical properties

Two tests have been conducted in each position. As the results concerning the absence of angular variations are similar for both thicknesses, they have been plotted all only for 0.9 mm in Figure 3.7 (all the data for the 1.2 mm specimens are presented in ANNEX IV).

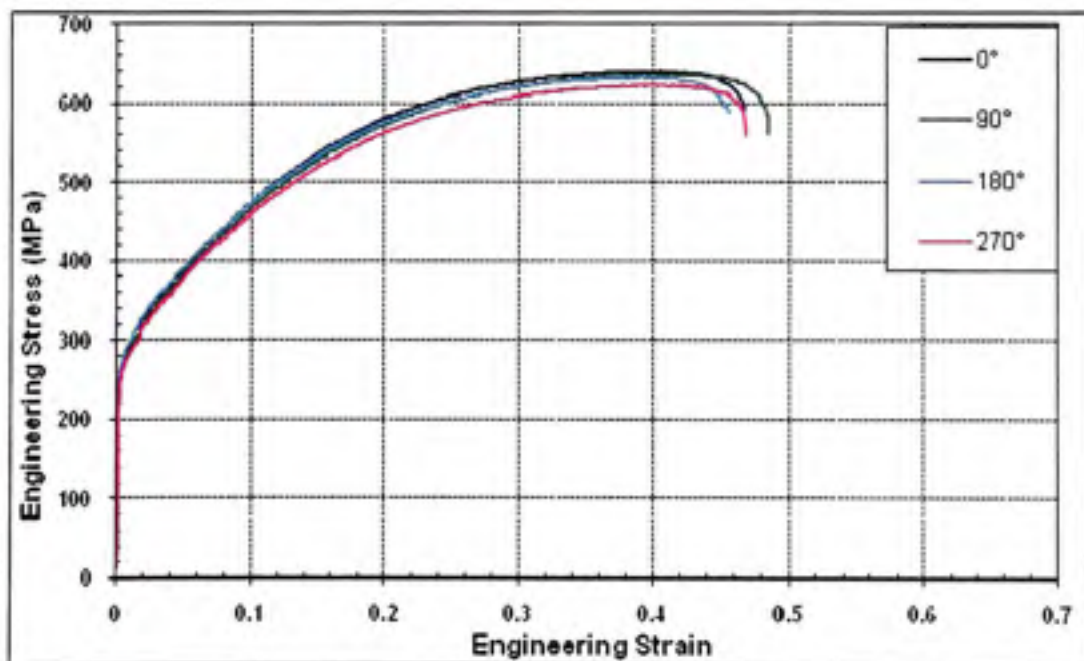


Figure 3.7 Engineering stress-strain curves of SS 321 curved samples cut around the tube – 0.9 mm thick.

The curved specimens present the same mechanical behavior. Only the 270° specimen seems slightly under shift. The mechanical properties presented in Table 3.5 have been obtained with less than 5% error in each case.

Table 3.5 Mechanical properties of SS 321 curved specimens– 0.9 mm thick

| 0.9 mm thick | YS (MPa) | UTS (MPa) | Necking strain | Breaking strain |
|-------------------------------|----------|-----------|----------------|-----------------|
| 321 – 0° | 269 | 641 | 0.405 | 0.472 |
| 321 – 90° | 263 | 637 | 0.413 | 0.488 |
| 321 – 180° | 271 | 633 | 0.391 | 0.461 |
| 321 – 270° | 261 | 623 | 0.407 | 0.470 |
| Average | 266 | 633 | 0.404 | 0.473 |
| Standard Deviation | 4.64 | 7.61 | 0.009 | 0.011 |

The stress-strain curves as well as the mechanical properties extracted from the four tensile tests around a tube are very closed to each other. An average curve has been plotted in Figure 3.8 to represent the behavior of the curved specimens and compare it to sheet specimen behavior.

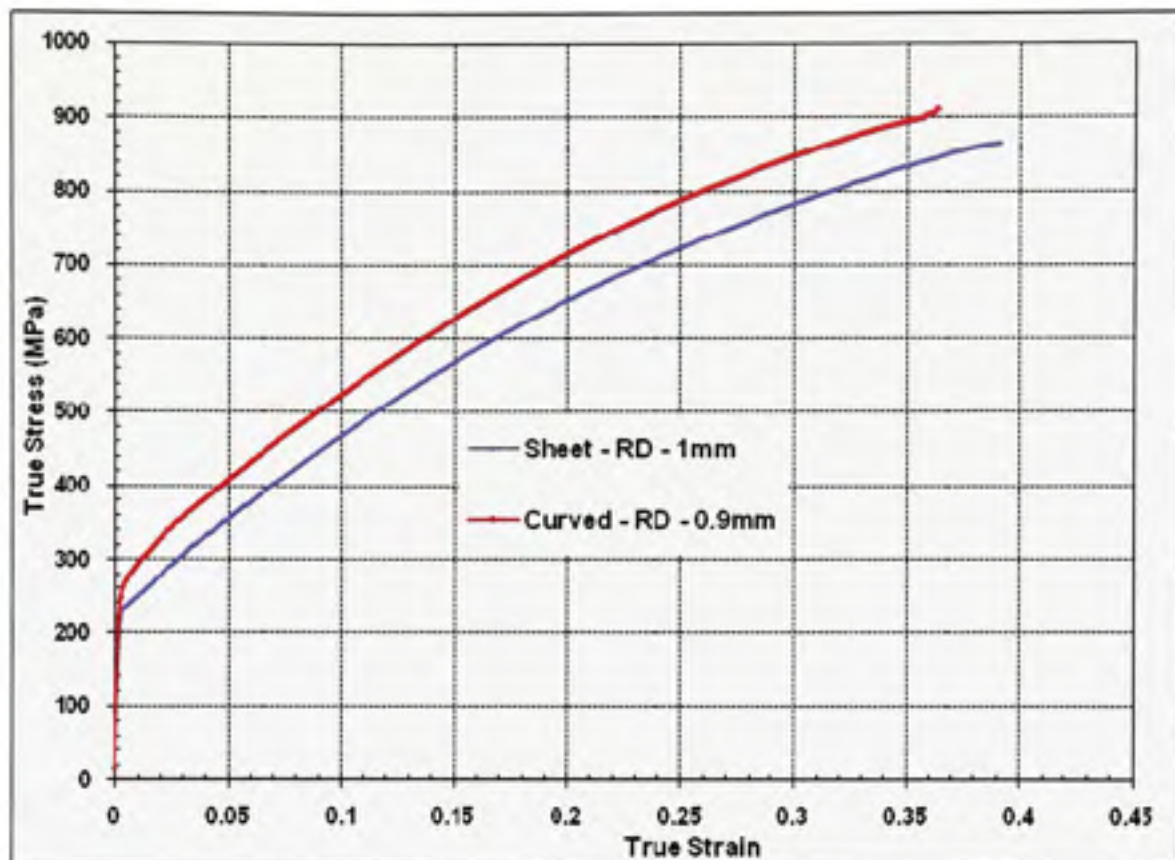


Figure 3.8 Comparison of true stress-strain curves of SS 321 curved samples (0.9mm thick) vs. flat samples (1mm thick).

The stress-strain curves present a similar shape. The curve for the flat samples is 50 MPa lower than the curve for the curved samples. This difference could be explained by a possible difference in grain size.

3.2.2 Hardening equations

To make easier the extraction of the hardening equations for curved specimens, the average true stress-strain curve has been considered. The calculated curves with the best fit coefficients are plotted in Figure 3.9.

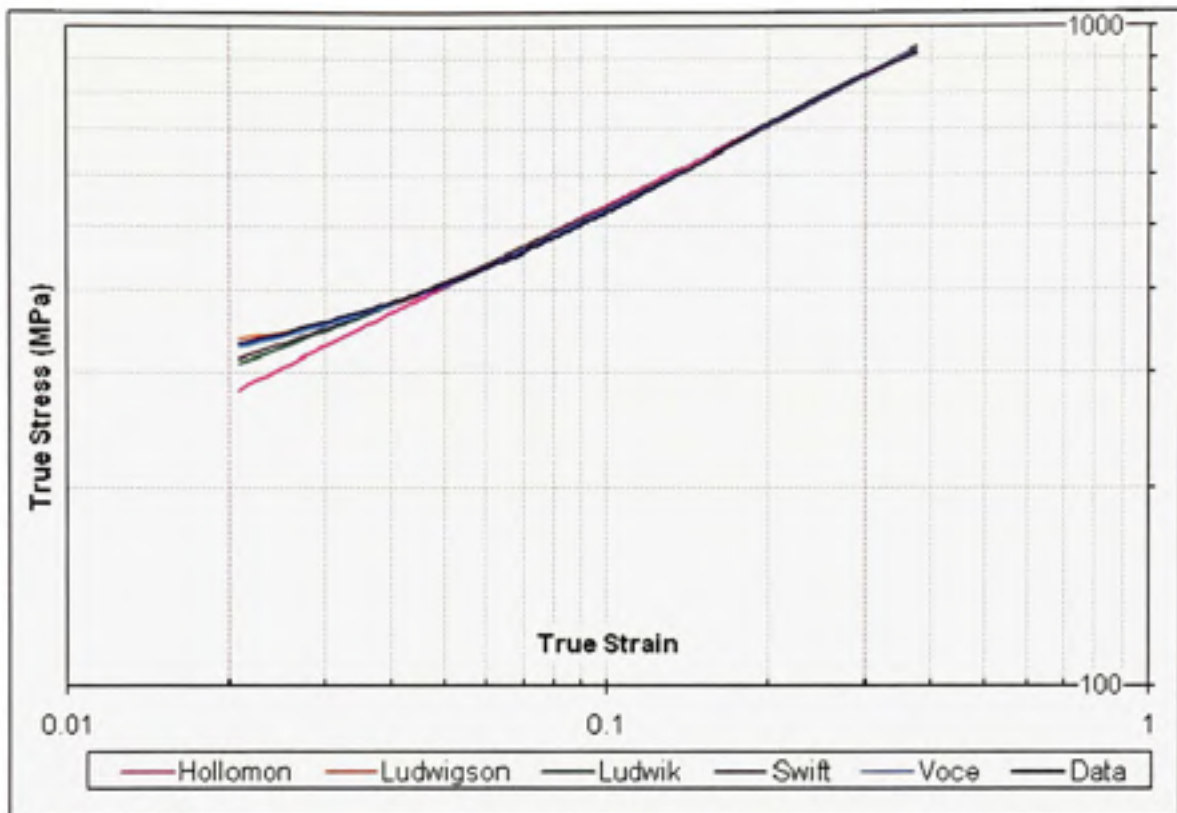


Figure 3.9 True stress-strain curve of SS 321 curved specimen – 0.9 mm thick fitted by calculated hardening equations in the logarithmic scale.

As for the flat samples, the hardening equations fit very well the data except at the beginning of the plastic strain range. The coefficients of the best fitted equations for the curved specimens are presented in Table 3.6. The calculated coefficients allow the extrapolation of the stress-strain curves of the curved specimens up to 100% deformation as presented in Figure 3.10.

Table 3.6 Best fitted coefficients of the tested hardening equations
SS321 curved specimens – 0.9 mm thick

| 0.9 curved | Hollomon $\sigma = K \epsilon_p^n$ | Ludwigson $\sigma = K \epsilon_p^n + \exp(K_1 + n_1 \epsilon_p)$ | Ludwik $\sigma = \sigma_0 + K \epsilon_p^n$ | Swift $\sigma = K (\epsilon_0 + \epsilon)^n$ | Voce $\sigma = \sigma_v - K_v \exp(n_v \epsilon_p)$ |
|------------|---------------------------------------|---|--|---|--|
| K | 1382.8 | 1415.8 | 1339.8 | 1442.0 | $K_v = 912.2$ |
| n | 0.4097 | 0.4269 | 0.5248 | 0.4634 | $n_v = -3.3857$ |
| | | $K_1 = 5.3368$ $n_1 = -55.14887$ | $\sigma_0 = 134.16$ | $\epsilon_0 = 0.0169$ | $\sigma_v = 1178.5$ |
| S/N | 100 | 21 | 53 | 43 | 4 |

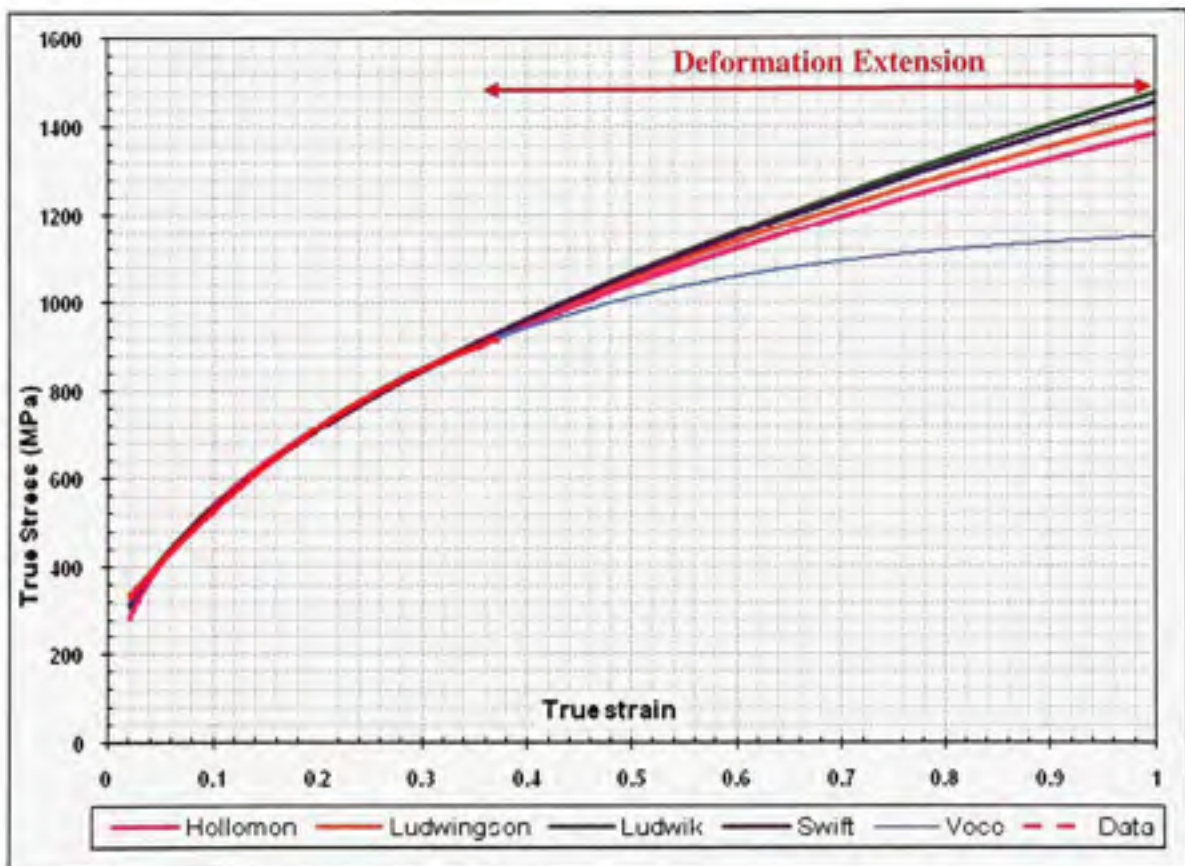


Figure 3.10 True stress-strain curves of SS 321 curved specimens – 0.9 mm thickness fitted by calculated hardening equations extended up to 100%.

The extrapolation conducted in the case of curved specimens shows more dispersion among the equations. The Voce equation goes apart whereas the other equations remain close to each other even if differences are visible.

3.2.3 Effect of the thickness on the hardening equations

In order to estimate the importance of the thickness, an identical procedure has been applied to 1.2 mm thickness curved specimens. To be able to compare both thicknesses, the average stress-strain curves of both geometries have been plotted in the same graph in Figure 3.11. The mechanical properties of the 1.2 mm thickness specimens have been sorted in Table 3.7.

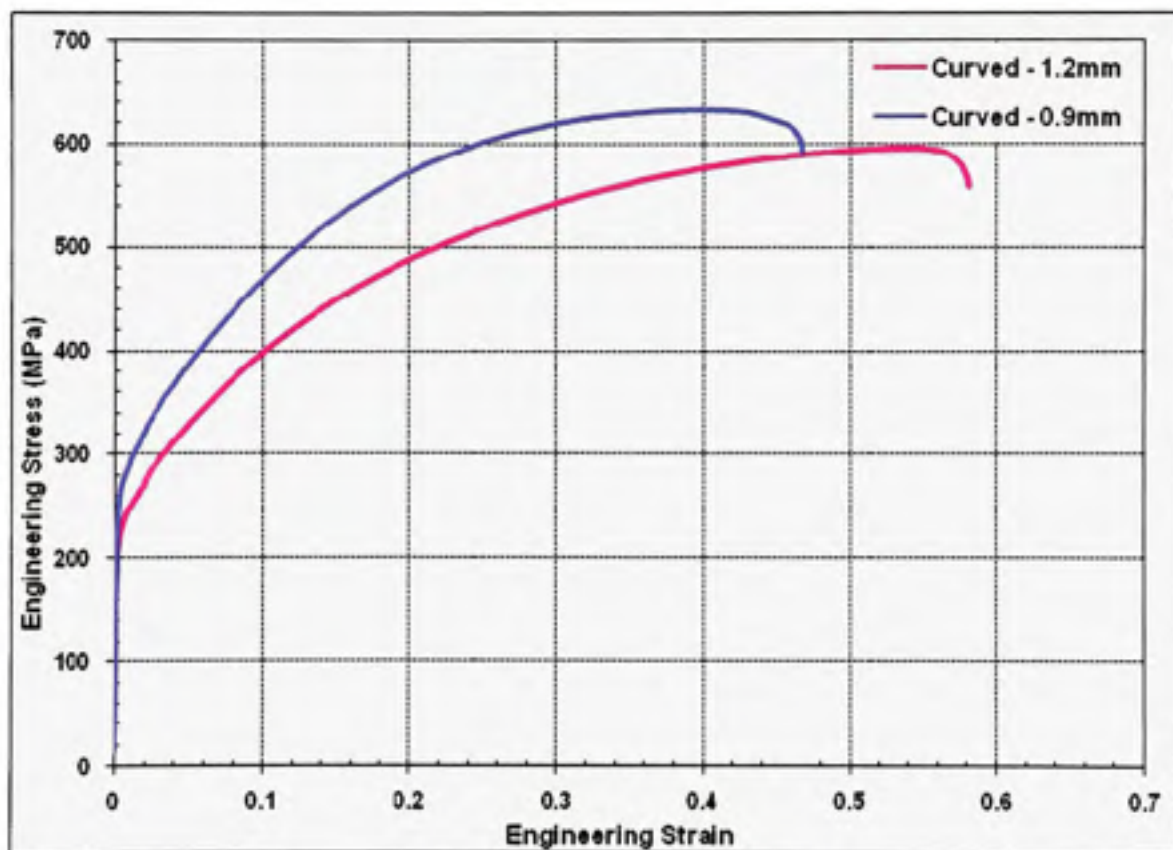


Figure 3.11 Comparison of engineering stress-strain curves of SS 321 curved samples 0.9 mm vs. 1.2mm thick.

Table 3.7 Mechanical properties of SS 321 curved samples - 1.2 mm thick

| 1.2 mm thick | YS (MPa) | UTS (MPa) | Necking strain | Breaking strain |
|------------------------|----------|-----------|----------------|-----------------|
| 321 - 0° | 224 | 585 | 0.529 | 0.590 |
| 321 - 90° | 218 | 587 | 0.535 | 0.583 |
| 321 - 180° | 229 | 617 | 0.528 | 0.586 |
| 321 - 270° | 219 | 595 | 0.545 | 0.593 |
| Average | 223 | 596 | 0.534 | 0.588 |
| Standard Deviation | 5,09 | 14,51 | 0.008 | 0.004 |
| 0.9 mm (comparison) | 266 | 633 | 0.404 | 0.473 |

The thickness of the tube has an important impact on the stress-strain curve, particularly on the mechanical properties. Indeed, the curves seem to follow the same trend but divergences appear at the yield point and increase with the deformation. The YS of the 0.9 mm specimen is 19% higher than the 1.2 mm one whereas the necking strain decreases by 24%. These differences could be explained by the process of tubes fabrication if those had been rolled. In this case, they are extruded. Probably, the extrusion process which requires plastic deformation of the metal has a different impact depending on the die (thin or thick).

The influence of thickness has been also investigated on the hardening coefficients. The best fit hardening coefficients obtained have been compiled in Table 3.8.

Table 3.8 Best fit coefficients of the hardening equations for SS321 curved specimens - 1.2 mm thick

| 1.2 curved | Hollomon | Ludwigson | Ludwik | Swift | Voce |
|------------|------------------------------|--|---|--|---|
| | $\sigma = K \varepsilon_p^n$ | $\sigma = K \varepsilon_p^n + \exp(K_1 + n_1 \varepsilon_p)$ | $\sigma = \sigma_0 + K \varepsilon_p^n$ | $\sigma = K (\varepsilon_0 + \varepsilon)^n$ | $\sigma = \sigma_v - K_v \exp(n_v \varepsilon_p)$ |
| K | 1354.5 | 1440.3 | 1334.7 | 1449.0 | $K_v = 1354$ |
| n | 0.4793 | 0.5342 | 0.7072 | 0.6160 | $n_v = -1.5912$ |
| | | $K_1 = 4.9084$ $n_1 = -17.1100$ | $\sigma_0 = 186.14$ | $\varepsilon_0 = 0.0481$ | $\sigma_v = 1599.0$ |
| S/N | 174 | 1 | 6 | 3 | 2 |

Figures 3.12 and 3.13 show respectively the strength coefficient K and the strain-hardening coefficient n values obtained in each equation for the different thicknesses. They highlight the effect of the geometry on the hardening coefficients. The Voce equation is not presented because its hardening coefficients (K_V and n_V) do not represent the same material reality as the K and n values of the other equations.

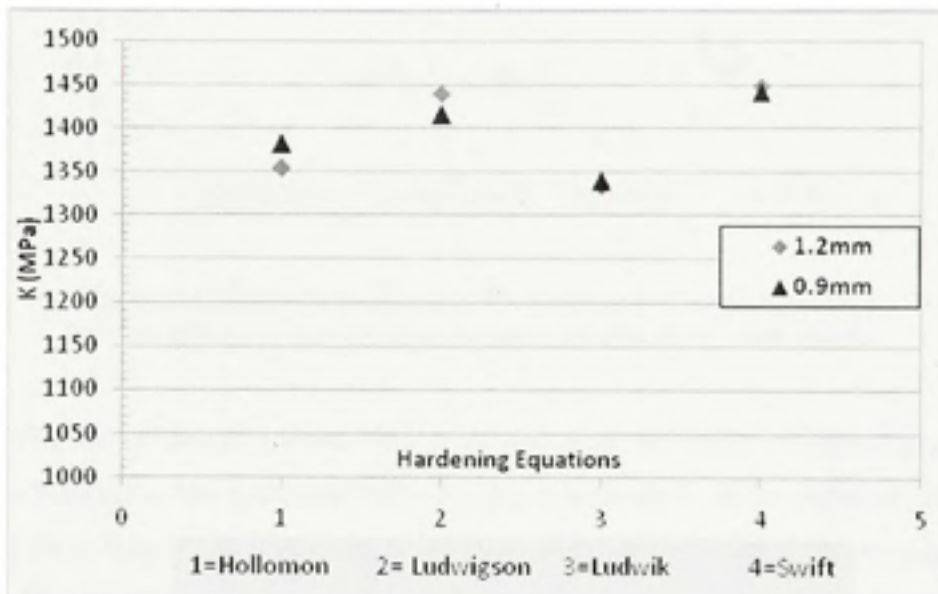


Figure 3.12 Best fit hardening coefficient K of each equation for two different curved specimens (0.9 mm & 1.2 mm thick).

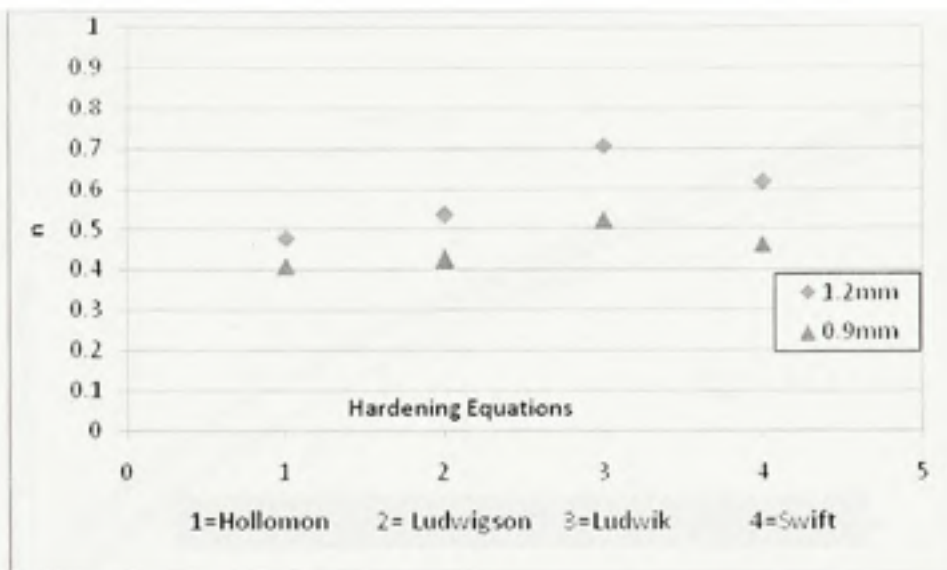


Figure 3.13 Best fit hardening coefficient n of each equation for two different curved specimens (0.9 mm & 1.2 mm thick).

The K coefficient is always around 1400 MPa and does not seem to depend much on the specimen's thickness. The difference between the calculated K of the different thickness is very small (less than 2%). More significant variations are noticed in the n -value. The n values for the 1.2 mm specimens are higher than for the 0.9 mm specimens. This means that larger degrees of strengthening are reached for the 1.2-thick specimens. It seems that a higher thickness leads to a delay in the necking.

The calculated flow curves extrapolated up to 100%, presented in Figure 3.14, show that for higher strains the 0.9 mm and 1.2 mm curves merge and no more significant differences are found.

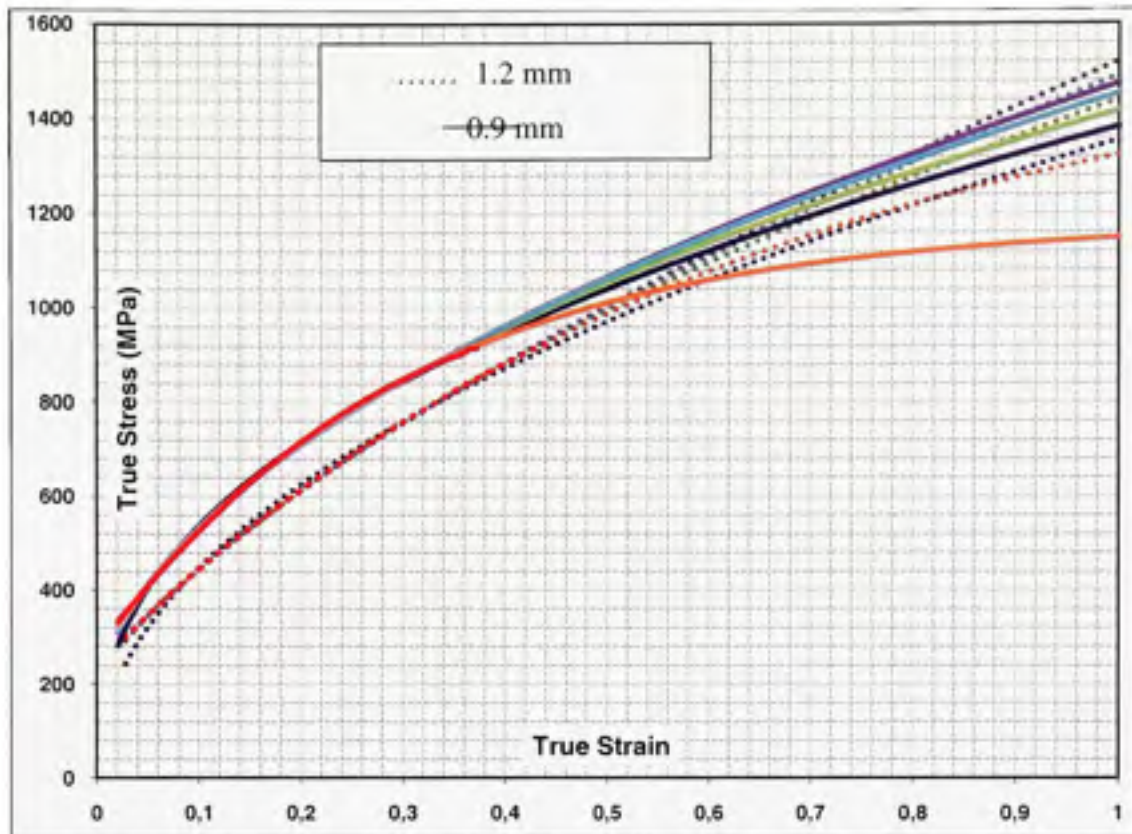


Figure 3.14 True stress-strain curves of two thicknesses SS 321 curved specimens (0.9 mm & 1.2 mm) fitted by calculated hardening equations extended up to 100%.

As demonstrated, the thickness of specimen for the same material has a considerable effect on the hardening equations. As a result, each material, in its particular shape, should be treated separately with its own material data during simulation process.

3.3 Biaxial stress-strain curves from tubes

Similarly to sheet metal samples, free expansion tests as presented in section 2.2.2 were done on the two tubes thicknesses (0.9 mm & 1.2 mm) to document the effect of biaxial strain and stress.

3.3.1 Stress – strain curves

Like the previous section, only the true stress-strain curves of 0.9 mm tubes based on free expansion tests data are shown here. The results obtained with the 1.2 mm tubes are detailed in ANNEX V. The raw data extracted from the FX test, coupled with the Aramis system, are the pressure versus the bulge height as presented in Figure 3.15. These are the result of two tests that gave very similar results.

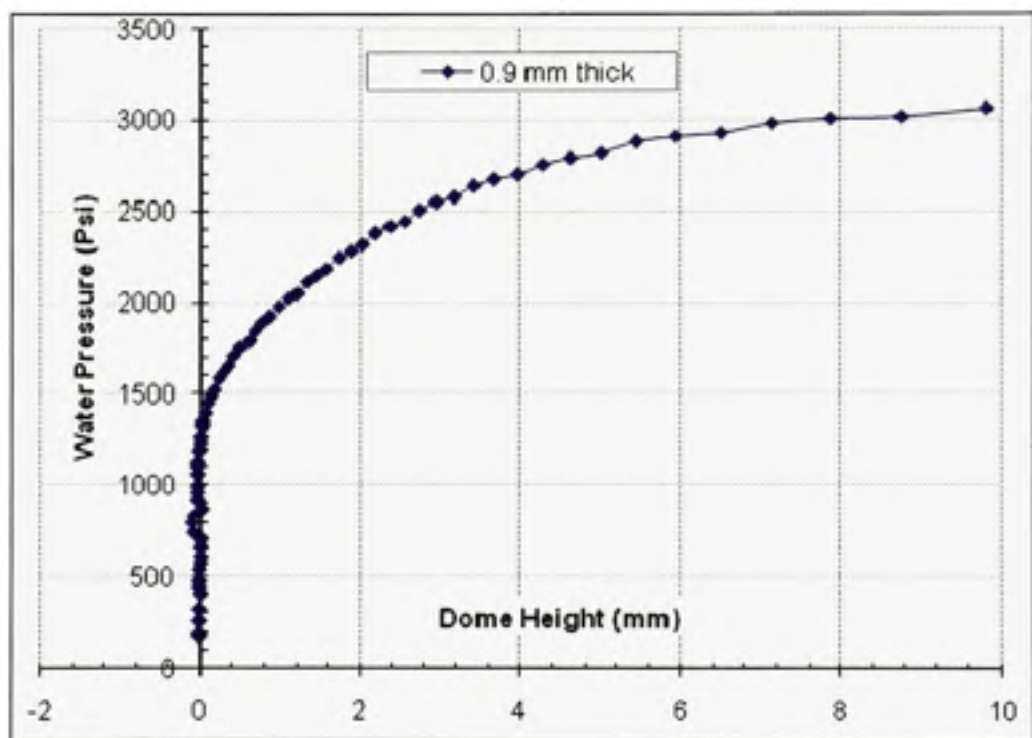


Figure 3.15 Water pressure vs. Expansion curve of SS 321 tubes from free expansion tests – 0.9 mm thick.

The calculations detailed in section 2.2.2.2 for the flow curve of tubes from FX tests use these data to extract the true stress-strain curve shown in Figure 3.16.

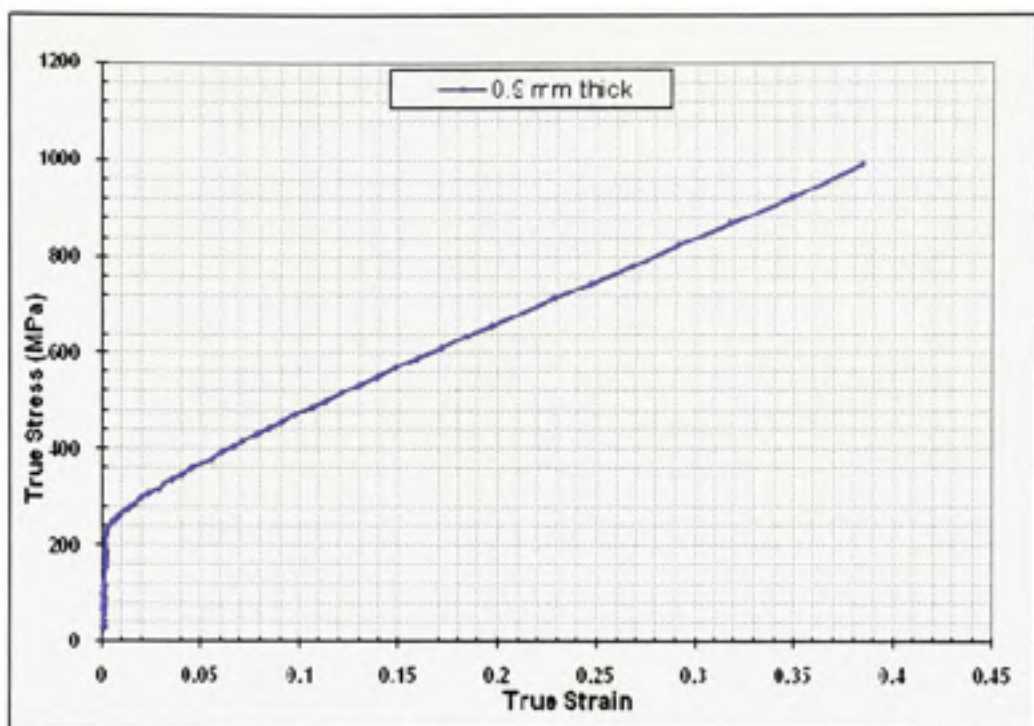


Figure 3.16 Calculated true stress-strain curves of SS 321 tubes from free expansion tests – 0.9 mm.

The stress-strain curve of tubes after calculations has a similar trend as a usual tensile test curve (Figure 3.17). The YS seems to appear at around 240 MPa. The true stress-strain representing the uniform plastic deformation zone, the necking seems to appear around 40%. However, because these curves are not obtained directly from experiments, it is questionable to use them to estimate the mechanical properties of the material in the biaxial loading.

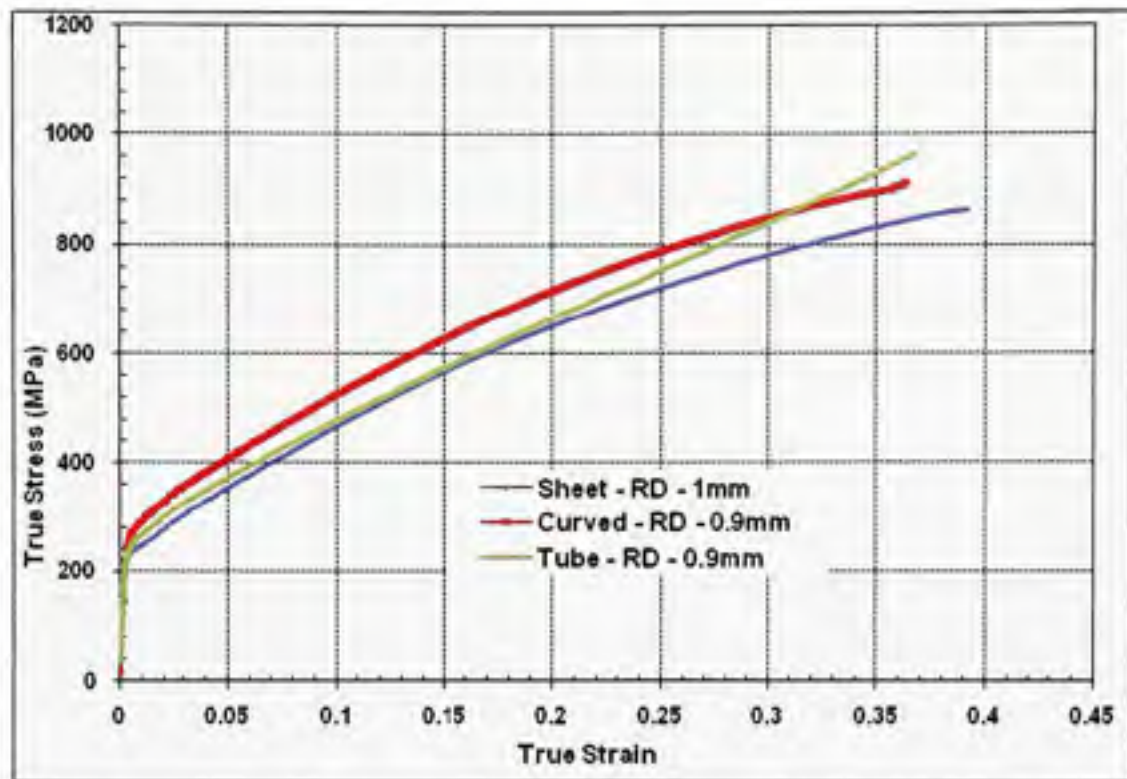


Figure 3.17 Comparison of true stress-strain curves of SS 321 – sheet (1 mm thick), curved (0.9 mm thick), and the calculated one for tube (0.9 mm thick).

The comparison between the true stress-strain curves of the different specimens shows many similarities but also some confusing divergences. Concerning the similarities, all the curves remain in the same window. That is to say the levels of stress and strain reached either in the uniaxial or in the biaxial state are very close. Nevertheless, the calculated curve for tubes has different hardening behavior. The biaxial curve is positioned between the uniaxial curves, closer to the sheet one. The tubes' curve reaches neither higher deformations than uniaxial curves nor very significant stresses. This observation goes completely against the common thought (Hwang, Lin and Altan, 2007; Koç, Aue-u-lan and Altan, 2001; Sokolowski and al., 2000) and are different to our expectations. Several hypotheses can explained those unexpected results. Our experimental procedure could be reviewed. In fact, the FX test goes very quickly particularly between the beginning of the expansion and the burst and it is almost impossible to capture the necking starting point, a key point in forming processes. In Also, a subsequent disadvantage is that the curves compared above do not stop at the same

moment. We can better take advantage of the optical image correlation system used to measure continuously the bulge height by increasing the frequency of the images record and thus improve the precision of the data measurements. Also, the method used to calculate the true stress-strain curves from FX tests exhibits some strong assumptions which could lead to an underestimation of the stress and strain reached. Finally, the material studied, SS 321 which is a very deformable one could be insensitive to the effect of the specimens' geometry in a biaxial state.

3.3.2 Hardening equations

The average stress-strain curve from 0.9 mm tubes has been fitted and the calculated curves which best fit the data are plotted in Figure 3.18. Also, the best fit coefficients of the hardening equations for 0.9 mm thick tubes as presented in Table 3.9.



Figure 3.18 True stress-strain curve of SS 321 tubes 0.9 mm thick fitted by calculated hardening equations in the logarithmic scale.

Table 3.9 Best fit coefficients of the tested hardening equations
SS321 tubes 0.9 mm thick

| 0.9 tube | Hollomon $\sigma = K \varepsilon^p$ | Ludwigson $\sigma = K \varepsilon^p + \exp(K_1 + n_1 \varepsilon^p)$ | Ludwik $\sigma = \sigma_0 + K \varepsilon^p$ | Swift $\sigma = K (\varepsilon_0 + \varepsilon)^n$ | Voce $\sigma = \sigma_v - K_v \exp(n_v \varepsilon^p)$ |
|----------|--|---|---|---|---|
| K | 1342.1 | 1986.8 | 1665.8 | 1745.9 | $K_v = 2010.0$ |
| n | 0.4198 | 0.7855 | 0.8422 | 0.7352 | $n_v = -1.1529$ |
| | | $K_1=5.4136$ | $n_1=-3.8336$ | $\sigma_0=238.4$ | $\varepsilon_0=0.0713$ |
| S/N | 1268 | 2 | 6 | 14 | 27 |

The calculated stress-strain curves are able to fit correctly the experimental data with the exception of the Hollomon equation. These results are different from what has been notified in the tensile tests of curved specimens based on the S/N criteria. This contradiction can be explained by two hypotheses. Either, the uniaxial tensile test does not reflect the deformation undergone during a free expansion test and the two sets of data cannot be compared (the hardening curves obtained in both cases are independent); or, the stress-strain curves calculated based on free expansion tests are not yet representative of the reality. This statement has to be considered since the program used is not yet in its final state.

3.3.3 Effect of the thickness

In order to compare the effect of the tube thickness on the loading behavior, the best fit hardening coefficients for the 1.2 mm thickness tubes are also presented in Table 3.10. The extended stress-strain curves obtained with the best fit coefficients for both thicknesses are presented in Figure 3.19.

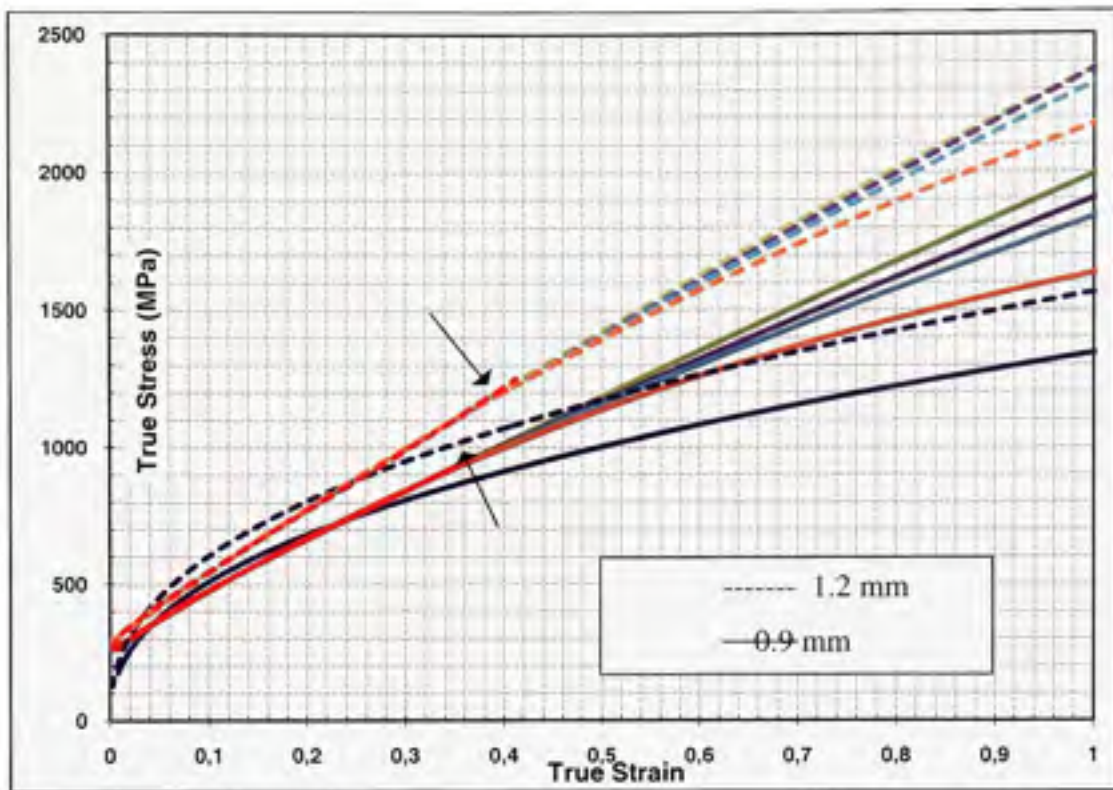


**Figure 3.19 Calculated true stress-strain curves of two thicknesses SS 321 tubes (0.9 mm & 1.2 mm) fitted by calculated hardening equations extended up to 100%.
The arrows represent the end of the experimental data.**

**Table 3.10 Best fit coefficients of the tested hardening equations –
SS321 tubes 1.2 mm thick**

| 1.2 tube | Hollomon $\sigma = K \varepsilon_p^n$ | Ludwigson $\sigma = K \varepsilon_p^n + \exp[K_1 + n_1 \varepsilon_p]$ | Ludwik $\sigma = \sigma_0 + K \varepsilon_p^n$ | Swift $\sigma = K (\varepsilon_0 + \varepsilon)^n$ | Voce $\sigma = \sigma_v - K_v \exp(n_v \varepsilon_p)$ |
|----------|--|---|---|---|---|
| K | 1562.9 | 2375.9 | 2099.1 | 2179.6 | $K_v = 3732.4$ |
| n | 0.4128 | 0.7462 | 0.8894 | 0.8124 | $n_v = -0.7031$ |
| | | $K_1 = 5.5282$ $n_1 = -7.4394$ | $\sigma_0 = 275.11$ | $\varepsilon_0 = 0.0812$ | $\sigma_v = 4020.5$ |
| S/N | 4362 | 14 | 55 | 83 | 108 |

For both thicknesses, the curves follow the same trend. However, conversely to the results for curved specimen, the 1.2 mm thick tubes come to higher stresses than the 0.9 mm ones. The main coefficients K and n are higher in the case of the thin tube than the thick tube.

In Figure 3.19, the hardening behavior was extrapolated to $\varepsilon = 1$. Except the Hollomon curves (blue curves), which remains in a lower range of stress, compared to those in the curved specimens, the other equations reach very large stresses. The level of stress reached after extension is very close to what was expected. At significant levels of deformation, the stress required to deform in a biaxial state of strain seems higher compared to the uniaxial state (Bortot, Ceretti and Giardini, 2008). However, some questionings remain concerning the validity of the hardening coefficients calculated based on the stress-strain curves of tubes. In fact, for both thicknesses, the n -value calculated is between 0.53 and 0.84 in the considered hardening equations which is superior to the typical n -value of metals and alloys known as been between 0.1 and 0.5.

3.4 Synthesis

In this chapter, the effect of the specimens' shape has been discussed. In the case of flat specimens, limited anisotropy have been reported on the mechanical properties, hardening coefficients as well as crystalline texture. The thickness impact has been analyzed on curved tensile specimens and tubes. On the contrary, a significant effect of the tube thickness on the stress-strain curves and the hardening coefficients were found. The estimation of the true stress-strain curves based on the FX tests showed unexpected results. The biaxial test does not seem to lead to higher level of strain. Also, the flow curves do not follow the similar hardening behavior. Before confirming those results, the experimental procedure followed as well as the calculations program have to be reexamine and improve if necessary.

This work was focused on developing a method to extract systematically all the hardening coefficients from several hardening equations. The extrapolated stress-strain curves up to 100% deformation for all geometrical configurations are compared respectively in Figures Figure 3.20 and Figure 3.21. Also, Table 3.11 summarizes the different hardening equations in function of the geometry, the thickness and the yield strength.

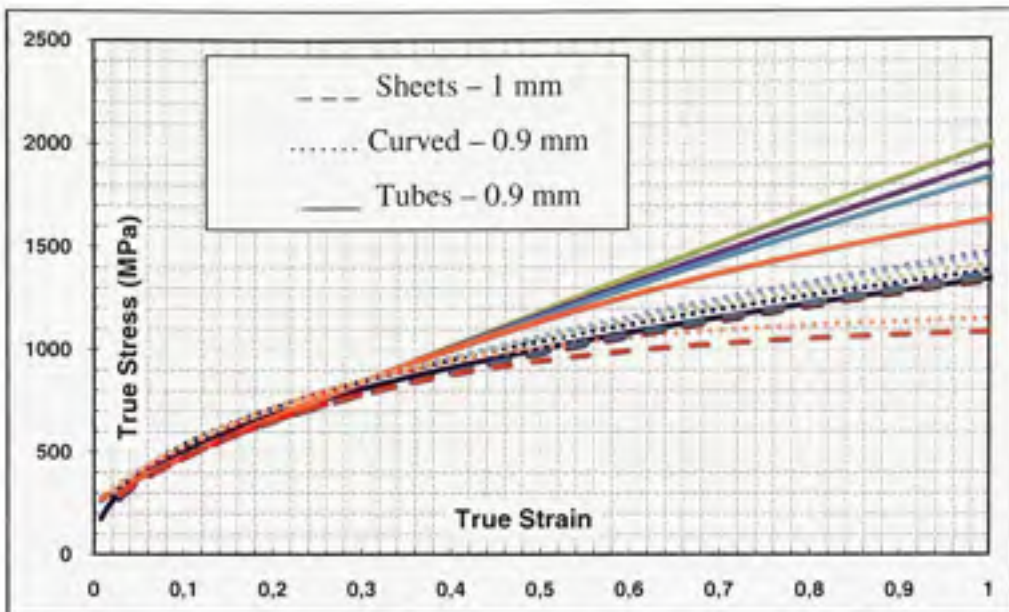


Figure 3.20 Stress-strain curves of SS 321 sheets (1mm thick), curved and tubes (0.9 mm) fitted by calculated hardening equations extended up to 100%.

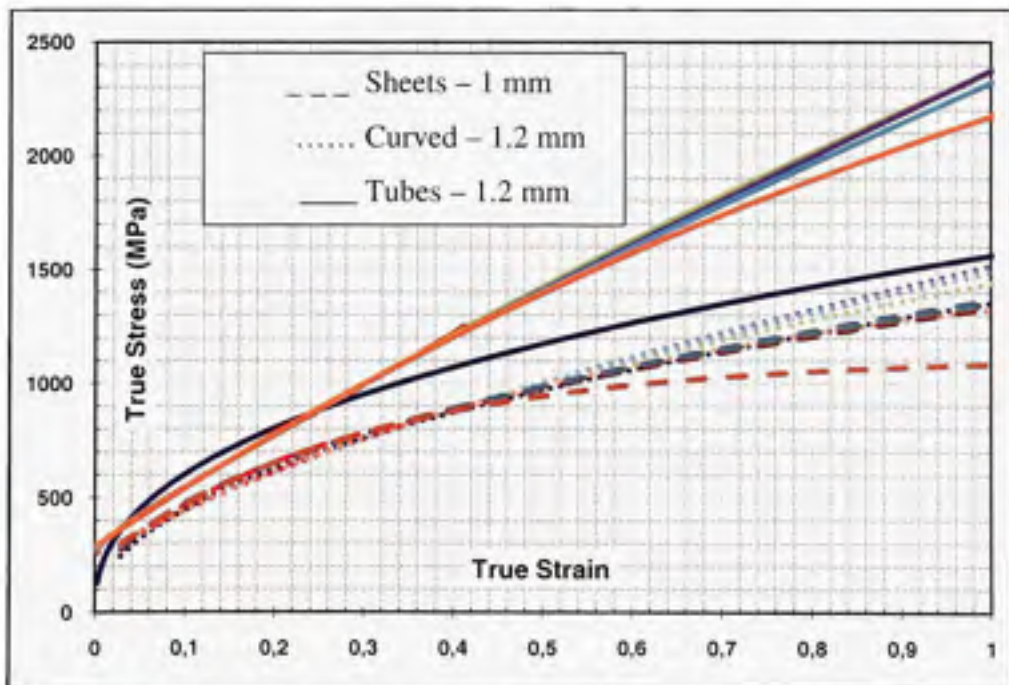


Figure 3.21 Stress-strain curves of SS 321 sheets (1 mm), curved and tubes (1.2 mm) fitted by calculated hardening equations extended up to 100%.

Table 3.11 Summary of hardening coefficients for different equations of SS 321 in various geometries

| SS 321 | VS | Hollomon $\sigma = K \epsilon_p^n$ | | | Ludwigin $\sigma = K \epsilon_p^n + \exp(K_1 + K_2 \epsilon_p^n)$ | | | Ludwik $\sigma = \sigma_0 + K \epsilon_p^n$ | | | Swift $\sigma = K (\epsilon_0 + \epsilon)^n$ | | | Voce $\sigma = \sigma_v + K_v \exp(n_v \epsilon_v)$ | | | |
|--------|-----|---------------------------------------|--------|--------|--|----------------|----------------|--|--------|------------|---|--------|--------------|--|----------------|------------|--------|
| | | K | n | K | n | K ₁ | n ₁ | K | n | σ_0 | K | n | ϵ_0 | K _v | n _v | σ_v | |
| SHEET | RD | 230 | 1333.7 | 0.446 | 1348.1 | 0.4542 | 5.7395 | -73.8085 | 1312.8 | 0.49 | 51.98 | 1356.9 | 0.47 | 0.0077 | 900.4 | -3.2968 | 1117.9 |
| | 45D | 229 | 1255.2 | 0.4432 | 1274 | 0.4555 | 5.3838 | -51.5864 | 1214.6 | 0.5291 | 92.53 | 1287.8 | 0.4857 | 0.0153 | 918.7 | -2.723 | 1145.4 |
| | TD | 241 | 1301.6 | 0.4509 | 1310.4 | 0.4692 | 5.1262 | -38.1935 | 1233.4 | 0.5783 | 129.44 | 1349.6 | 0.5146 | 0.0232 | 1014 | -2.4022 | 1151.9 |
| | 0.9 | 266 | 1382.8 | 0.4097 | 1415.8 | 0.4259 | 5.3368 | -55.14887 | 1339.8 | 0.5248 | 134.16 | 1442 | 0.4634 | 0.0169 | 912.2 | -3.3857 | 1178.5 |
| CURVE | 1.2 | 223 | 1154.5 | 0.4793 | 1440.3 | 0.5342 | 4.9084 | -17.1100 | 1334.7 | 0.7072 | 186.14 | 1449.0 | 0.6160 | 0.0481 | 1354.0 | -1.5912 | 1599.0 |
| | 0.9 | | 1342.1 | 0.4198 | 1986.8 | 0.7855 | 5.4136 | -3.8336 | 1665.8 | 0.8422 | 238.4 | 1745.9 | 0.7352 | 0.0713 | 2010 | -1.1529 | 2266.5 |
| | 1.2 | | 1562.9 | 0.4128 | 2375.9 | 0.7462 | 5.5282 | -7.4394 | 2099.1 | 0.8894 | 275.11 | 2179.6 | 0.8124 | 0.0812 | 3732.4 | -0.7031 | 4020.5 |

CHAPTER 4

HEAT TREATMENT IMPACT ON THE MATERIAL CONSTITUTIVE LAWS (SS 321 / SS 17-4PH / INC 718)

The purpose of this chapter is to enforce the characterization method put in place in the previous section to various aerospace alloys. Moreover, the metallurgical part is underlined as the impact of different heat treatments on the material mechanical properties and hardening behavior is studied. The uniaxial tensile test has been chosen to conduct this campaign because it is the easiest mechanical test. Also, only flattened specimens in the RD direction have been used for cost and availability reasons. The heat treatments section has been performed at PWC. In addition to the evaluation of the mechanical properties of the materials in the different metallurgical states, the hardening coefficients have been extracted. Beyond the mathematical fitting of the hardening equations, it has been important to validate if they have a physical sense, in other words, if the coefficients calculated reflect the mechanical reality. To reach that goal, the YS has been calculated for each equation based on the assumption that it corresponds to the stress when the plastic strain reaches the offset point ($\epsilon_p = 0.002$). The YS calculations, just give another criteria with which we can classify the equations.

4.1 Stainless Steel 321

As SS 321 has been widely studied in the previous chapter in its as-received state of strain (A-R), only the results concerning an alternative heat treated state are detailed in this section. For the comparisons, the reader will be send back to the appropriate table or figure.

4.1.1 Applied Heat treatment

SS 321 is an alloy hardened only by cold working. A **Stress Relieve** heat treatment (SR) is generally used to recover the material and increase the ductility (Chandler, 1996, p. 753). The

SR treatment has been performed on the as-received specimens prior to deformation. The heat treatment schematic is presented in Figure 4.1 and consists of one hour holding time at 982°C and a rapid cooling at minimum 19°C/min.

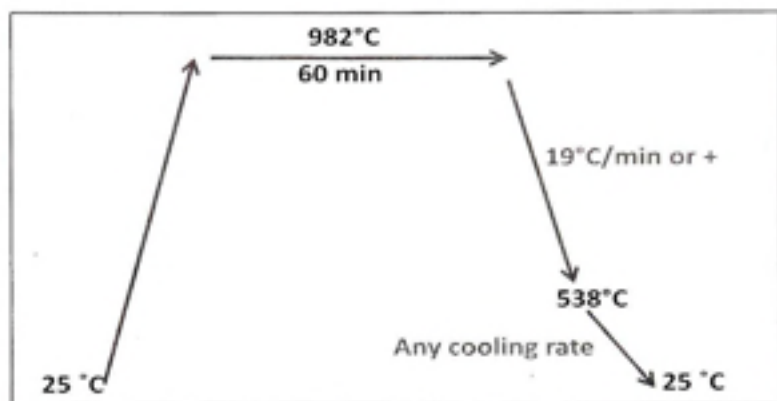


Figure 4.1 SR performed on the SS 321 specimens.

4.1.2 Stress-strain curves

For comparison with the A-R state, two SR specimens were tested. The average curves of two uniaxial tensile tests are plotted in Figure 4.2.

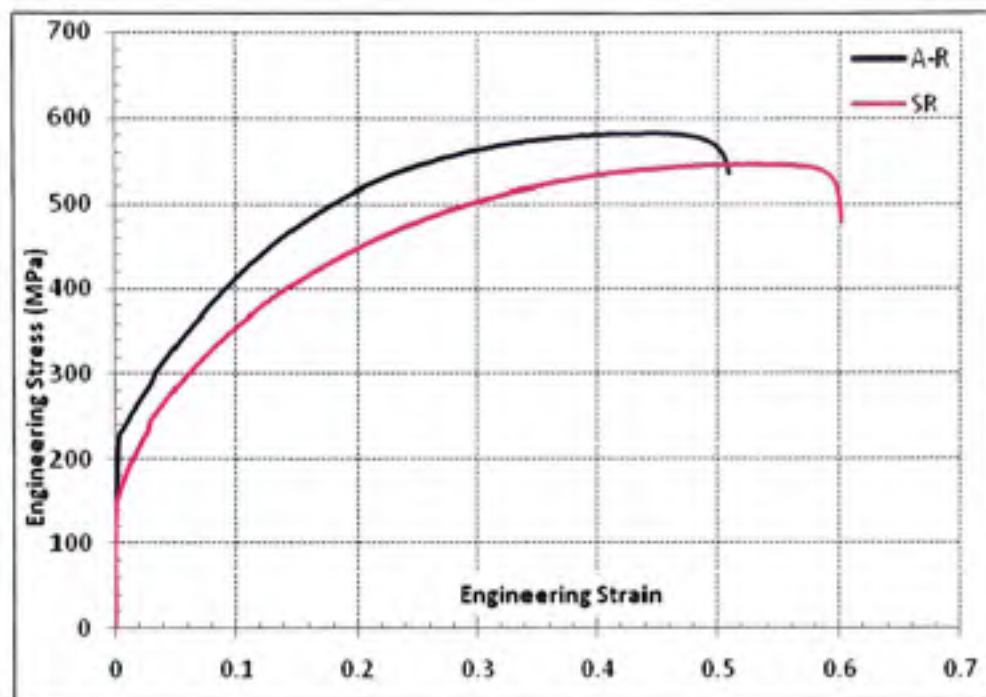


Figure 4.2 Engineering stress-strain curves of SS 321 flat samples (1 mm thickness) in As-Received state vs. Stress Relieve state.

The stress-strain curves have the same shape, however, the YS is lower after heat treatment whereas the breaking strain increases. To compare into details, the mechanical properties of both specimens have been inserted in Table 4.1. the Young modulus have not been evaluated because of a lack of data points obtained in the elastic part as explained p. 62.

Table 4.1 Mechanical properties of SS 321 flatted samples in A-R and SR states

| SS 321 | E (GPa) | YS (MPa) | UTS (MPa) | Necking strain | Breaking strain |
|------------|---------|----------|-----------|----------------|-----------------|
| A-R | 183 | 230 | 592 | 0.453 | 0.515 |
| SR | - | 156 | 547 | 0.531 | 0.603 |

The properties obtained in the A-R state are closed to the ones given by the literature (p. 42). Significant variations are observed between these two curves. After SR, the material gains in ductility. The A-R material is not in its softest condition. So, the application of this heat

treatment systematically before starting any deformation will be envisaged in order to always start the THF process in a the softest material condition.

4.1.3 Hardening equations

The true stress-strain curves of both tests have been plotted in the logarithmic scale as shown in Figure 4.3 in order to extract their hardening coefficients. The experimental true stress-strain curve and its best fitted curves have been plotted in Figure 4.4.

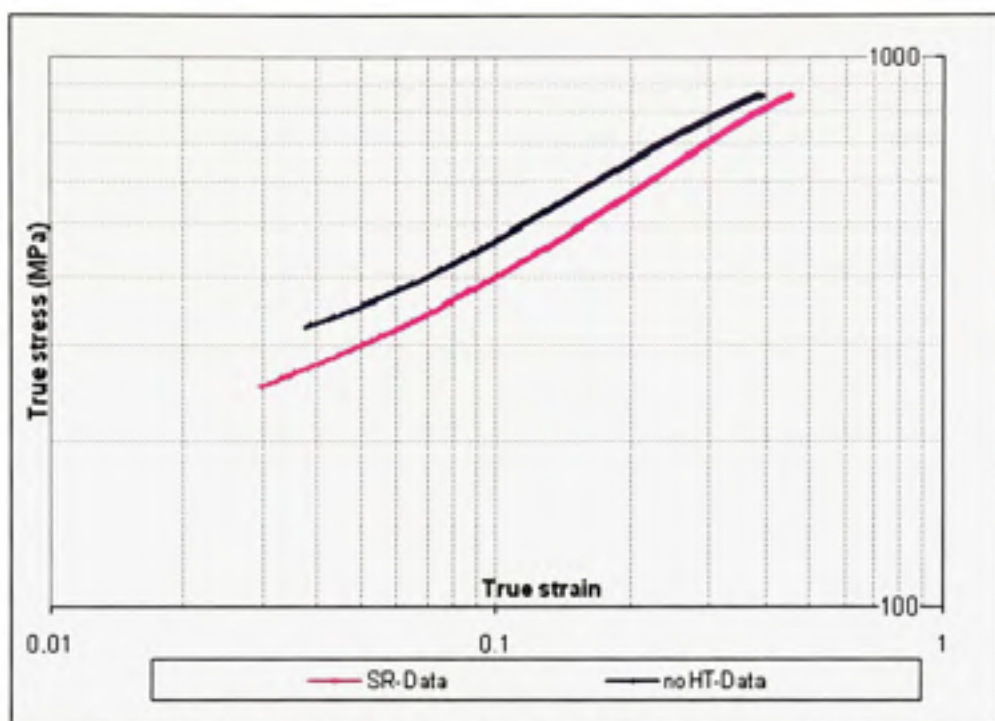


Figure 4.3 Comparison of true stress-strain curves of both A-R and SR specimens in logarithmic scale.

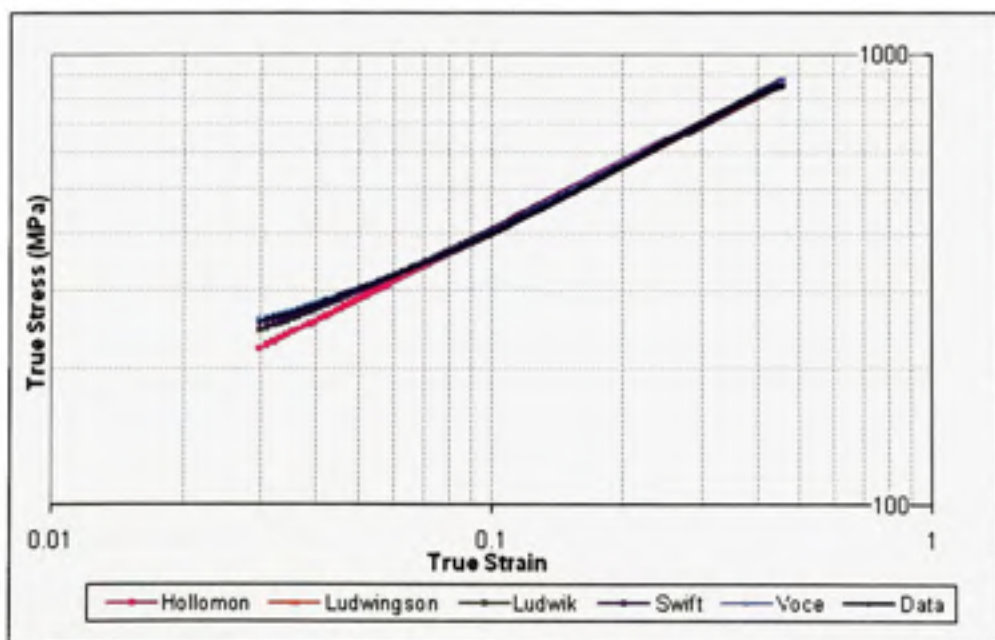


Figure 4.4 True stress-strain curves of SS 321 SR heat treated specimen fitted by calculated hardening equations in the logarithmic scale.

The hardening equations all fit well the data. Some tiny differences are observed at the beginning, particularly for the Hollomon curve but around 7% plastic deformation, all the equations converge to a relative straight line. The same conclusions had been done on the fitting of the A-R true stress-strain curve in section 3.1.2. The best fit coefficients of the studied hardening equations of the SR specimen are presented in Table 4.2 (for comparison, Table 3.2 presented the same data for the A-R curves).

Table 4.2 Best fit coefficients of the tested hardening equations -
SS 321 heat treated specimens (SR)

| SR | Hollomon $\sigma = K \varepsilon_p^n$ | Ludwigson $\sigma = K \varepsilon_p^n + \exp(K_1 + n_1 \varepsilon_p)$ | Ludwik $\sigma = \sigma_0 + K \varepsilon_p^n$ | Swift $\sigma = K (\varepsilon_0 + \varepsilon)^n$ | Voce $\sigma = \sigma_v - K_v \exp(n_v \varepsilon_p)$ |
|-----|--|---|---|---|---|
| K | 1283.8 | 1307.9 | 1256.1 | 1320.1 | $K_v = 1076.8$ |
| n | 0.5030 | 0.5193 | 0.6004 | 0.5563 | $n_v = -2.1552$ |
| | | $K_1 = 4.7817$ $n_1 = -32.7513$ | $\sigma_0 = 88.64$ | $\varepsilon_0 = 0.0186$ | $\sigma_v = 1266.6$ |
| S/N | 50 | 11 | 22 | 18 | 3 |

The YS has been evaluated by each equation using the best fit coefficients and the results are presented in Table 4.3.

Table 4.3 Calculated YS based on the best fit parameters of tested hardening equations – SS 321 in A-R and SR states

| YS | Hollomon $YS_H = 0$ | Ludwigson $YS_L = \exp(K_1)$ | Ludwik $YS_LK = \sigma_0$ | Swift $YS_S = K (\varepsilon_0)^n$ | Voce $YS_V = \sigma_v - K_v$ | Experimental |
|-----|------------------------|---------------------------------|------------------------------|---------------------------------------|---------------------------------|--------------|
| A-R | 83 | 348 | 114 | 154 | 223 | 240 |
| SR | 56 | 164 | 119 | 152 | 194 | - |

In order to understand the influence of the heat treatment on the hardening behavior, the two important hardening coefficients (K & n) have been compared at each equation for both states in Figure 4.5 and Figure 4.6.

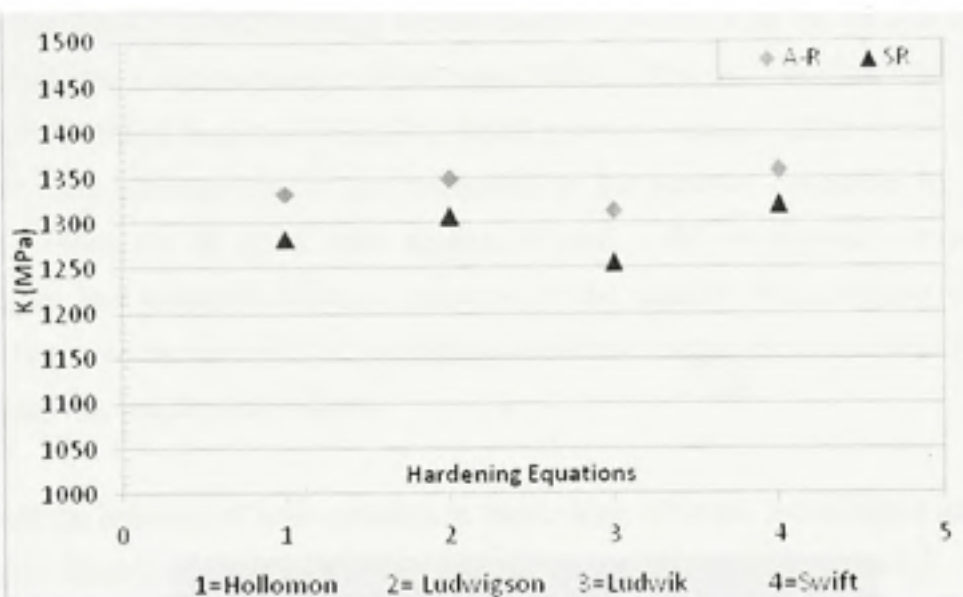


Figure 4.5 Best fit strength coefficient K of each equation for as-received and heat treated specimens.

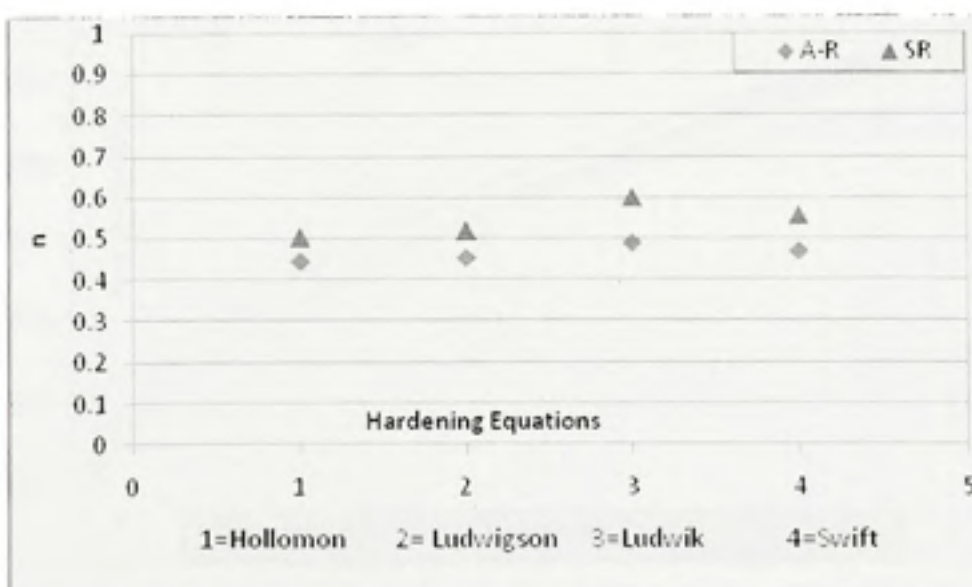
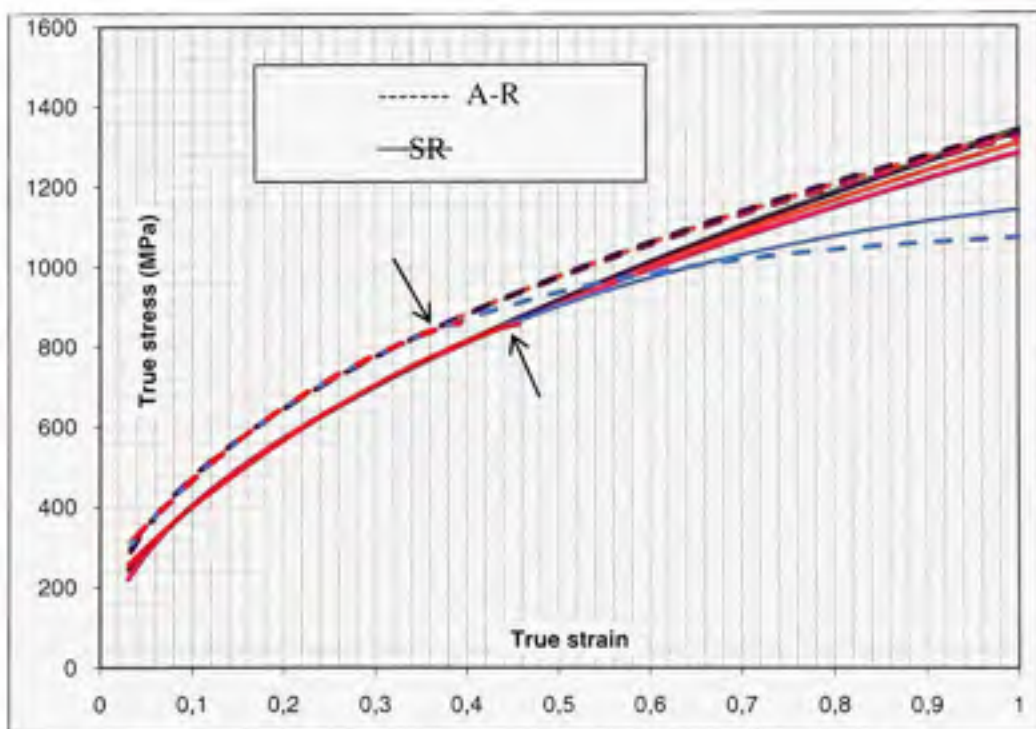


Figure 4.6 Best fit hardening coefficient n of each equation for as-received and heat treated specimens.

The Voce equation is not plotted because its hardening coefficients (K_V & n_V) do not represent the same material concept as in the other equations. Otherwise, the strength coefficients differences between both curves are regular and seem almost not to depend on

the type of equation. The decrease in K varies between 2 and 4% after the SR heat treatment. Contrastingly, the n values increase by the same amount. That is to say, for each equation, the SR heat treatment leads to a small but almost constant increase of the strain hardening coefficient most probably due to the restoration of the material conducted by the heat treatment. Indeed, the SR as its name suggests is used to relieve previous stresses in the material; hence, an increase of strain hardening is observed and so does the strain for which necking happens, and thus the ductility.

To evaluate the behavior of both materials at higher level of strain, extrapolated true stress-strain curves fitted by the best hardening equations have been plotted in Figure 4.7.



**Figure 4.7 True stress-strain curves of two SS 321 sheets (A-R & SR) fitted by calculated hardening equations extended up to 100%.
The arrows represent the end of experimental data.**

At very high levels of strain, the curves start to coincide and no more differences are noticed between A-R and SR.

4.2 Stainless Steel 17-4 PH

As for SS 321, uniaxial tensile tests have been performed on RD sheets for 17-4 PH. This part develops the effect of heat treatments on the mechanical properties and hardening behavior of SS 17-4 PH.

4.2.1 Heat treatments

The specificity of SS 17-4PH is its sensitivity to heat treatments. In fact, its most important strengthening mechanism is by precipitation. Thus, two different heat treatments have been tested and compared to the as received (A-R) condition. The A-R condition, according to the literature consists on the solution treating heat treatment followed by an oil quenching or an air cooling to below 33°C. It is known as the hardest state of SS 17-4 PH (Wu, 2003).

The first one, presented in Figure 4.8 is an **Annealing Overage** heat treatment (AO) and is supposed to generate the softest condition of the heat treatment recipes available at PWC.

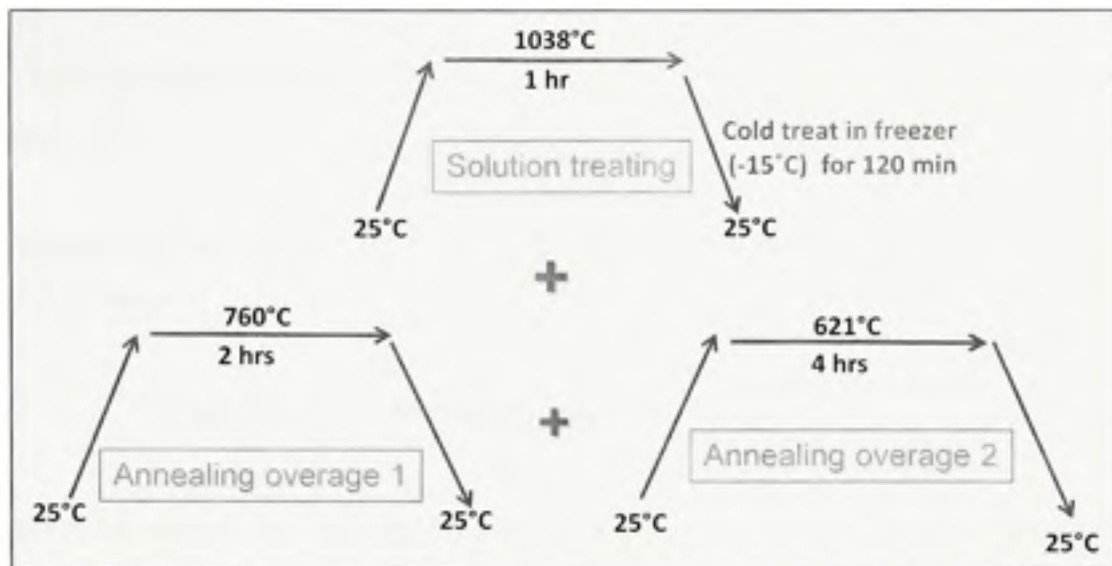


Figure 4.8 Annealing Overage schedule performed on SS 17-4 PH specimens.

The second heat treatment performed is called **Precipitation Hardening (PH)** and leads to an intermediate hardening state of the material compare to the AO state which is soft and the A-R state (condition A) which is very hard. It is considered as a good alternative to Condition A in terms of forming as it is softer (ASM International., 2001). The schedule is presented in Figure 4.9.

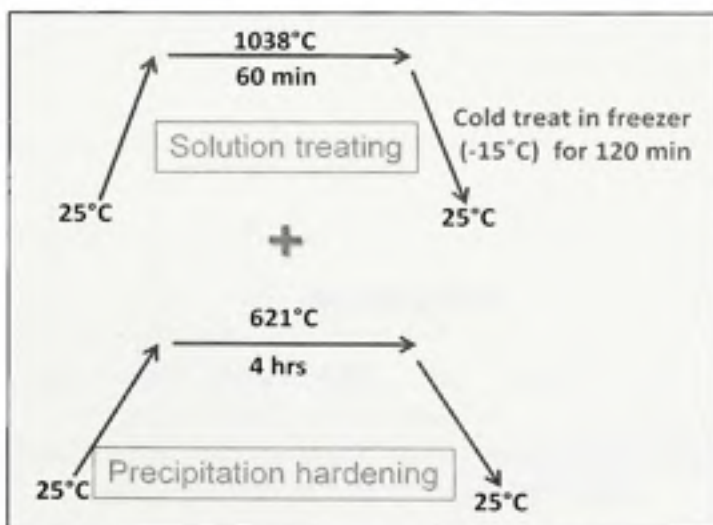


Figure 4.9 Precipitation Hardening schedule performed on SS 17-4 PH specimens.

The PH heat treatment performed is closed to the H1150 heat treatment briefly introduces in section 1.3.2.2.

Hardness measurements are used to track precisely the material softening between each heat treatment steps.

4.2.2 Stress-strain curves comparison

Figure 4.10 presents the engineering stress-strain curves of SS 17-4 PH specimens after various heat treatments schedules presented above.

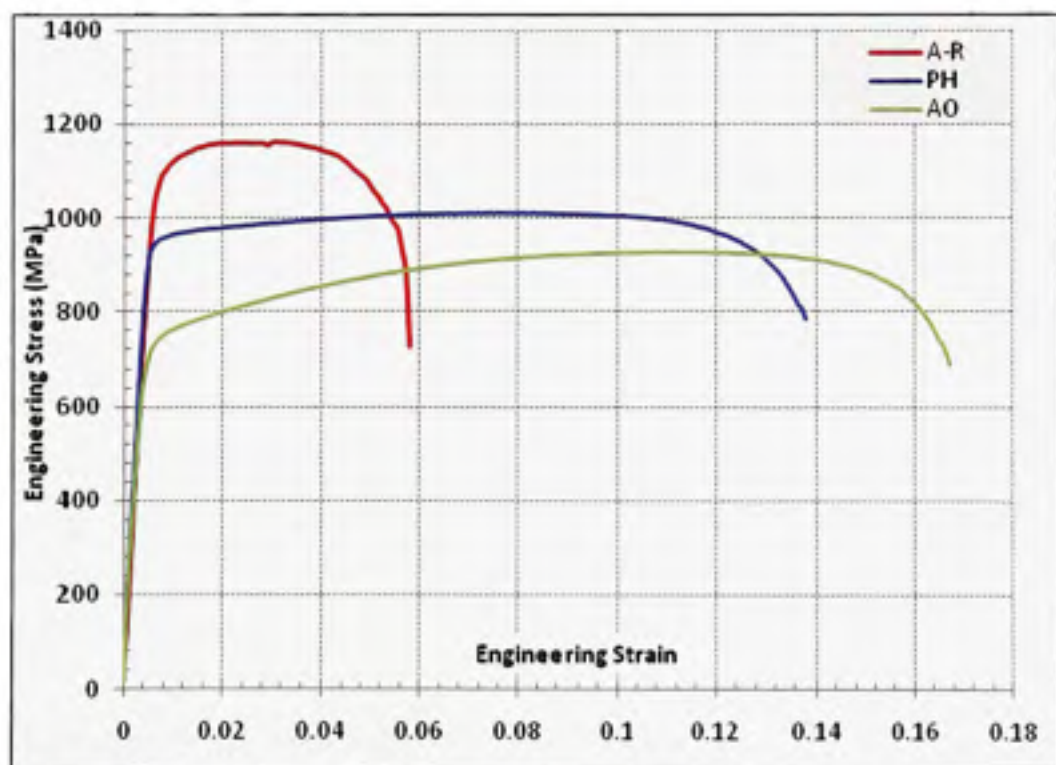


Figure 4.10 Engineering stress-strain curves of SS 17-4 PH flat samples in A-R, PH and AO states.

Any heat treatment applied to this alloy influences the mechanical properties. The A-R material presents a very high strength combined with a limited plastic deformation. The AO

state gives the most ductile behavior with a certain decrease in strength but a huge gain in ductility. Finally the PH heat treatment leads the material to an intermediate behavior between the previous ones. The decrease in strength is not significant whereas the increase in strain remains non negligible compared to the A-R material. Table 4.4 summarizes the mechanical properties of SS 17-4 PH in the three states.

Table 4.4 Mechanical properties of SS 17-4 PH flattened samples in A-R, PH and AO states

| SS 17-4 PH | E (GPa) | YS (MPa) | UTS (MPa) | Necking strain | Breaking strain |
|------------|---------|----------|-----------|----------------|-----------------|
| A-R | 199 | 1087 | 1168 | 0.028 | 0.064 |
| AO | 181 | 727 | 926 | 0.112 | 0.169 |
| PH | 191 | 951 | 1013 | 0.077 | 0.142 |

When the mechanical properties are compared to those given by the literature (p.44), the initial state of the specimen is confirmed as Condition A whereas the PH heat treatment can be considered as an alternative to the H1150. In addition, the young modulus does not change significantly with the heat treatment as in Table 1.4. After the AO heat treatment, the YS as well as the UTS dropped by 33% and 20% respectively. This decrease is quite interesting as it comes along with a greater potential for plastic deformation. In fact, the gain in ductility can be appreciated as the necking strain increase by 300%. This alloy presents the particularity to keep deforming a lot after necking before rupture. The non uniform plastic strain zone is useless in our case as necking apparition becomes the appropriate property to evaluate the ductility. Thus, comparing A-R and AO specimens, the AO heat treatment allows trebling the necking strain.

The PH treatment brings an important increase of the ductility with less loss of strength. This intermediate heat treatment has been tested as it may have an effect on the necking. The YS drop, between the A-R and PH specimens, is about 12.5% whereas the UTS difference is less than 5% and, the necking strain reaches 175% the A-R necking strain. Finally, the PH heat treatment is turned out to be a very interesting compromise in terms of strength and ductility.

The gain in YS is important, about 23% and the loss in the necking apparition delay is low, 30%. Nevertheless, the hardening behavior of both heat treated specimens does not seem to follow the same trend. So, both states have to be studied independently in terms of hardening behavior.

4.2.3 Hardening equations

In order to study the hardening equations of the several metallurgical states of SS 17-4 PH, the true stress-strain curves of the designated specimens in the uniform plastic strain range have been plotted in a logarithmic scale. Then, the best fit hardening coefficients have been extracted and the results obtained are presented in this section.

4.2.3.1 As received state (A-R)

The A-R state of the material is the hardest one with maximum strength but the lower ductility. The uniform plastic strain region is very small and the necking appears at about 3% of deformation. Figure 4.11 presents the true stress-strain curve of the A-R specimen in the logarithmic scale.

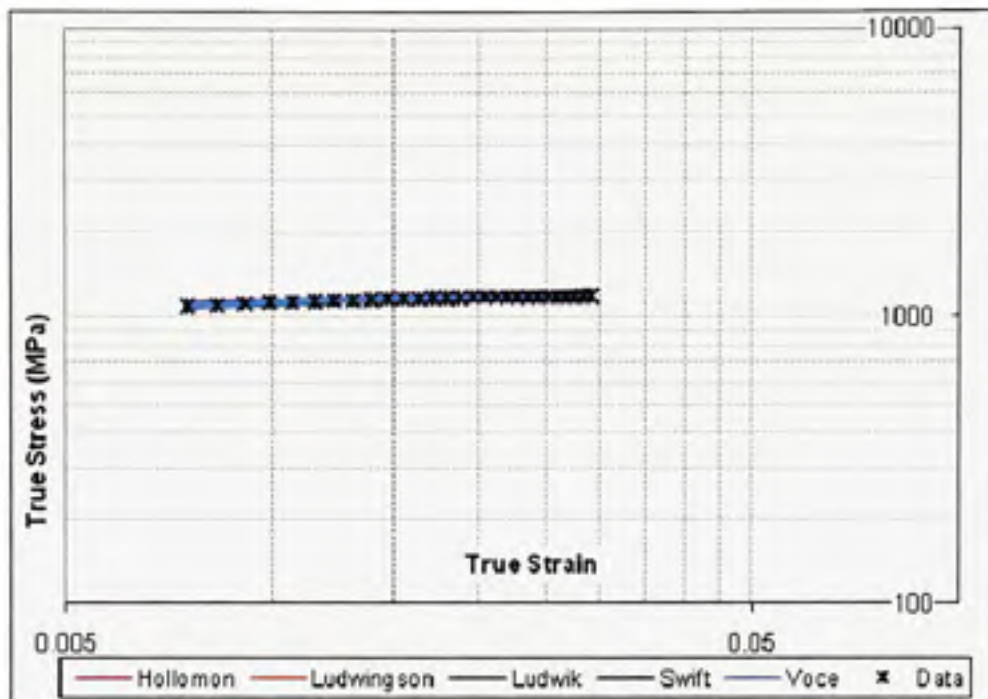


Figure 4.11 True stress-strain curves of SS 17-4 PH A-R specimen fitted by calculated hardening equations in the logarithmic scale.

One can see that the experimental data points of the A-R specimen on the log-log diagram are disseminated even if the number of experimental points is very limited. This is due to the fact that the A-R uniform plastic deformation covers a very small region. As a consequence, the fitting process does not seem to work well as seen in Table 4.5 and some divergences are notified.

Table 4.5 Best fit coefficients of the tested hardening equations – SS 17-4 PH as received specimens (A-R)

| A-R | Hollomon $\sigma = K \varepsilon_p^n$ | Ludwigson $\sigma = K \varepsilon_p^n + \exp(K_1 + n_1 \varepsilon_p)$ | | Ludwik $\sigma = \sigma_0 + K \varepsilon_p^n$ | Swift $\sigma = K (\varepsilon_0 + \varepsilon)^n$ | Voce $\sigma = \sigma_v - K_v \exp(n_v \varepsilon_p)$ |
|-----|--|---|-----------------|---|---|---|
| K | 1461.6 | 2169.8 | | 2316.5 | 1328.2 | $K_v = 344.6$ |
| n | 0.0553 | 0.2490 | | 0.0393 | 0.0275 | $n_v = -170.9277$ |
| | | $K_1 = 6.3020$ | $n_1 = -806.32$ | $\sigma_0 = -806.32$ | $\varepsilon_0 = -0.0067$ | $\sigma_v = 11193.5$ |
| S/N | 49 | 18 | | 74 | 7 | 1 |

The Voce and Swift equations possess the lowest S/N which means that those models are very close to the real data. In fact, these two equations are the only ones which present a concave curvature as the experimental data does. All the other equations are straight lines. Table 4.6 groups the evaluated YS by the hardening equations using the best fit coefficients and the offset strain.

Table 4.6 Calculated YS based on the best fit parameters of tested hardening equations – SS 17-4 PH in A-R state

| A-R | Hollomon $\sigma = K \varepsilon_P^n$ | Ludwigson $\sigma = K \varepsilon_P^n + \exp(K_1 + n_1 \varepsilon_P)$ | Ludwik $\sigma = \sigma_0 + K \varepsilon_P^n$ | Swift $\sigma = K (\varepsilon_0 + \varepsilon)^n$ | Voce $\sigma = \sigma_v - K_v \exp(n_v \varepsilon_P)$ | Experimental |
|-----|--|---|---|---|---|--------------|
| YS | 1037 | 985 | 1009 | 1146 | 949 | 1087 |

The calculation of YS based on the coefficients of the various hardening laws shows some variations. Even if the data curve seems to be best fitted with a smallest S/N, this does not mean that this equation gives the best hardening coefficient. In fact, in the case presented here, the Voce equation, with its lowest S/N does not give the most interesting YS. The Swift equation is the only one which combines a good S/N with calculated YS close to the reality. Also, the Hollomon equation suggests very interesting calculated YS, very close to the reality at $\varepsilon_P = 0.002$.

4.2.3.2 Annealing Overage heat treatment (AO)

AO is the softest condition of SS 17-4 PH. This heat treatment leads to an increase of the ductility, in other words, a delay in the necking apparition. Thus, the number of data points in the uniform plastic deformation range is increased a lot compared to the A-R specimen. The fitted true stress-strain curve of the AO specimen is presented in Figure 4.12.

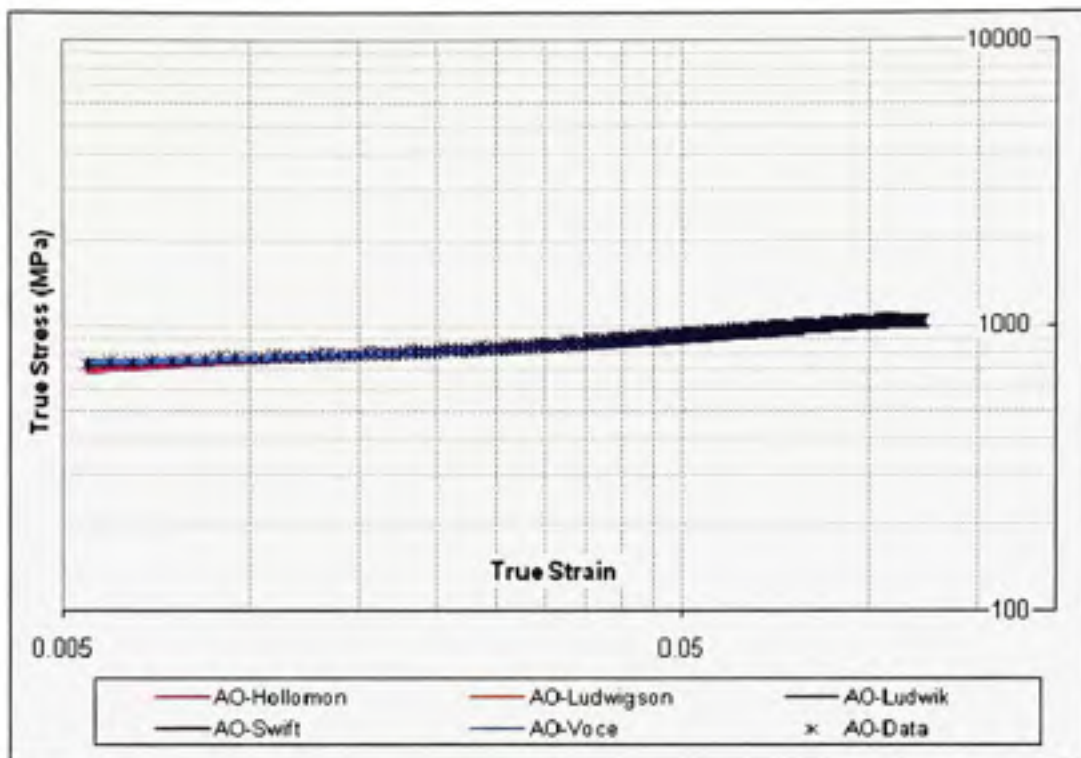


Figure 4.12 True stress-strain curves of SS 17-4 PH specimen heat treated by AO fitted by calculated hardening equations in the logarithmic scale.

First of all, the data points seems completely best fitted with all the hardening equations. Also, the true stress-strain curve in the logarithmic scale is closer to a straight line than in the A-R state. Table 4.7 detailed the best fit hardening coefficients obtained for the AO curve.

Table 4.7 Best fit coefficients of the tested hardening equations – SS 17-4 PH overage annealed specimens (AO)

| AO | Hollomon $\sigma = K \varepsilon^p^n$ | Ludwigson $\sigma = K \varepsilon^p^n + \exp(K_1 + n_1 \varepsilon^p)$ | Ludwik $\sigma = \sigma_0 + K \varepsilon^p^n$ | Swift $\sigma = K (\varepsilon_0 + \varepsilon)^n$ | Voce $\sigma = \sigma_v - K_v \exp(n_v \varepsilon_p)$ |
|-----|--|---|---|---|---|
| K | 1373.1 | 1520.0 | 1029.5 | 1477.2 | $K_v = 392.9$ |
| n | 0.1306 | 0.4977 | 0.3429 | 0.1673 | $n_v = -15.5469$ |
| | | $K_1 = 6.4321$ $n_1 = -1.4386$ | $\sigma_0 = 553.11$ | $\varepsilon_0 = 0.0097$ | $\sigma_v = 1103.8$ |
| S/N | 83 | 28 | 31 | 22 | 5 |

Based on the S/N parameter, the Hollomon equation seems very far from the data whereas the Voce equation is again the best fit. The other equations remain very close to each other.

The calculated YS from the hardening equations have been evaluated as well and the results are presented in Table 4.8. The estimated YS of all the equations are closer to the reality than in the case of the A-R specimen. However, all equations underestimated the YS. The Voce equation which possesses the lowest S/N is the closest in terms of calculated YS with 0.5% error on the YS estimation. In the other side, the Hollomon equation presents a high S/N and evaluates the YS 16% under the experimental data.

Table 4.8 Calculated YS based on the best fit parameters of tested hardening equations – SS 17-4 PH in AO state

| AO | Hollomon $\sigma = K \varepsilon_p^n$ | Ludwigson $\sigma = K \varepsilon_p^n + \exp(K_1 + n_1 \varepsilon_p)$ | Ludwik $\sigma = \sigma_0 + K \varepsilon_p^n$ | Swift $\sigma = K (\varepsilon_0 + \varepsilon)^n$ | Voce $\sigma = \sigma_v - K_v \exp(n_v \varepsilon_p)$ | Experimental |
|----|--|---|---|---|---|--------------|
| YS | 610 | 689 | 675 | 702 | 723 | 727 |

4.2.3.3 Precipitation hardening heat treatment (PH)

The PH is an intermediate heat treatment between the condition A and the annealing overage. It allows a good increase of the ductility without an important loss of strength. Figure 4.13 represents the true stress-strain curve of the PH specimen fitted by the designated hardening equations.

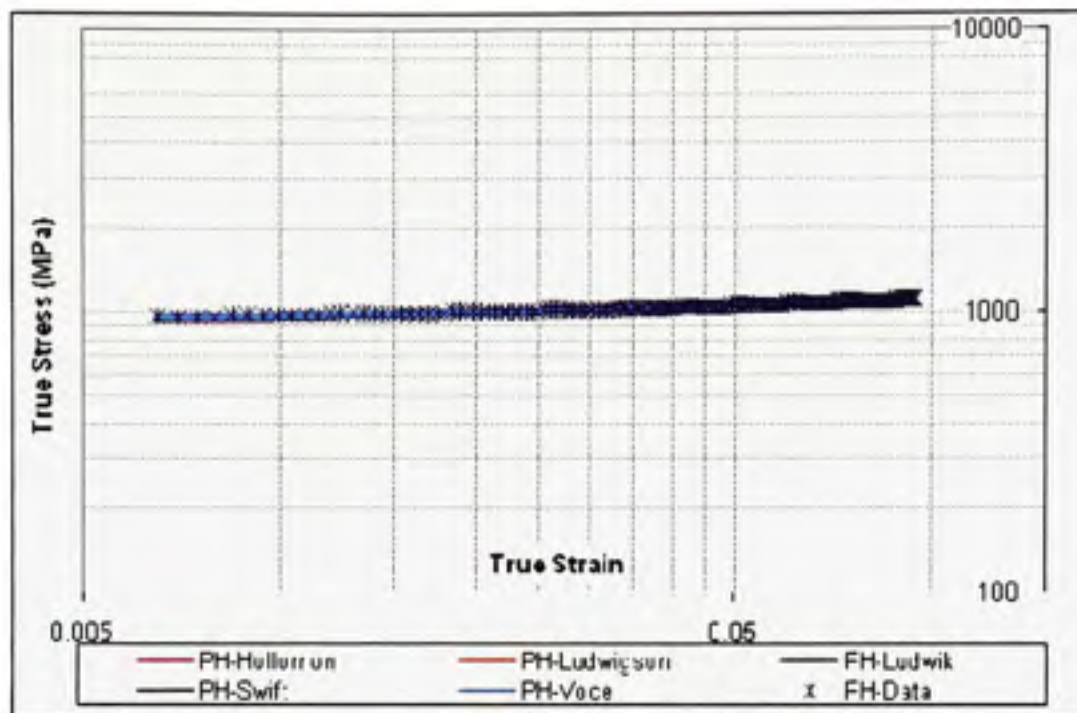


Figure 4.13 True stress-strain curves of SS 17-4 PH specimen heat treated by PH fitted by calculated hardening equations in the logarithmic scale.

As in the AO specimen case, the number of experimental process points for the PH curve is in appreciable quantity; this will contribute to improve the fitting. They also tend to a horizontal straight line. All the equations seem to fit very well the data. Table 4.9 holds the best fit coefficients of the studied hardening equations.

**Table 4.9 Best fit coefficients of the tested hardening equations
SS 17-4 PH - precipitation hardened specimens (PH)**

| PH | Hollomon $\sigma = K \varepsilon_P^n$ | Ludwigson $\sigma = K \varepsilon_P^n + \exp(K_1 + n_1 \varepsilon_P)$ | Ludwik $\sigma = \sigma_0 + K \varepsilon_P^n$ | Swift $\sigma = K (\varepsilon_0 + \varepsilon)^n$ | Voce $\sigma = \sigma_v - K_v \exp(n_v \varepsilon_P)$ |
|-----|--|---|---|---|---|
| K | 1265.7 | 1175.0 | 632.9 | 1381.1 | $K_v = 219.5$ |
| n | 0.0591 | 0.6273 | 0.4704 | 0.1026 | $n_v = -14.0267$ |
| | | $K_1 = 6.8210$ $n_1 = -0.8994$ | $\sigma_0 = 901.28$ | $\varepsilon_0 = 0.0233$ | $\sigma_v = 1165.7$ |
| S/N | 37 | 4 | 4 | 3 | 2 |

The S/N parameter in the case of PH specimens is quite low for all equations. Except the Hollomon equation which has the higher S/N, all the others remains at the same level and can be considered equivalent. The Voce equation, anew, presents the smallest S/N. The YS mechanical property has been estimated based on each equation and the resulting data have been consigned in Table 4.10.

Table 4.10 Calculated YS based on the best fit parameters of tested hardening equations
– SS 17-4 PH in PH state

| PH | Hollomon $\sigma = K \varepsilon_p^n$ | Ludwigson $\sigma = K \varepsilon_p^n + \exp(K_1 + n_1 \varepsilon_p)$ | Ludwik $\sigma = \sigma_0 + K \varepsilon_p^n$ | Swift $\sigma = K (\varepsilon_0 + \varepsilon)^n$ | Voce $\sigma = \sigma_v - K_v \exp(n_v \varepsilon_p)$ | Experimental |
|----|--|---|---|---|---|--------------|
| YS | 877 | 939 | 935 | 947 | 952 | 951 |

The YS calculated by all the equations are very close to the experimentally measured YS. In fact, the less close YS to the reality comes from the Hollomon equation which is only 74 MPa under the experimental data, that is less than 8 % underestimated. In the other side, the Voce equation reaches 0.1% error on the estimation of the YS.

4.2.4 Synthesis

The hardening behavior of SS 17-4 PH specimens in various metallurgical states differentiated by several heat treatments has been studied separately. Now, the effect of the heat treatment on the hardening coefficients is highlighted. For that, the most important hardening coefficients (K & n) obtained in each state and calculated for each equation have been plotted (except Voce's equation) respectively in Figures 4.14 and 4.15.

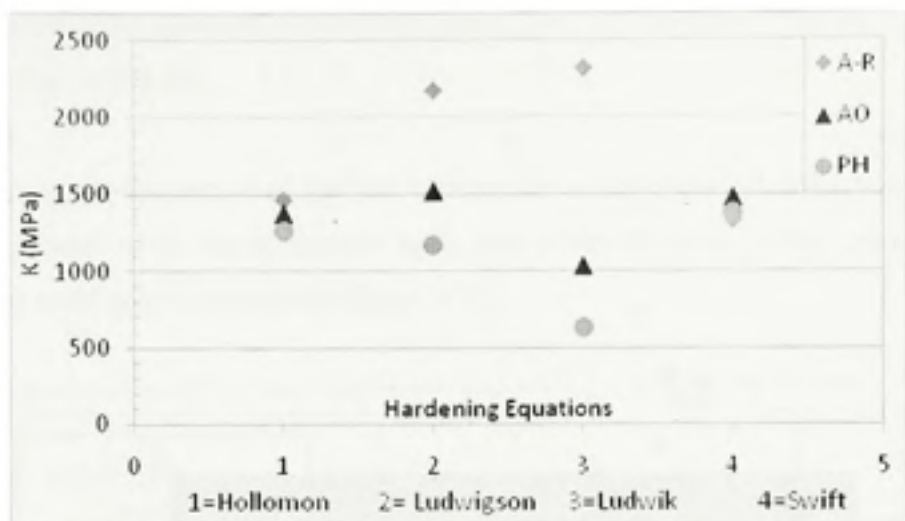


Figure 4.14 Best fit hardening coefficient K of each equation for A-R, AO and PH specimens of SS 17-4 PH.

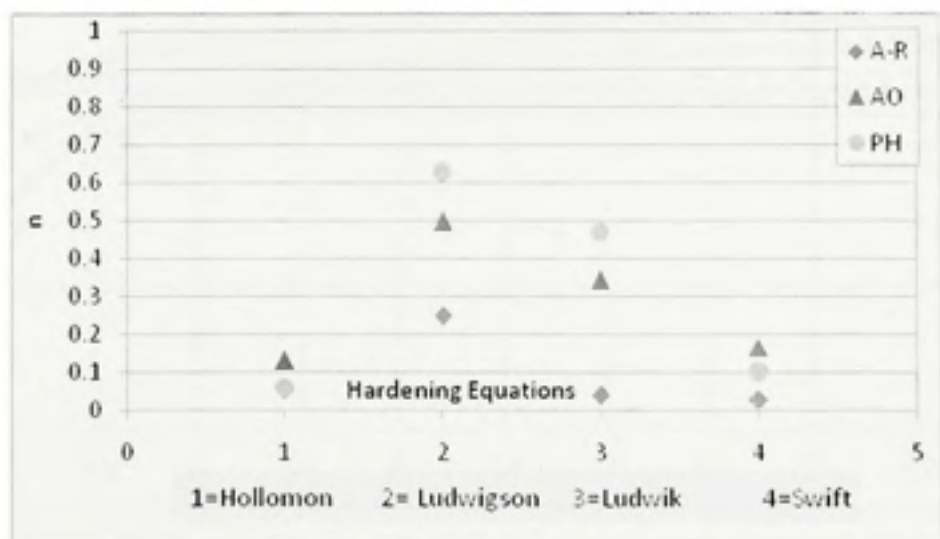
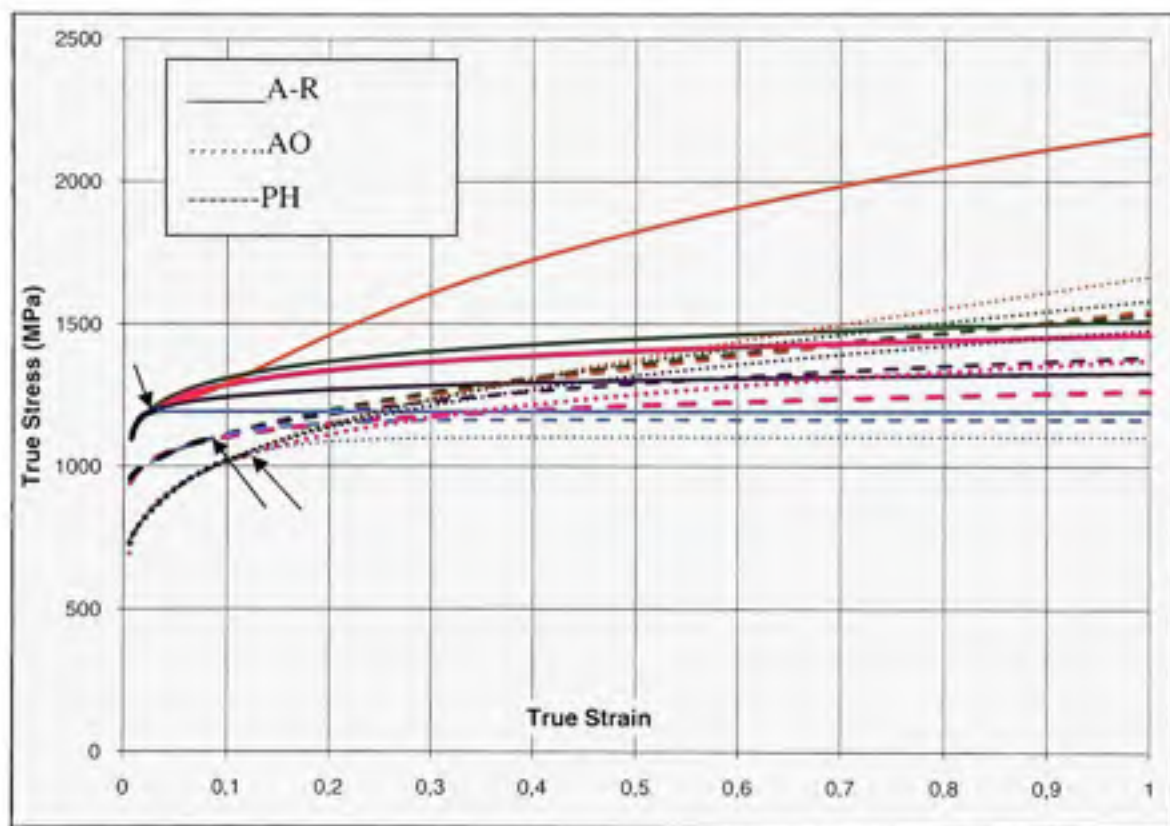


Figure 4.15 Best fit hardening coefficient n of each equation for A-R, AO and PH specimens of SS 17-4 PH.

The strength coefficient K is very high in all the equations, higher than 1000 MPa for most of the cases. The A-R specimen reaches very high level of stress. It is difficult to extract a tendency concerning the heat treatments impact on this hardening property. The divergence

of n values among the equations is very significant, from 0.03 to 0.6. But, in the majority, the n values are low, under 0.2.

In order to evaluate the impact of the heat treatments on large level of deformation, the true stress-strain curves of all the specimens have been extended up to 100% deformation and plotted in the same graph as shown in Figure 4.16.



**Figure 4.16 True stress-strain curves of SS 17-4 PH specimens (A-R, AO & PH) fitted by calculated hardening equations extended up to 100%.
The arrows represent the end of experimental data.**

The extended true stress-strain curves of all the specimens start to diverge as soon as the experimental data are stopped that is to say after less than 10% deformation. Beyond this point all the curves are mixed and any valuable differences can be extracted. The only exception concerns the Ludwiginson equation fitting the A-R specimen which increases

drastically and diverges completely from the other curves. Only FE modeling will give a possibility to know, with no doubt, which equation gives the best fit.

4.3 Superalloy Inconel 718

Inconel 718 is the most interesting material as it is widely used in the aerospace field. Because of its low availability and high cost, only few tests have been performed. INC 718 does not own a proper softening heat treatment. So, in order to test a different metallurgical state, a heat treatment called HT2 has been used and studied. HT2 has been conducted on tensile specimens cut from sheets in the rolling direction. The influence of a different starting state on the mechanical properties as well as the hardening behavior of INC 718 in these cases is studied.

4.3.1 Stress Relieve Heat treatment

The heat treatment conducted on INC 718 specimens to change the microstructure of the material prior to deformation is detailed in Figure 4.18. The heat treatment undergone before receiving the A-R specimens had not been revealed by the supplier. However, we supposed that they have been subjected to a classical solution treating followed by two steps of aging as depicted by Figure 4.17. HT2 corresponds to the ST heat treatment but with a faster cooling rate. It has been chosen because it is the only alternative heat treatment recipe available at PWC.

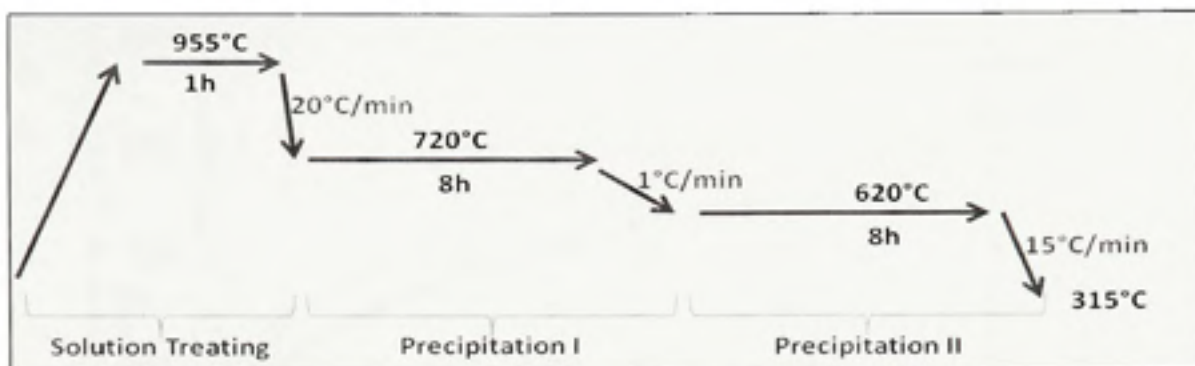


Figure 4.17 Heat treatment conducted on the A-R INC 718 specimens.

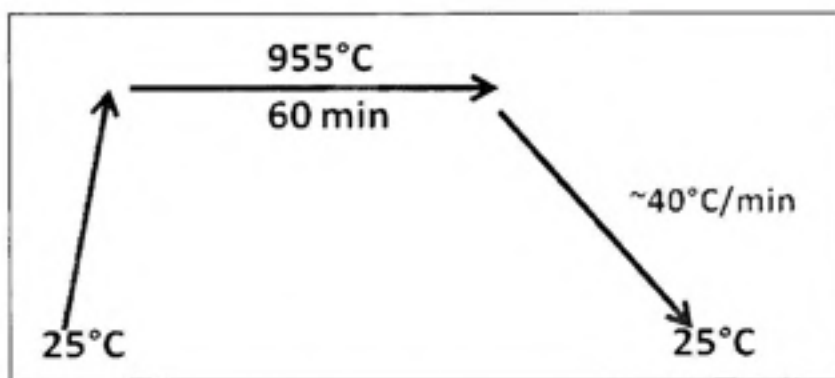


Figure 4.18 HT2 performed on INC 718 specimens.

The HT2 heat treatment corresponds to the annealed state depicted in section 1.3.3.2 whereas the A-R state does not correspond to any heat treatment given by the literature.

4.3.2 Stress-strain curves

Figure 4.19 presents the engineering stress-strain curves of INC 718 on both states. It is important to remind that each plotted curve represents an average of two tensile tests.

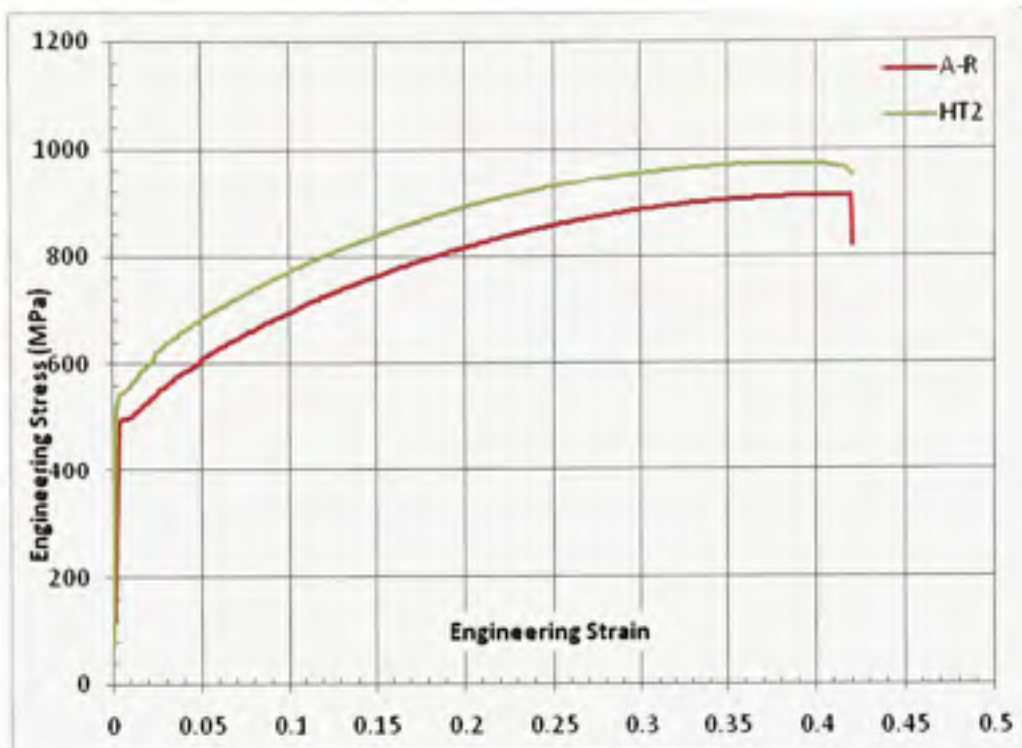


Figure 4.19 Engineering stress-strain curves of INC 718 flatted samples in A-R and HT2 states.

Both curves show a very similar trend. Even if the HT2 curve reaches higher stresses in the plastic strain region than the A-R curve, the necking strain as well as the breaking strain remains very close. Also, the elastic parts of both curves are coincided. Table 4.11 presents the mechanical properties of INC 718 specimens measured for both states.

Table 4.11 Mechanical properties of INC 718 flatted samples in A-R and HT2 states

| INC 718 | E (GPa) | YS (MPa) | UTS (MPa) | Necking strain | Breaking strain |
|---------|---------|----------|-----------|----------------|-----------------|
| A-R | 179 | 496 | 915 | 0.409 | 0.440 |
| HT2 | - | 541 | 974 | 0.380 | 0.431 |

In this case also, we could not evaluate the Young modulus for the same reasons as in the SS 321 case. When the mechanical properties obtained experimentally are compared to the literature data, one can observe that the A-R and the HT2 specimens presented both closed

data to the annealed state properties. But, in the two cases, the specimens reach higher YS and UTS than those suggested by the literature.

4.3.3 Hardening equations

In order to compare the hardening behavior of both metallurgical states of INC 718, their plastic true stress-strain curves have been plotted in the logarithmic scale on Figure 4.20.

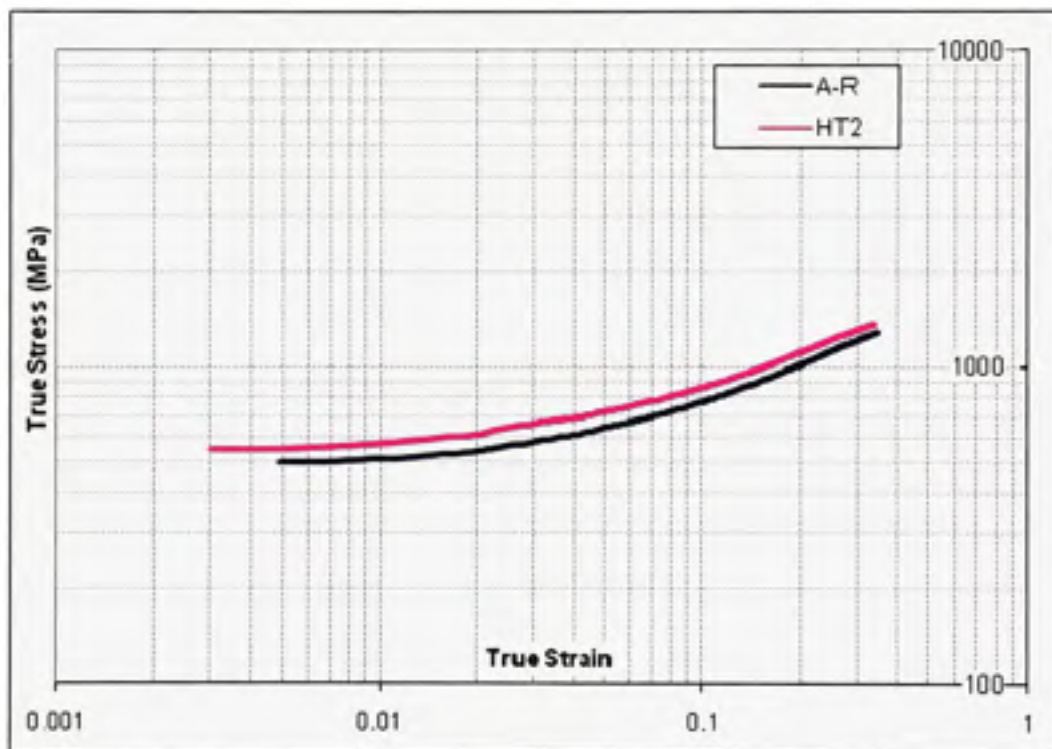


Figure 4.20 Comparison of true stress-strain curves of both A-R and HT2 specimens in logarithmic scale - INC 718.

The plastic strain region took up by both materials is almost the same. The HT2 curve is just a little shifted up compared to the A-R. Each curve has been fitted as previously to extract the best fit hardening coefficients.

4.3.3.1 As Received state

The plastic true stress-strain curve of INC 718 in the as received state has been fitted using the implemented method. The best fitted coefficients obtained allowed the plot of hardening curves which best fit the experimental data curve as shown in Figure 4.21.

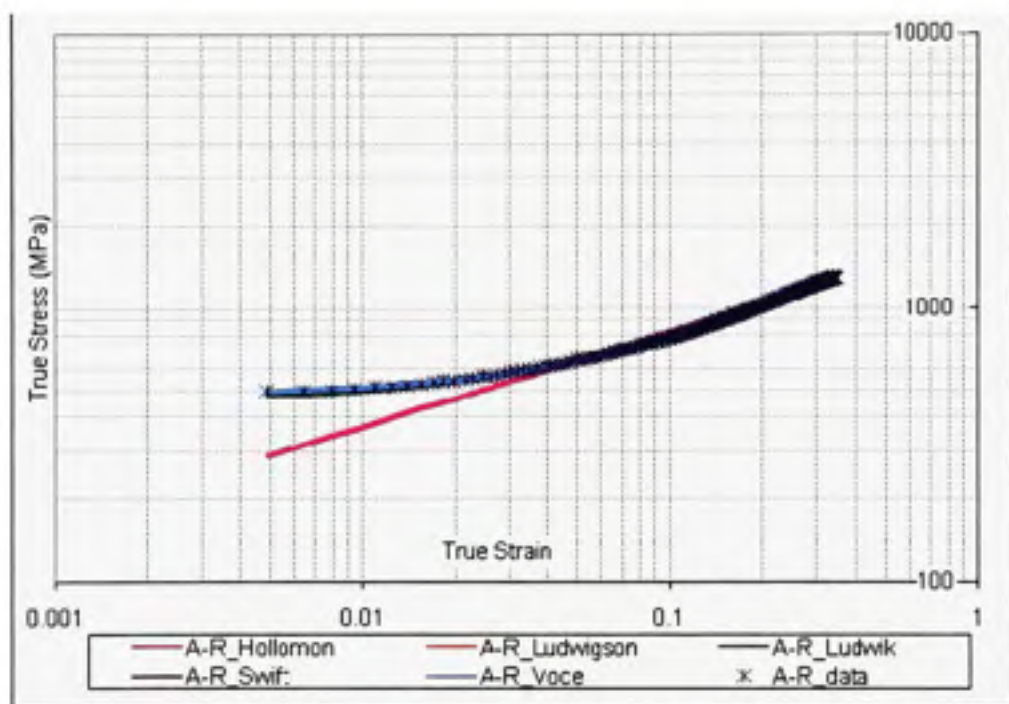


Figure 4.21 True stress-strain curves of INC 718 A-R specimens fitted by calculated hardening equations in the logarithmic scale.

Most of the studied equations fitted well the experimental curve. Only the Hollomon curve is in disagreement with the data as it cannot fit correctly the curve for strains lower than 4%. Beyond that point, all the curves fitted perfectly the data as the alloy behavior becomes quite linear. Table 4.12 summarized the best fit coefficients obtained for each hardening equation.

Table 4.12 Best fit coefficients of the tested hardening equations INC 718 in A-R state

| A-R | Hollomon $\sigma = K \epsilon_p^n$ | Ludwigson $\sigma = K \epsilon_p^n + \exp(K_1 + n_1 \epsilon_p)$ | Ludwik $\sigma = \sigma_0 + K \epsilon_p^n$ | Swift $\sigma = K (\epsilon_0 + \epsilon)^n$ | Voce $\sigma = \sigma_v - K_v \exp(n_v \epsilon_p)$ |
|-----|---------------------------------------|---|--|---|--|
| K | 1803.2 | 2065.0 | 1914.1 | 2146.6 | $K_v = 1604.9$ |
| n | 0.3443 | 0.8117 | 0.7479 | 0.5702 | $n_v = -2.0427$ |
| | | $K_1 = 6.1390$ | $n_1 = -0.12$ | $\sigma_0 = 440.39$ | $\epsilon_0 = 0.0699$ |
| S/N | 1641 | 65 | 35 | 18 | 9 |

The S/N parameter calculated returns some differences from one equation to the other. As expected, the Hollomon equation has the largest S/N. The Ludwigson equation follows, but with an S/N 25 times smaller. Finally, all the other equations seem more or less closed with the smallest S/N for the Voce equation.

The YS estimated by the equations is in accordance with the experimental calculated YS except for the Hollomon equation (Table 4.13). However, all the equations underestimated the reality. If the Voce equation, which is the closest parameter, is about 1.6% less than the measured YS, the others are up to 7.5% less than what is expected except Hollomon which has its YS half underestimated. Based on these results, one can conclude that the coefficients extracted well represent the experimental case.

Table 4.13 Calculated YS based on the best fit parameters of tested hardening equations - INC 718 in A-R state

| A-R | Hollomon $\sigma = K \epsilon_p^n$ | Ludwigson $\sigma = K \epsilon_p^n + \exp(K_1 + n_1 \epsilon_p)$ | Ludwik $\sigma = \sigma_0 + K \epsilon_p^n$ | Swift $\sigma = K (\epsilon_0 + \epsilon)^n$ | Voce $\sigma = \sigma_v - K_v \exp(n_v \epsilon_p)$ | Experimental |
|-----|---------------------------------------|---|--|---|--|--------------|
| YS | 212 | 477 | 459 | 478 | 488 | 496 |

4.3.3.2 HT2 heat treatment

The plastic true stress-strain curve of INC 718 specimen has been fitted by the hardening equations as presented in Figure 4.22 and Table 4.14 detailed the best fit coefficients

extracted for each hardening equation. The same observations as for the A-R specimen can be made since both curves were very close.

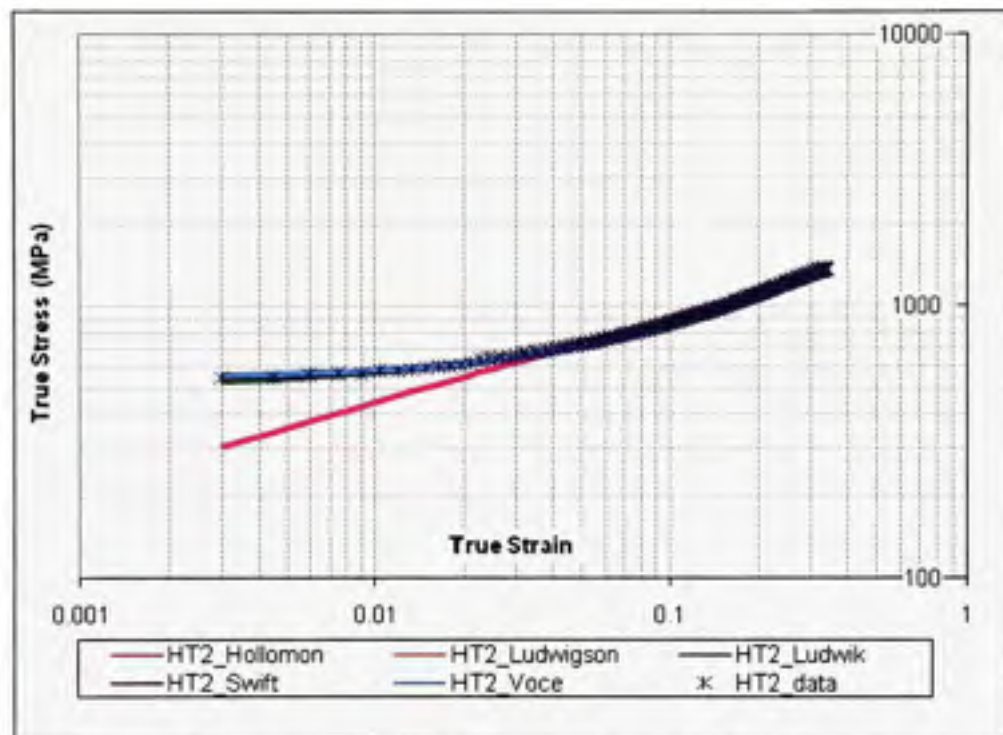


Figure 4.22 True stress-strain curves of INC 718 HT2 specimens fitted by calculated hardening equations in the logarithmic scale.

Table 4.14 Best fit coefficients of the tested hardening equations INC 718 in HT2 state

| HT2 | Hollomon $\sigma = K \varepsilon P^n$ | Ludwigson $\sigma = K \varepsilon P^n + \exp(K_1 + n_1 \varepsilon_P)$ | | Ludwik $\sigma = \sigma_0 + K \varepsilon P^n$ | Swift $\sigma = K (\varepsilon_0 + \varepsilon)^n$ | Voce $\sigma = \sigma_v - K_v \exp(n_v \varepsilon_P)$ |
|-----|--|---|-------------------|---|---|---|
| | K | 2042.6 | 1930.2 | 2215.3 | K _v =1500.3 | |
| n | 0.3119 | 0.7518 | 0.7181 | 0.5207 | n _v =-2.3611 | |
| | | K ₁ =6.2382 n ₁ =-0.1435 | $\sigma_0=499.92$ | $\varepsilon_0=0.0654$ | $\sigma_v=2049.5$ | |
| S/N | 1982 | 46 | 38 | 26 | 23 | |

The Swift and Voce equations are very closed but Voce's equation presents the smallest S/N. Then again, the Hollomon curve, because of the straightness of its equation on such a graph is the worst fit in terms of S/N parameter. The Ludwigson and Ludwik equations follow with S/N more than 40% less in relation to the Hollomon one.

The estimation of YS has also been performed and the results consigned in Table 4.15.

Table 4.15 Calculated YS based on the best fit parameters of tested hardening equations INC 718 in HT2 state

| | Hollomon $\sigma = K \varepsilon P^n$ | Ludwigson $\sigma = K \varepsilon P^n + \exp(K_1 + n_1 \varepsilon P)$ | Ludwik $\sigma = \sigma_0 + K \varepsilon P^n$ | Swift $\sigma = K (\varepsilon_0 + \varepsilon)^n$ | Voce $\sigma = \sigma_v - K_v \exp(n_v \varepsilon P)$ | Experimental |
|-----|--|---|---|---|---|--------------|
| HT2 | 268 | 531 | 522 | 544 | 556 | 541 |
| YS | | | | | | |

The estimated YS with the hardening coefficients calculated are very close to the reality. The Voce and Swift equations overvalued a little the YS, about 2.8% and 0.5% respectively. All the other equations underestimated the yield. Except for the Hollomon equation, the hardening equations presented fitted very well the experimental data and neither the S/N parameter nor the YS estimation can be able to discriminate one equation compared to the other.

4.3.4 Synthesis

In order to evaluate the impact of the heat treatment on the hardening equations, the most important coefficients (K & n) of each equation except Voce in both states have been plotted respectively in Figures 4.23 and 4.24.

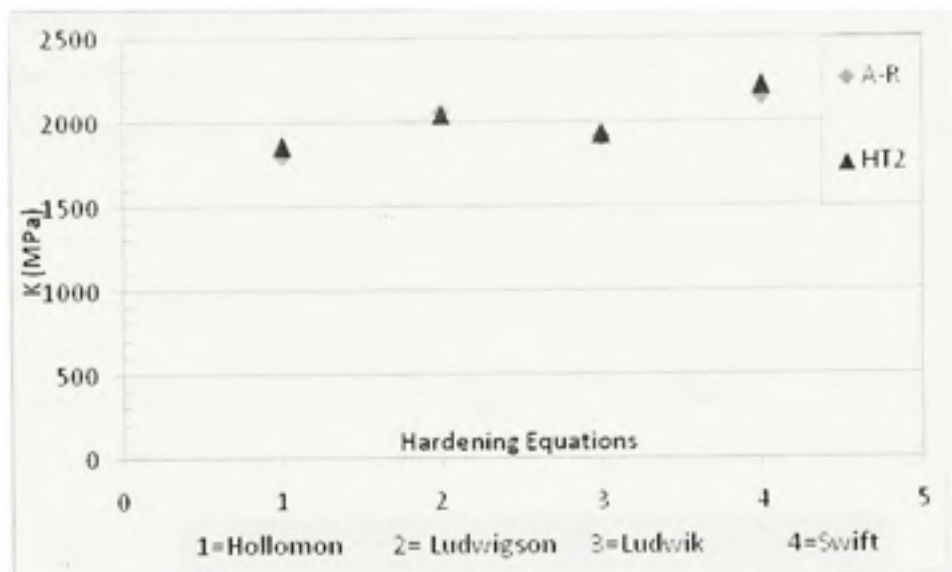


Figure 4.23 Best fit hardening coefficient K of each equation for A-R and HT2 specimens of INC 718.

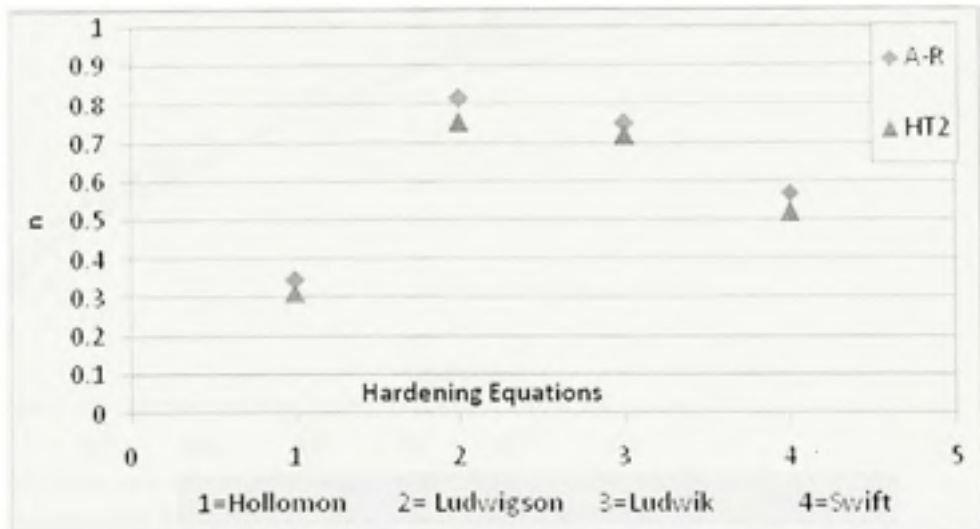


Figure 4.24 Best fit hardening coefficient n of each equation for A-R and HT2 specimens of INC 718.

Only, the hardening coefficient n carried a tiny impact of the heat treatment. In fact, the hardening strength K in all the equations is very high and is around 2000 MPa. For a given equation, no difference is observed on K when the metallurgical state is changed. For all equations, the A-R n values are a little higher than the HT2 n values (about +0.05). The

mechanical properties of both materials as well as the hardening coefficients seem very closed. Some differences can be observed on the strain hardening coefficient n which decreased when an HT2 heat treatment is applied on the specimen.

To evaluate the heat treatment influence on high levels of strain, the true stress-strain curves of both A-R and HT2 specimens have been extended up to 100% deformation in Figure 4.25.

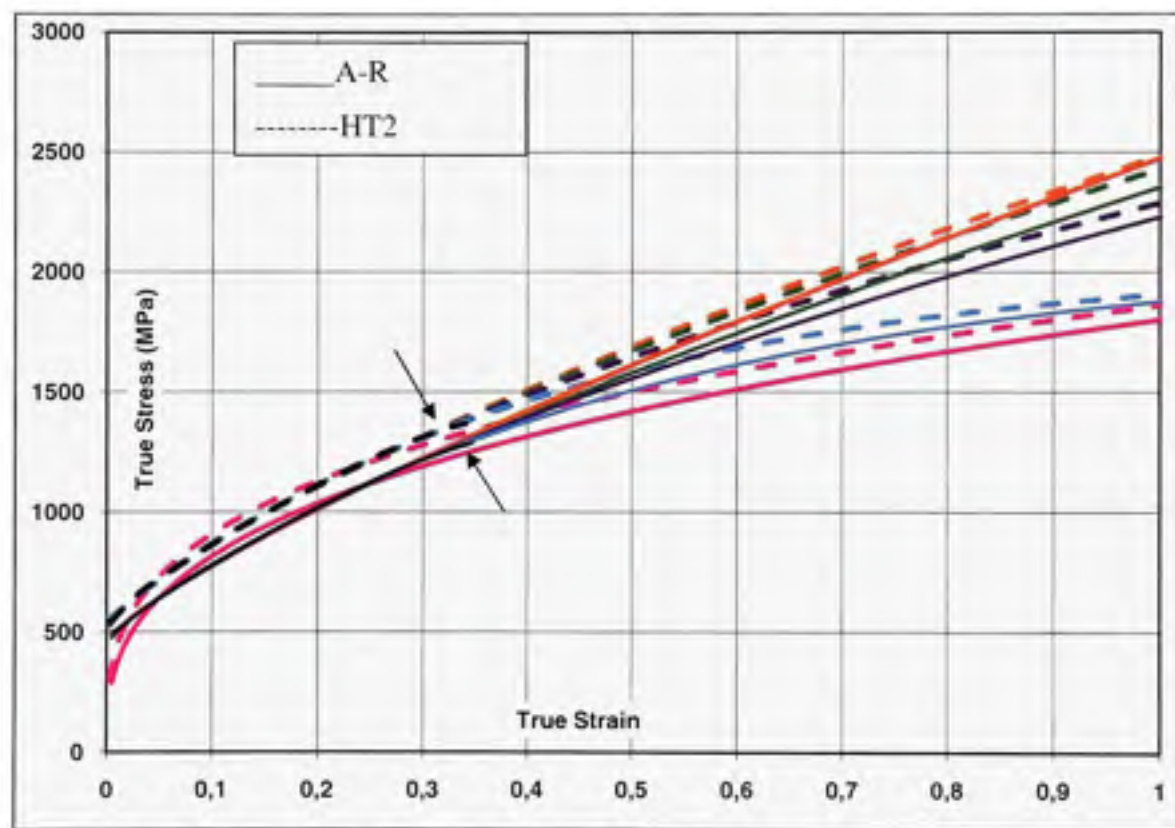


Figure 4.25 True stress-strain curves of INC 718 specimens (A-R & HT2) fitted by calculated hardening equations extended up to 100%. The arrows correspond to the end of experimental data.

The extended true stress-strain curves present a small divergence on the experimental data range. Beyond that section, all the curves start to merge. In both cases, the Voce and Hollomon equations do not predict strain hardening whereas the others continue to increase.

The study of different metallurgical states of INC 718 in terms of mechanical properties and hardening behavior leads to several conclusions. First of all, the proposed heat treatment performed does not have a significant influence on the mechanical properties of INC 718. Then, the hardening behavior in both cases is very close. The small differences observed coming from the heat treatment affected the strain hardening coefficient n . After the heat treatment, the n value increases slightly. Finally, the heat treatment applied does not bring any additional ductility to the material. Thus, it could be costly and not really interesting for the material.

CONCLUSIONS

The purpose of the present work was to define characterization methods of particular aerospace alloys for tube hydroforming applications. Hydroforming is widely used in the automotive industry but quite unknown in the aerospace field because of the lack of knowledge concerning the formability of aerospace materials. Thus, the formability of designated aerospace alloys has been documented in the present work with the objective of building material models for FEM simulations of tube hydroforming of aerospace parts.

The studied materials were the stainless steels SS 321, SS 17-4 PH, and the nickel-based superalloy ING 718. The mechanical tests were mainly uniaxial tensile tests and free expansion tests. The latter were chosen for their closeness to the hydroforming process. All the tests have been conducted using an automated digital images correlation system, Aramis®, to record the deformation in the case of tensile tests and the bulge height in the case of free expansion tests.

The results were used in combination with a systematic methodology to extract the constitutive equations which describe the hardening behaviour of the material. The effect of the specimens' geometries and directions has been evaluated in the case of SS 321 as well as the impact of a different starting metallurgical state on the formability of all the alloys. On one hand, in order to consider the potential influence of the laminated direction, tensile specimens of SS 321 have been cut from sheet in three directions, i.e., RD, 45D, TD. The results have shown that a limited impact of the direction is observed for this alloy either in the mechanical properties or on the hardening coefficients. On the other hand, the tests performed on curved specimens have shown a significant effect of the thickness on both mechanical properties and hardening behavior. Since the thinner tube had undergone a different forming path, its mechanical properties have been modified. That means that it is essential to take into account the previous life of the material to be able to better understand its mechanical behavior.

This part of the work has also been the occasion to test a program which allows the estimation of true stress-strain curves from free expansion tests. Thus, the true stress-strain curves from flat sheets, curved specimens and the calculated curves from tubes were compared. The curved and flattened tensile specimens have given similar curve shapes but the calculated curves which are supposed to reflect the biaxiality of the free expansion tests have led similar necking strain without reaching higher stresses, which is quite surprising. Several hypotheses have been proposed to confirm or infirm those results. First, the experimental procedure to extract the bulge height could be improved. Then, the Matlab program used to evaluate the stress and strain and which contains several assumptions could be reviewed and confirmed. Finally, other tests could be conducted on different materials to define if this is not linked to the material properties.

The impact of various metallurgical states on the mechanical behavior on the material properties has been studied for the 3 different alloys under investigation. The as-received state has been compared to other starting metallurgical states. On the SS 321, a stress relief heat treatment has been conducted. The results have shown that this heat treatment increases the ductility of the material as well as its strain hardening coefficient. However, when the strains are extrapolated to higher levels of strains, no significant differences are observed. Concerning the SS 17-4 PH, two heat treatments have been tested and compared to the as-received hardened state. The so-called annealing overage (AO) heat treatment conducts to the softest condition with lower yield stress and UTS but lead to higher ductility. The precipitation hardening (PH) heat treatment leads to conditions between the as-received very hard state and the AO. In all the cases, the heat treatment applied leads to a modification of the mechanical properties as well as the hardening behavior of the material. Finally, the INC 718 has been subjected to a solution treating treatment. In this case, the application of the heat treatment does not bring any major changes with just the strain hardening coefficient decreasing a little after the heat treatment.

This study has been an investigative work and has brought out several research paths. As future work, it will be interesting to generalize the study conducted on SS 321 to the others

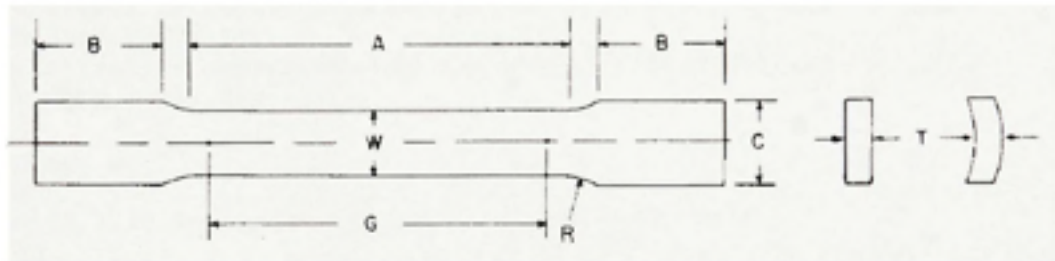
aerospace involved in this research. Then, all the developed constitutive equations should be implemented in the FEM and compared to experiments to find the optimized material parameters for HF applications. Finally, the effect of multistage forming process to improve the formability of aerospace alloys should be investigated. The metallurgical phenomena which are take place during the heat treatments correlated with the multistage processes should be study more deeply to be able to predict the mechanical behavior.

ANNEX I

STANDARD TEST METHODS FOR TENSION OF METALLIC MATERIALS

ASTM E 8 - 04 - Extract

 E 8 - 04



| Specimen 1 | |
|---|--------------------|
| | in. |
| G—Gage length | 2.000 ± 0.005 |
| W—Width (Note 1) | 0.500 ± 0.010 |
| T—Thickness | measured thickness |
| R—Radius of fillet, min | $\frac{1}{2}$ |
| A—Length of reduced section, min | $2\frac{1}{4}$ |
| B—Length of grip section, min (Note 2) | 3 |
| C—Width of grip section, approximate (Note 3) | $1\frac{1}{16}$ |

ANNEX II

MATLAB PROGRAM FOR HARDENING EQUATIONS EXTRACTION

```
clear all
close all
% Excel file reading
% --> All the data are inserted in N matrix
nom_fichier='C:\Documents and Settings\ah61490\Mes
documents\Maitrise_CRIAQ\Hardening laws\174-0-2-2.xlsm';
N = xlsread(nom_fichier,'Hardening law','A3:B20');
% True strain is represented by the matrix N first column (x data)
strain_data = N(:,1);
% True stress is represented by the matrix N second column (y data)
stress_data = N(:,2);

% Display
figure
subplot(1,1,1),loglog(strain_data, stress_data, ' ')
grid on
title('True stress-strain data curve','FontSize',9,'Color','blue');
xlabel('Strain'),ylabel('Stress (MPa)');

%%%%%%%%%%%%%%%
% Program which fit the best law to the aforementioned data %
%%%%%%%%%%%%%%%
% Initial conditions for the wanted values --> order of magnitude for K &
n values (hardening coefficients)
%InitialConditions = [0.00000001 0.00000001];
options = optimset('MaxIter',10000);
options.MaxFunEvals = 10e90;

% "newParameters" is a table containing the optimum values which will
% generate the curve that best-fit strain_data and stress_data
% "sumres" is the sum of residual squares. Smaller is sumres, better is
the fitting

%%%%%%%%%%%%%%%
% HOLLOWMON %%%%%%%%%%%%%%%
InitialConditions = [1790 0.1];
lb = [10e-15 10e-15];
ub = [10e45 10e45];
[newParametersl, sumresl, residuall, exitflagl, outputl] =
lsqcurvefit(@Hollowmon, InitialConditions, strain_data, stress_data);

% Use of the new parameters to obtain new values for curve plot (output)
yl = Hollowmon(newParametersl, strain_data);
Kh = newParametersl(:,1);
nh = newParametersl(:,2);
```

```

stress_Hollomon=y1;

%%%%%%%%%%%%% LUDWIGSON %%%%%%
InitialConditions = [1900 0.1 5 -20];
lb = [0 0 0 -1000];
ub = [20000 1000 1000 0];
[newParameters2, sumres2, residual2, exitflag2, output2] =
lsqcurvefit(@Ludwigson, InitialConditions, strain_data, stress_data)

% Use of the new parameters to obtain new values for curve plot (output)
y2 = Ludwigson(newParameters2, strain_data);
K1 = newParameters2(:,1);
n1 = newParameters2(:,2);
K1 = newParameters2(:,3);
n1 = newParameters2(:,4);
stress_Ludwigson=y2;

%%%%%%%%%%%%% LUDWIK %%%%%%
InitialConditions = [1700 0.1 50];
lb = [10e-9 10e-9 10e-9];
ub = [10e37 10e37 10e37];
[newParameters3, sumres3, residual3, exitflag3, output3] =
lsqcurvefit(@Ludwik, InitialConditions, strain_data, stress_data)

% Use of the new parameters to obtain new values for curve plot (output)
y3 = Ludwik(newParameters3, strain_data);
Kk = newParameters3(:,1);
nk = newParameters3(:,2);
S0 = newParameters3(:,3);
stress_Ludwik=y3;

%%%%%%%%%%%%% SWIFT %%%%%%
InitialConditions = [9000 0.8 0.05];
lb = [10e-9 10e-9 10e-9];
ub = [10e37 10e37 10e37];
[newParameters4, sumres4, residual4, exitflag4] = lsqcurvefit(@Swift,
InitialConditions, strain_data, stress_data)

% Use of the new parameters to obtain new values for curve plot (output)
y4 = Swift(newParameters4, strain_data);
Ks = newParameters4(:,1);
ns = newParameters4(:,2);
Eps0 = newParameters4(:,3);
stress_Swift=y4;

%%%%%%%%%%%%% VOCE %%%%%%
InitialConditions = [500 -100 1000];
lb = [10e-9 10e-9 10e-9];
ub = [10e37 10e37 10e37];
[newParameters5, sumres5, residual5, exitflag5, output5] =
lsqcurvefit(@Voce, InitialConditions, strain_data, stress_data);

```

```
% Use of the new parameters to obtain new values for curve plot (output)
y5 = Voce(newParameters5, strain_data);
Kv = newParameters5(:,1);
nv = newParameters5(:,2);
Sv = newParameters5(:,3);
stress_Voce=y5;

% Display of the real data (blue) and the calculated data
% Hollomon = red / Ludwigson = green / Ludwik = magenta / Swift = black /
% Voce = cyan

hold

semilogx(strain_data, y1, 'r');
semilogx(strain_data, y2, 'g');
semilogx(strain_data, y3, 'm');
semilogx(strain_data, y4, 'k');
semilogx(strain_data, y5, 'c');

h = legend('Data','Hollomon','Ludwigson','Ludwik','Swift','Voce',6);
set(h,'Interpreter','none')

% The coefficients as well as the calculated stress data are written into
% the excel sheet

DATA=[strain_data stress_data stress_Hollomon stress_Ludwigson
stress_Ludwik stress_Swift stress_Voce];
d = xlswrite(nom_fichier,DATA, 'matlab','A3');

coef={'Laws', 'Hollomon', 'Ludwigson', 'Ludwik', 'Swift', 'Voce';'K' Kh Kl
Kk Ks Kv; 'n' nh nl nk ns nv;'K1/S0/Eps0/sigmaV' 0 K1 S0 Eps0 Sv; 'nl' 0
nl 0 0 0; 'sumres' sumres1 sumres2 sumres3 sumres4 sumres5};
s = xlswrite(nom_fichier,coef, 'matlab','I7');

%%%%%%%%%%%%%%%
function fono_Hollomon = Hollomon(param, input)
% the calculating parameters are given to the program
Kh = param(1);
nh = param(2);
% Equation to solve
sigma = Kh.*input.^{nh};
fono_Hollomon = sigma;
```

ANNEX III

45D AND TD SPECIMENS FROM SHEETS DATA

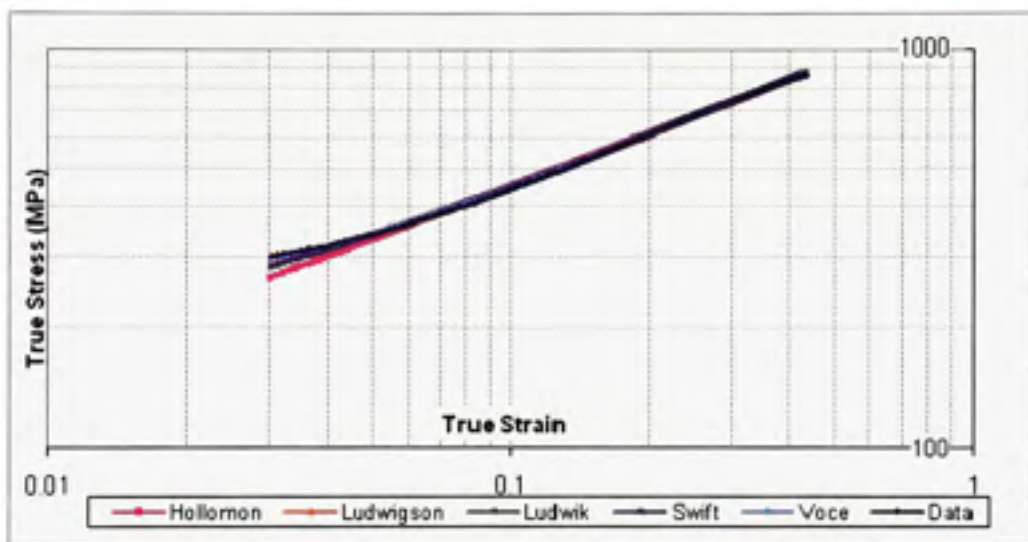


Figure-A III.1 Stress-strain curve of SS 321-45D fitted by calculated hardening equations in the logarithmic scale.

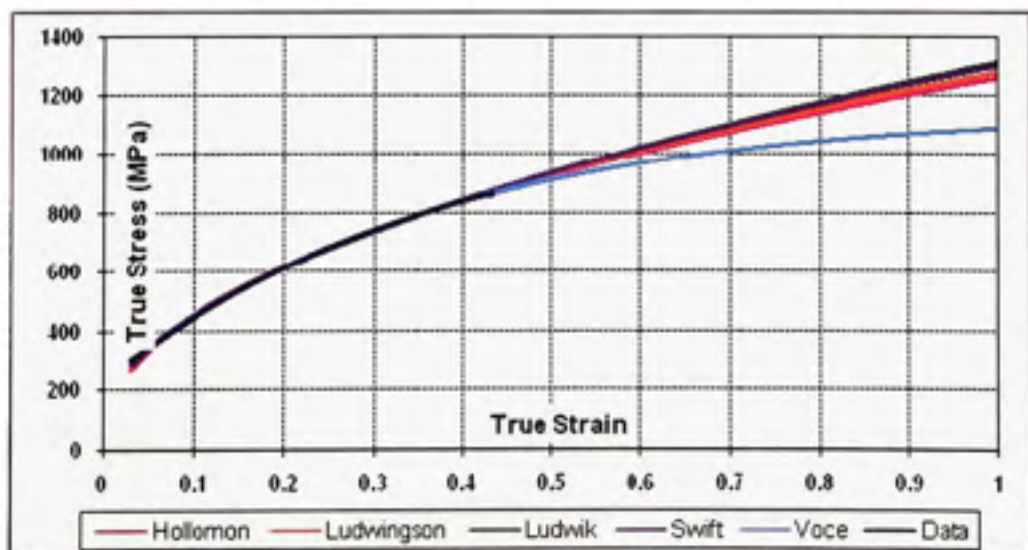


Figure-A-III.2 Stress-strain curves of SS 321-45D by calculated hardening equations extended up to 100%.

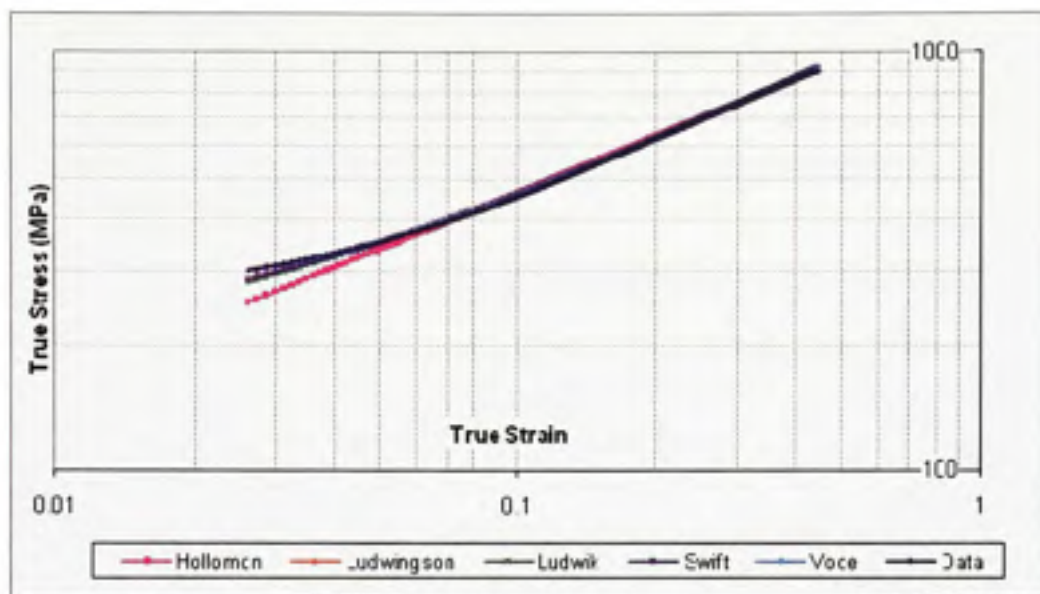


Figure-A-III.3 Stress-strain curve of SS 321-TD fitted by calculated hardening equations in the logarithmic scale.

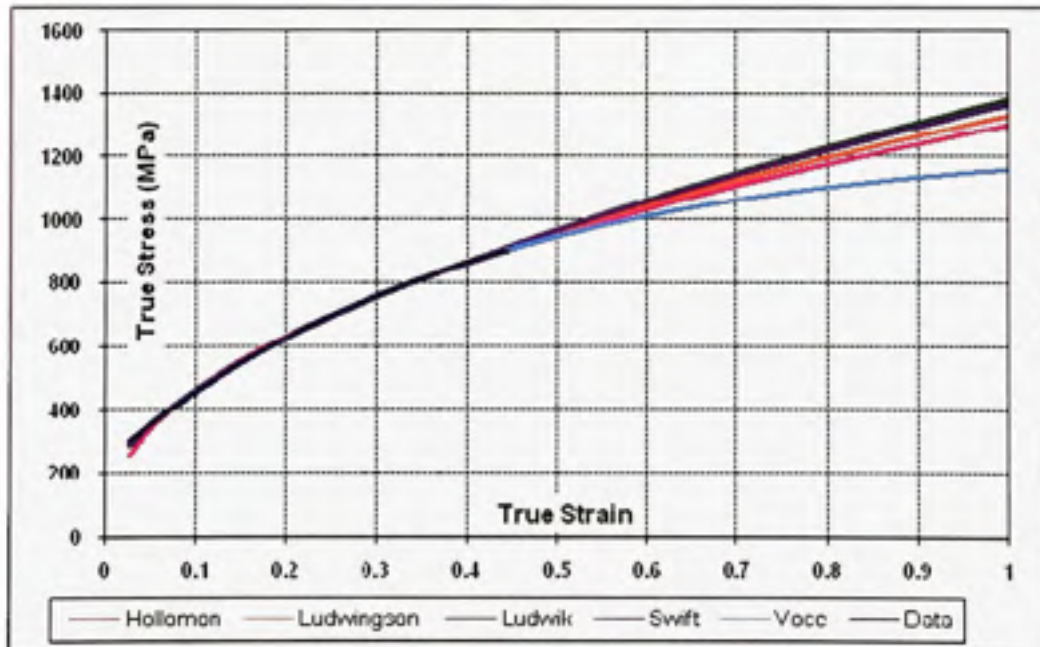


Figure-A-III.4 Stress-strain curves of SS 321-TD by calculated hardening equations extended up to 100.

ANNEX IV

1.2 mm THICKNESS CURVED SPECIMENS DATA

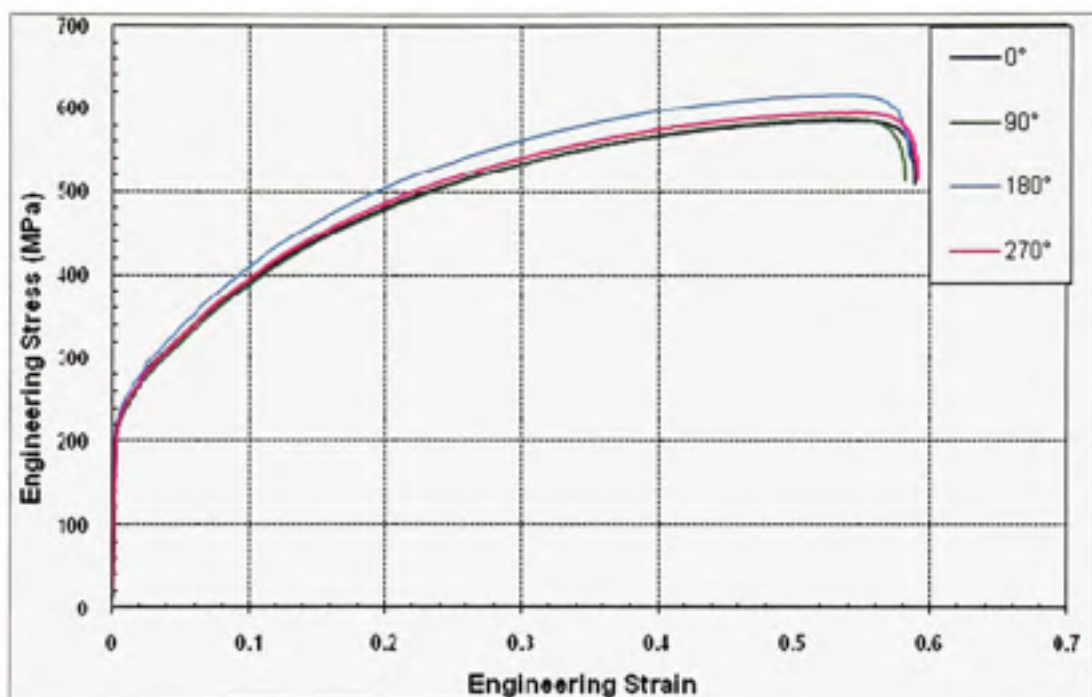
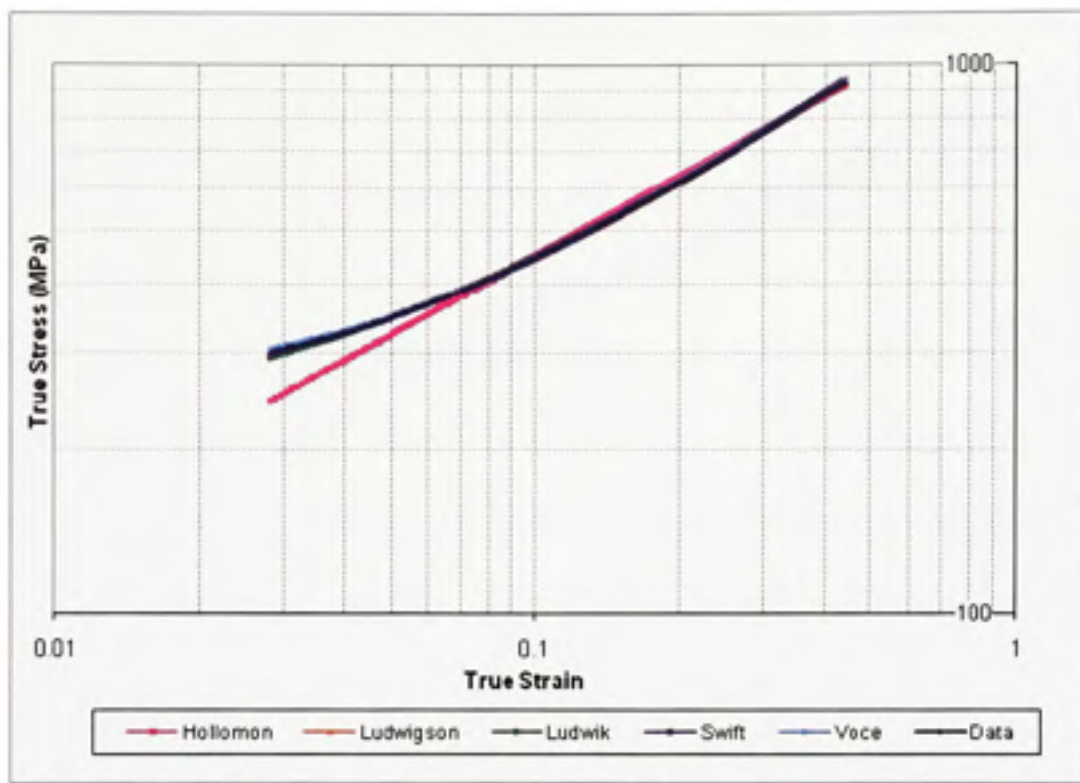


Figure-A-IV.1 Engineering stress-strain curves of SS 321 curved samples cut all over the tube – 1.2 mm thick.

Table-A-IV.1 Mechanical properties of SS 321 curved samples– 1.2 mm thick

| 1.2 thick curved | YS (MPa) | UTS (MPa) | Necking elongation | Break elongation |
|-------------------|----------|-----------|--------------------|------------------|
| 321 – 0° | 224 | 585 | 0.529 | 0.590 |
| 321 – 90° | 218 | 587 | 0.535 | 0.583 |
| 321 – 180° | 229 | 617 | 0.528 | 0.586 |
| 321 – 270° | 219 | 595 | 0.545 | 0.593 |
| Average | 223 | 596 | 0.534 | 0.588 |



**Figure-A-IV.2 Stress-strain curve of SS 321 curved specimen
1.2 mm thick fitted by calculated hardening equations in the logarithmic scale.**

**Table-A-IV.2 Best fit coefficients of the tested hardening equations
SS321 curved specimens – 1.2 mm thick**

| 1.2 curved | Hollomon $\sigma = K \epsilon^{\alpha}$ | Ludwigson $\sigma = K \epsilon^{\beta} + \exp(K_1 + n_1 \epsilon \rho)$ | Ludwik $\sigma = \sigma_0 + K \epsilon^{\gamma}$ | Swift $\sigma = K (\epsilon_0 + \epsilon)^n$ | Voce $\sigma = \sigma_v - K_v \exp(n_v \epsilon \rho)$ |
|------------|--|--|---|---|---|
| K | 1354.5 | 1440.3 | 1334.7 | 1449.0 | $K_v = 1354$ |
| n | 0.4793 | 0.5342 | 0.7072 | 0.6160 | $n_v = -1.5912$ |
| | | $K_1 = 4.9084$ $n_1 = -17.1100$ | $\sigma_0 = 186.14$ | $\epsilon_0 = 0.0481$ | $\sigma_v = 1599.0$ |
| S-R | 89801 | 744 | 2871 | 1583 | 1037 |

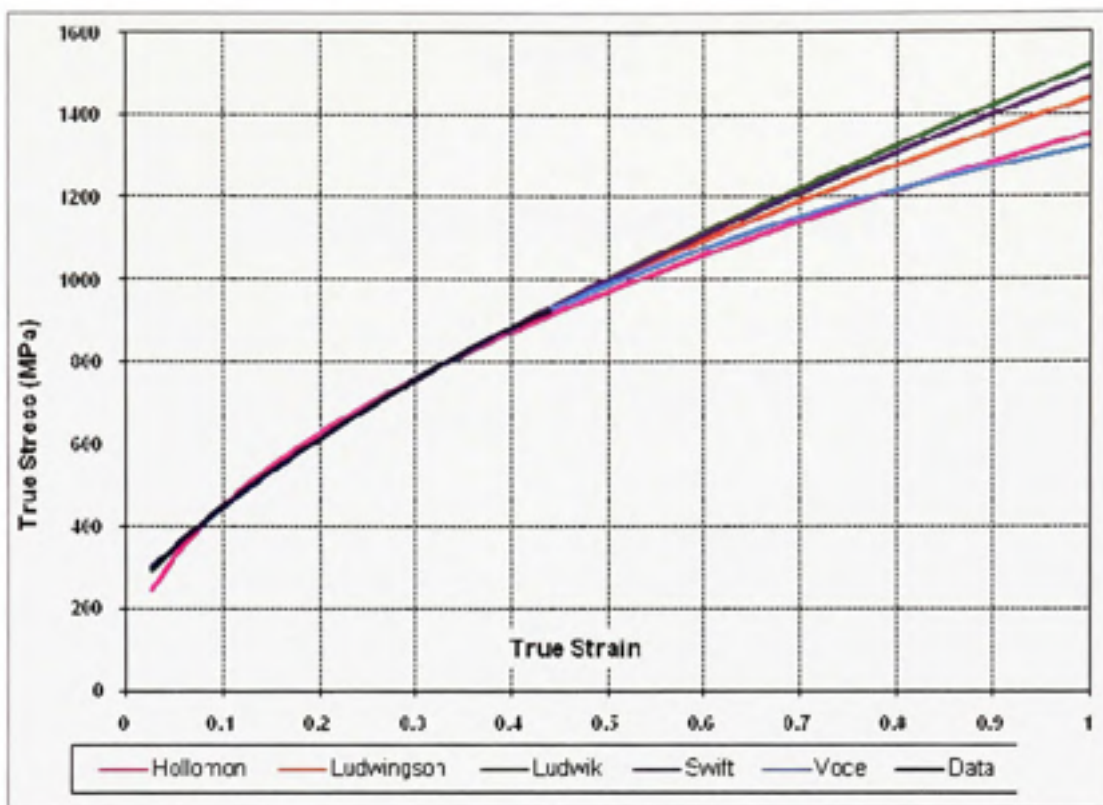


Figure-A-IV.3 Stress-strain curves of SS 321 curved specimens
1.2 mm thickness fitted by calculated hardening equations extended up to 100%.

ANNEX V

1.2 mm THICKNESS TUBE SPECIMENS DATA



Figure-A-V.1 Engineering stress-strain curves of SS 321 tube samples cut all over the tube – 1.2 mm thick.

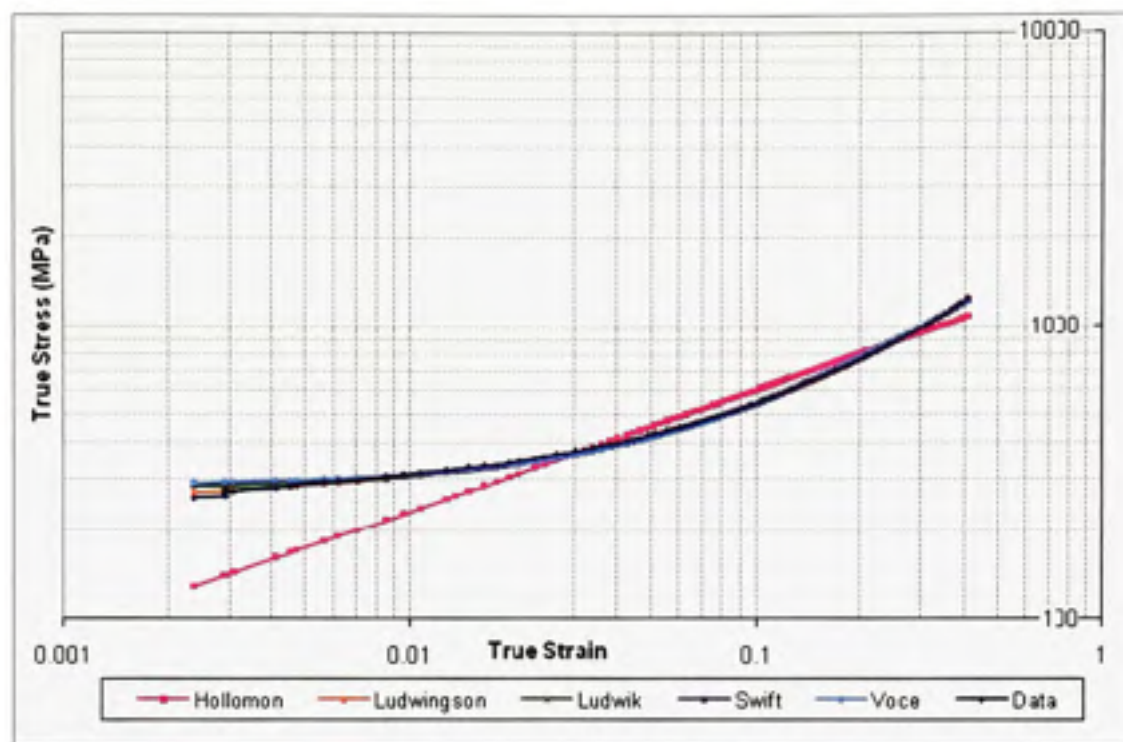


Figure-A-V.2 Stress-strain curve of SS 321 tube specimen 1.2 mm thick fitted by calculated hardening equations in the logarithmic scale.

Table-A-V.1 Best fit coefficients of the tested hardening equations – SS321 curved specimens – 1.2 mm thick

| 1.2 tube | Hollomon $\sigma = K \varepsilon_P^n$ | Ludwigson $\sigma = K \varepsilon_P^n + \exp(K_1 + n_1 \varepsilon_P)$ | Ludwik $\sigma = \sigma_0 + K \varepsilon_P^n$ | Swift $\sigma = K (\varepsilon_0 + \varepsilon)^n$ | Voce $\sigma = \sigma_v - K_v \exp(n_v \varepsilon_P)$ |
|-------------|--|---|---|---|---|
| K | 1562.9 | 2375.9 | 2099.1 | 2179.6 | $K_v = 3732.4$ |
| n | 0.4128 | 0.7462 | 0.8894 | 0.8124 | $n_v = -0.7031$ |
| | | $K_1 = 5.5282$ $n_1 = -7.4394$ | $\sigma_0 = 275.11$ | $\varepsilon_0 = 0.0812$ | $\sigma_v = 4020.5$ |
| S-R | 449247 | 1396 | 5684 | 8533 | 11096 |

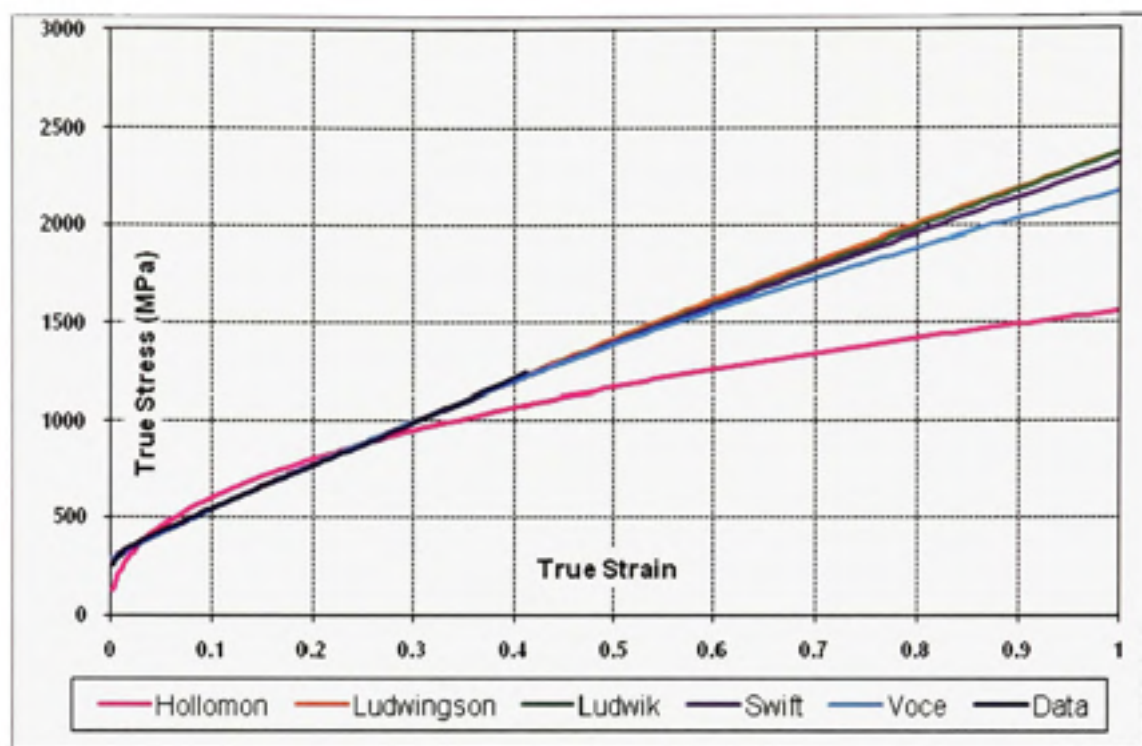


Figure-A-V.3 Stress-strain curves of SS 321 tube specimens 1.2 mm thickness fitted by calculated hardening equations extended up to 100%.

BIBLIOGRAPHY

- Ahmetoglu, M., and T. Altan. 2000. « Tube hydroforming: state-of-the-art and future trends ». *Journal of Materials Processing Technology*, vol. 98, n° 1, p. 25-33.
- Allen, Dell K. 1969. *Metallurgy theory and practice*. Chicago: American Technical Society, 663 p.
- American Society for Testing and Materials. 2000. *Standard Test Method for Tensile Strain-Hardening Exponents (n-values) of Metallic Sheet Materials*. ASTM E646-00. West Conshohocken (PA): ASTM International, 7 p.
- Askeland, Donald R., and Pradeep Prabhakar Phulé. 2003. *The science and engineering of materials*, 4th. Pacific Grove, Calif.: Thomson Brooks/Cole, xxviii, 1003 p.
- ASM International. 2001. *Alloy Digest data on worldwide materials and alloys : 1952-2000*, Version PC and MAC. Materials Park, Ohio: ASM International, 1 cédérom p.
- ASM International. 2002. *ASM alloy center online*. Coll. « ASM materials information », Materials Park, OH: ASM International.
- Bortot, P., et al. 2008. « The determination of flow stress of tubular material for hydroforming applications ». *Journal of Materials Processing Technology*, vol. 203, n° 1-3, p. 381-388.
- Bowman, Keith J. 2004. *Mechanical behavior of materials*. Hoboken, NJ: John Wiley, xi, 334 p. <<http://www.loc.gov/catdir/toc/wiley041/2004299135.html>>.
- Boyer, Howard E. 1990. *Atlas of stress-strain curves*. Metals Park, Ohio: ASM International, xx, 630 p. <<http://products.asminternational.org/datasheets/index.jsp>>. Consulté le November 14th 2008.
- Chandler, Harry E. 1996. *Heat treater's guide : practices and procedures for nonferrous alloys*. Materials Park, Ohio: ASM International, viii, 669 p.
- Chen, K. K., et al. 2004. *Free expansion bulge testing of tubes for automotive hydroform applications*. SAE technical paper No. 2004-01-0832. Warrendale, Pennsylvania.
- Datsko, Joseph. 1966. *Material properties and manufacturing processes*. New York: Wiley, 543 p.
- Dieter, George Ellwood. 1986. *Mechanical metallurgy*, 3rd ed. Coll. « McGraw-Hill series in materials science and engineering ». New York: McGraw-Hill, xxiii, 751 p. <<http://www.loc.gov/catdir/toc/mh023/85018229.html>>.

- Douthett, Joseph. 2006. *Metalworking : Sheet forming, Forming of stainless steel*. En ligne. ASM International.
- Dowling, Norman E. 2007. *Mechanical behavior of materials : engineering methods for deformation, fracture, and fatigue*, 3rd. Upper Saddle River, N.J.: Pearson/Prentice Hall, xvii, 912 p. <<http://www.loc.gov/catdir/toc/fy0705/2006281523.html>>.
- Falco, Simone. 2008. « Behaviour of hydroformed tubes: Numerical models vs. Experimental results ». Napoli, Università degli studi di Napoli "Federico II", 81 p.
- Gholipour, Javad, et al. 2004. *Application of damage models in bending and hydroforming of aluminum alloy tube*. SAE technical paper No. 2004-01-835. Warrendale, Pennsylvania.
- Hwang, Yeong-Maw, and Yi-Kai Lin. 2002. « Analysis and finite element simulation of the tube bulge hydroforming process ». *Journal of Materials Processing Technology*, vol. 125-126, p. 821-825.
- Hwang, Yeong-Maw, et al. 2007. « Evaluation of tubular materials by a hydraulic bulge test ». *International Journal of Machine Tools and Manufacture*, vol. 47, n° 2, p. 343-351.
- Hwang, Yeong-Maw, et al. 2004. « Study on forming limit of tubular materials ». *Key Engineering Materials*, vol. 274-276, n° 1, p. 391-396.
- Kleemola, H. J., and M. A. Nieminen. 1974. « On the Strain-Hardening Parameters of Metals ». *Metallurgical transactions. A*. Vol. 5, n° 8, p. 1863-1866.
- Koç, Muammer. 2008. *Hydroforming for advanced manufacturing*. Coll. « Woodhead publishing in materials ». Cambridge Boca Raton: Woodhead publishing ; CRC Press, 396 p.
- Koç, Muammer, et al. 2001. « On the characteristics of tubular materials for hydroforming - experimentation and analysis ». *International Journal of Machine Tools and Manufacture*, vol. 41, n° 5, p. 761-772.
- Kuwabara, T., et al. 2003. « Yield locus and work hardening behavior of a thin-walled steel tube subjected to combined tension-internal pressure ». *J. Phys. IV France*, vol. 105, p. 347-354.
- Levy, B. S., et al. 2004. « Characterizing steel tube for hydroforming applications ». *Journal of Materials Processing Technology*, vol. 150, n° 3, p. 280-289.

- Lianfa, Yang, and Guo Cheng. 2008. « Determination of stress-strain relationship of tubular material with hydraulic bulge test ». *Thin-Walled Structures*, vol. 46, n° 2, p. 147-154.
- Miles, M. 2006. « Formability testing of Sheet metals ». In *Metalworking : Sheet forming*, 9th. Online. Vol. 14B, p. 673-696. Coll. « ASM handbook ». Material Park, Ohio: ASM International ; <<http://products.asminternational.org/hbk/index.jsp>>. Consulted on April 3rd 2008.
- Mokrzycki, Marcin, and Jean Savoie. 2006. *Reproducibility of sheet metal properties for aerospace applications*. Coll. « Pratt & Whitney Canada technical reports ». Longueuil (QC): Pratt & Whitney Canada, 62 p.
- Montheillet, Frank. 2008. « Métallurgie de mise en forme à froid ». In *Mise en forme*. Online. Techniques de l'ingénieur. Consulted on November, 10th.
- Moosbrugger, Charles. 2002. « Representation of Stress-Strain Behavior ». In *Atlas of stress-strain curves*, 2nd. p. iv, 816. Materials Park, Ohio: ASM International. <<http://www.loc.gov/catdir/toc/fy035/2002027674.html>>.
- Peckner, Donald, and I. M. Bernstein. 1977. *Handbook of stainless steels*. New York, N.Y.: McGraw-Hill, 1 v. 1107 p.
- Russel, K. C., and L. M. Brown. 1972. « A dispersion strengthening model based on differing elastic module applied to the copper-iron system ». *Acta metallurgica*, vol. 20, p. 969-974.
- Sanchez, F., and Javad Gholipour. 2008. *Simulation study of hydroforming of sharp angles*. Coll. « National Research Council Canada reports ». Montréal (QC): NRC-IAR-AMTC, 22 p.
- Slama, C., and G. Cizeron. 1997. « Structural behaviour of INC 718 Etude du comportement structural de l'alliage NC 19 Fe Nb (Inconel 718) ». *Journal de physique. III*, vol. 7, n° 3, p. 665-688.
- Sokolowski, T., et al. 2000. « Evaluation of tube formability and material characteristics: Hydraulic bulge testing of tubes ». *Journal of Materials Processing Technology*, vol. 98, n° 1, p. 34-40.
- Song, Jung Han, and Hoon Huh. 2007. « The effect of strain rate on the material characteristics of nickel-based superalloy inconel 718 ». *Key Engineering Materials*, vol. 340-341 1, p. 283-288.
- Special Metals Corporation. 2007. *Inconel alloy 718*. Online. <<http://www.specialmetals.com/documents>>. Consulté le April 3rd 2008.

- Vollertsen, F. 2001. « State of the art and perspectives of hydroforming of hydroforming of tubes and sheets ». *Journal of Materials Science and Technology*, vol. 17, n° 3, p. 321-324.
- Wu, Jui-Hung. 2003. « High temperature mechanical properties, fatigue and fracture behavior of 17-4 PH stainless steel ». Thesis dissertation, Taiwan, National central university, 134 p.
- Youle, A., and B. Ralph. 1972. « A study of the precipitation of Copper from α -iron in the pre-peak to peak hardness range of aging ». *Metal science journal*, vol. 6, p. 149-152.